University of Warsaw

Doctoral Thesis

Nonlinear coupled systems: effects of gain, loss and nonlocality

Author:
Aleksandr Ramaniuk

Supervisor:
Prof. dr hab. Marek Trippenbach

A thesis submitted in fulfillment of the requirements for the degree of Doctor of Philosophy

in the

Institute of Theoretical Physics
Faculty of Physics

UNIVERSITY
OF WARSAW

October 4, 2021

Declaration of Authorship

I, Aleksandr Ramaniuk, declare that this thesis titled, "Nonlinear coupled systems: effects of gain, loss and nonlocality" and the work presented in it are my own. I confirm that:

- This work was done wholly or mainly while in candidature for a research degree at this University.
- Where any part of this thesis has previously been submitted for a degree or any other qualification at this University or any other institution, this has been clearly stated.
- Where I have consulted the published work of others, this is always clearly attributed.
- Where I have quoted from the work of others, the source is always given. With the exception of such quotations, this thesis is entirely my own work.
- I have acknowledged all main sources of help.

Signed:

Date:

UNIVERSITY OF WARSAW

Abstract

Institute of Theoretical Physics, Faculty of Physics

Doctor of Philosophy

Nonlinear coupled systems:
effects of gain, loss and nonlocality

by Aleksandr Ramaniuk

Nonlinear phenomena exist in almost every type of physical system. Arguably, the most prevalent type of interaction is third-order nonlinearity, which is usually described by Gross-Pitaevskii Equations or Nonlinear Schrodinger Equations (NLSE). In certain cases, a nonlinear medium allows for the coexistence of multiple components interacting with each other. In this case, Coupled Nonlinear Schrodinger Equations are used to describe the complete physical system. Coupled NLSE is used in multiple fields of study, including optical waveguides, liquid crystals, cold atoms, and polariton condensates. The main goal of this thesis is to explore the influence of nonlocality, saturable gain, and other effects on coupled nonlinear systems. The additional goal is to present different analytical and numerical methods for the exploration of nonlinear effects in a concise manner.

The research presented in my thesis is divided into two parts. In the first part, we focus on two linearly coupled rings with saturable gain. This system is based on rings traps for polariton condensates. We discovered a rich family of solutions, exhibiting several interesting phenomena, including modulational instability, inhomogeneous stable states, chaotic behavior, and spontaneous symmetry breaking. We also observed spontaneous vortex generation in the system with localized coupling between rings. These processes are explained by observing current flow both inside and between rings.

In the second part, we explore beam propagation in a system with nonlocal nonlinear coupling. This system models two-color vector solitons in nematic liquid crystals. We focused our research on supermodes - multi-peak fundamental solitons, emerging due to counteraction of focusing and defocusing nonlinearity. We observed spontaneous trajectory bending due to the breaking of action-reaction symmetry. We've shown that the dynamics of trajectory bending can be predicted by looking at the relative shift between two components of vector soliton.

Acknowledgements

Firstly, I would like to thank my supervisor, prof. Marek Trippenbach, for patient guidance and many insights during my PhD studies and preparation of this work.

I want to thank dr. Pawel Jung for his insights into the nuances of numerical work and help during final steps of thesis preparation.

I'm grateful to all my fellow colleagues from Faculty of Physics – Jakub Kierdaszuk, Adam Gasiorowski, Krzysztof Czajkowski, Tomasz Stefaniuk, Dominika Switlik, Arkadiusz Ciesielski and many others – for sustaining atmosphere of support and creativity.

I am thankful to many senior scientist all around the globe – prof. Boris Malomed (Israel), prof. Vladimir Konotop (Portugal), prof. Michael Giersig (Germany/China), prof. Jacek Siedlecki (Denmark), prof. Gaetano Assanto (Italy) – and their research groups for greatly expanding my worldview, both in science and beyond. I want to thank University's Integrated Development Programme ZIP and its "Mobility for PhD Students" programme for making many of these collaborations possible.

I'm grateful to my parents – Anna and Sergiusz – for unending support of my curiosity from the earliest age.

Last, I want to thank University Center of Psychological Support, Mental Health Clinic "Centrum", Mental Health Clinic "Educatio" and their staff – in particular Joanna Stryjczyk, Tamara Wozniak, Agata Swoboda, Renata Skladanek and Anna Mach. Fellow scientists helped me start my journey as a PhD student – and you helped me finish it.

I want to dedicate my work to every PhD student struggling with physical and mental pressure of the scientist life. You are not alone. Our problems and worries break us, but we can rebuild each other stronger than ever. Remember – your darkest hour comes right before the sunset.

Contents

Declaration of Authorship iii

Abstract v

Acknowledgements vii

List of Figures xi

List of Publications xvii

List of Abbreviations xix

1 Introduction 1
- 1.1 Brief history of nonlinear optics . . . 1
- 1.2 Nonlinear optical processes . . . 3
- 1.3 Nonlinear Schrödinger Equation . . . 4
- 1.4 Solitons and nonlinear dynamics . . . 7
- 1.5 Thesis outline . . . 9

2 Theory of solitons in coupled nonlinear systems 11
- 2.1 Integrals of motion - scalar case . . . 12
- 2.2 Scalar solitons . . . 13
- 2.3 Linear stability analysis . . . 14
- 2.4 Vector solitons . . . 15
  - 2.4.1 Constants of motion in coupled NLSE . . . 16

3 Numerical methods for coupled nonlinear systems simulation 19
- 3.1 Propagation methods . . . 19
  - 3.1.1 Finite difference methods . . . 20
  - 3.1.2 Spectral methods . . . 21
  - 3.1.3 Split-step methods . . . 22
- 3.2 Soliton relaxation methods . . . 23
  - 3.2.1 Imaginary time method . . . 23
  - 3.2.2 Newton Conjugate Method . . . 24

4 Vector solitons in planar waveguides with nonlinear inclusions 27
- 4.1 Planar waveguides . . . 27

4.2 Single-delta waveguides . . . 29
4.3 Double-delta waveguides . . . 32
4.4 Two-dimensional waveguide model . . . 36

5 Gain and loss in coupled nonlinear systems **39**
5.1 Exciton polariton condensates . . . 39
5.2 Homogeneous coupling . . . 42
5.2.1 Stability analysis . . . 45
5.2.2 Inhomogeneous states . . . 47
5.2.3 Dynamic states . . . 49
5.3 Inhomogeneous coupling . . . 50
5.3.1 Narrow coupling . . . 51
5.3.2 Broad coupling . . . 51

6 Nonlocal nonlinearity in coupled systems **57**
6.1 Nematic liquid crystals and nematicons . . . 57
6.2 Nonlocal model of liquid crystal medium . . . 61
6.3 Supermode spatial solitons in nonlocal media . . . 64
6.3.1 Rescaled coupled model . . . 65
6.3.2 Family of supermode states . . . 66
Pseudo-scalar soliton case . . . 66
Vector soliton case . . . 69
6.3.3 Dynamics of nonlocally coupled solitons . . . 71
6.3.4 Trajectory bending in vector supermode solitons . . . 72
Analytical considerations . . . 73
Numerical investigation . . . 76

7 Conclusions **83**

A Derivation of conservation laws in coupled NLSE **85**

B Newton Conjugate Gradient method in coupled NLSE **89**

Bibliography **93**

List of Figures

1.1 Photographies of water soliton waves at Nuevo Vallarta, Mexico. Photographs made by M.J. Ablowitz. After Ref. [11]. 2
1.2 First experimental observation of the nonlinear optical effect – second harmonic generation. Actual nonlinear signal was infamously mistaken for noise by the publisher and removed. After Ref. [18]. 3
1.3 Formation of optical soliton beam (top) in the photorefractive medium. After Ref. [55]. 6
1.4 Simulation of bright soliton collision for in-phase solitons (left) and out-of-phase solitons (right). After Ref. [82]. 7

2.1 Schematic representation of diffraction term (red) and nonlinear term (blue) influence on the formation of bright (left) and dark (right) solitons. 12

4.1 Schematic representation of the planar waveguides (top) and photos of silicon-based waveguides (bottom). Image from NTT-AT archives www.keytech.ntt-at.co.jp/optic2/prd_e0015.html. 28
4.2 Norm (left), energy (center) and asymmetry coefficients (right) for the stationary states in one-delta system for $\kappa = 1$. Dashed lines represent unstable states. After Ref. [165]. 32
4.3 Examples of states with different symmetry properties. (a) – fully symmetric state; (b) – "inter-symmetric" state; (c) – "intra-symmetric" state; (d) – fully asymmetric state. After Ref. [165]. 33
4.4 Map of solution types for different values of κ and μ_+. Fully asymmetric states are found numerically in the red region, while fully symmetric states exist in both red and peach areas. Additional color filters represent areas with present intra-symmetric states (blue region defined by the equation 4.31) and inter-symmetric states (green region defined by the equation 4.33). After Ref. [165]. 34
4.5 Norm (left), energy (center) and asymmetry coefficients (right) for the stationary states in two-delta system for $\kappa = 0.05$. Black curves represent fully symmetric states, orange curves – "inter-symmetric" states, cyan curves – "intra-symmetric" states. Inset in subfigure (a) zooms on bifurcation points for both asymmetry states. Orange and cyan curve in subfigure (c) represent Θ_c and Θ_s respectively. After Ref. [165]. . . 35

4.6 Norm (left), energy (center) and asymmetry coefficients (right) for the stationary states in two-delta system for $\kappa = 0.2$. Black curves represent fully symmetric states, orange curves – "inter-symmetric" states, cyan curves – "intra-symmetric" states. Inset in subfigure (a) zooms on bifurcation points for both asymmetry states. Orange and cyan curve in subfigure (c) represent Θ_c and Θ_s respectively. After Ref. [165]. . . 36
4.7 Schematic representation of two potential wells with double nonlinear inclusions. After Ref. [165]. 37
4.8 Contour plots of wavefunction distribution of the stable two-dimensional solitons. Panels present fully symmetric states (a-b), states with single symmetry breaking (c-d) and states with double symmetry breaking (e-f). Parameters for the (a,c,e) simulations – $L = 11, D = 1, W = 4, V = 2$ and $N = 0.6(a), N = 1.5(c), N = 2.5(e)$. Parameters for the (b,d,f) simulations – $L = 1, D = 1, W = 3, V = 52$ and $N = 1(b), N = 4(d), N = 5.1(f)$. After Ref. [165]. 38

5.1 Fundamentals of exciton-polariton condensation. (a) – structure of quantum well used for polariton excitation. (b) – scheme of exciton-polariton pumping and condensation. After Ref. [52]. 40
5.2 Experimental observation of exciton-polariton ring condensates. (a-d) – single-ring condensate. (e) – double-ring condensate. (f) – schematic of ring condensate observation device. (g) – phase portrait of the condensate in example (b). After Ref. [188]. 41
5.3 (a-b) – examples of fabricated microresonator array. (c) – possible configurations of microresonators with inhomogeneous coupling. After Ref. [195]. 41
5.4 Schematic of double-ring structure described by Equations 5.3. After Ref. [196]. 42
5.5 Asymmetric branches domains. (a-b) – Branches of stationary solutions for $\tilde{c} = 0.38 < \tilde{c}_2$ (a) and $\tilde{c} = 0.8 > \tilde{c}_2$ (b). Red and blue curves represent symmetric and antisymmetric solutions, green and black curves represent asymmetric solutions μ_+ and μ_-. (c) – domains of existence for asymmetric states. Both asymmetric states exist inside green area, but only $\tilde{\mu}_-$ solutions exist in gray area. Upper border of both areas is defined by Γ_{crit}, lower bound of green area is described by Γ_{bif}. After Ref. [196]. 44
5.6 Transverse currents in asymmetric states for $\tilde{c} = 0.38 < \tilde{c}_2$ (a) and $\tilde{c} = 0.8 > \tilde{c}_2$ (b). After Ref. [196]. 45

5.7 Stability analysis of symmetric states. (a) – instability domains. Wavenumbers of unstable modes are noted in each domain. Colours signify different amount of unstable modes, gray color denotes stable domains. Red square outlines parametric area explored numerically. (b) – states reached through propagation of perturbed symmetrical state. Gray areas correspond to stable domains. Blue dots show symmetric states evolving into antisymmetric states; red triangles – into out-of-phase vortices with $\kappa = 1$; red stars show limit cycle oscillations with homogeneous density; red squares lead to stationary inhomogeneous states; red circle at $\gamma = c = 2$ represents chaotic motion; black stripe in lower left corner shows evolution into asymmetric state. Points on left axis correspond to $c = 0.01$. All calculations were made for $\Gamma = 1$. After Ref. [196]. 46

5.8 Inhomogeneous state, obtained for $\gamma = 1.5, \Gamma = 1, c = 1.75$. (a) – wavefunctions amplitudes. (b) – time evolution of central Fourier components. Inset present final Fourier spectrum of inhomogeneous state. (c) – relative phase θ. Figures (a-c) present full numerical simulation (solid line) and Galerkin approximation with $k = \{-1, 0, 1\}$ modes (dashed line). (d) – Intra-ring current $j_\perp$ (solid line) and inner ring currents j_m (dashed and dotted curves). After Ref. [196]. 48

5.9 Phase portraits of norm oscillations. (a) – limit cycle oscillations, observed at $\Gamma = 1, \gamma = 1, c = 1.25$. (b) – chaotic oscillations at $\Gamma = 1, \gamma = 2, c = 2$. Small frames show corresponding time evolution of total norm. After Ref. [196]. 49

5.10 Comparison of norm dynamics Fourier spectra for numerical simulations (black) and Galerkin approximation using 11 modes (color). Two frames correspond to different initial perturbations. Initial parameters $\Gamma = 1, \gamma = 1.75, c = 1.81$. After Ref. [197]. 49

5.11 Antisymmetric stationary states in inhomogeneously coupled system. Left – amplitudes (absolute values) of wavefunction ψ_1 for various coupling strengths and fixed coupling width $w = 1$. Black curve represents homogeneous state of the decoupled system. Right – amplitudes of ψ_1 for fixed coupling strength $c_0 = 1$ and varying widths. After Ref. [195]. 51

5.12 Absolute value $|\psi_1|$ (left) and relative phase (right) of the asymmetric (blue and red) and antisymmetric (black) states in case of narrow coupling $w = 0.01$. Antisymmetric and asymmetric state are calculated for $c_0 = 1$ and $c_0 = 1.5$ respectively. Phase oscillation term is calibrated so that $\phi_1(x = \pm\pi) = 0$. After Ref. [195]. 52

5.13 Top: pseudocolor plots of absolute values and relative phases of ψ_1 wavefunction component during limit cycle oscillations for $c_0 = 4$ (left) and $c_0 = 5$ (right). Oscillations of the second channel are shifted by half-period and reflected around $x = 0$ axis in case of asymmetric oscillations. Phase oscillation term is calibrated so that $\phi_1(x = \pm\pi) = 0$. Bottom: total norms in both channels and norm average during one oscillation period for $c_0 = 4$ (left) and $c_0 = 5$ (right). Coupling width is equal to $w = 1$ in both cases. After Ref. [195]. 52

5.14 Snapshots of symmetric limit cycle oscillations, representing half-period of oscillation for $c_0 = 4, w = 1$. Frames are presented in pairs – top frames (a1-h1) show absolute values of wavefunctions ψ_1 and ψ_2 (blue and red curve respectively) and rescaled coupling distribution (green curve); bottom frames (a2-h2) show relative phases in both channels. Phase oscillation term is calibrated so that $\phi_1(x = \pm\pi) = 0$ (blue curve). After Ref. [195]. 53

5.15 Snapshots of asymmetric limit cycle oscillations, representing full period of oscillation for $c_0 = 5, w = 1$. Frames are presented in pairs – top frames (a1-h1) show absolute values of wavefunctions ψ_1 and ψ_2 (blue and red curve respectively) and rescaled coupling distribution (green curve); bottom frames (a2-h2) show relative phases in both channels. Phase oscillation term is calibrated so that $\phi_1(x = \pm\pi) = 0$ (blue curve). After Ref. [195]. 54

5.16 Left – frequency of the symmetric (solid lines) and asymmetric (dashed lines) limit cycle oscillations for three different values of γ. All calculations performed for $w = 1, \Gamma = 1$. Right – norm in both channels during oscillations transition for $c_0 = 4.5$ (point of blue line discontinuity on the left panel). After initial propagation (not shown) systems temporarily develops symmetric oscillations, which morph into asymmetric oscillations after several periods of oscillation. After Ref. [195]. 55

5.17 Snapshots of transition from symmetric to asymmetric oscillations for $c_0 = 4.5, w = 1$. Frames are presented in pairs – top frames show absolute values of wavefunctions ψ_1 and ψ_2 (blue and red curve respectively) and rescaled coupling distribution (green curve); bottom frames show relative phases in both channels. Phase oscillation term is calibrated so that $\phi_1(x = \pm\pi) = 0$ (blue curve). After Ref. [195]. . 56

6.1 Schematic representation of molecules positioning in different LC phases. (a) – Nematic, (b) – Smectic A, (c) – Smectic C, (d) – Cholesteric (chiral nematic). After Ref. [208]. 58

6.2 Example of experimental setup for exploration of soliton propagation in nematic LC cell. Initial beam propagates in linear regime or forms a soliton depending on the polarization in respect to the LC molecules. After Ref. [213]. 59
6.3 Experimental observation of three-colour vector nematicon. Each of the three components diffracts during separate propagation (a-c), but they form soliton once launched together (d). After Ref. [221]. 60
6.4 Schematic representation of optical beam (red) propagation in LC cell with planar orientation of molecules (blue). E_y is the electric field polarization vector and n is the molecule orientation vector. 62
6.5 Formation of scalar supermode solitons for $N = K = 1, A = 1, B = 0.5$. (a) – wavefunction profile for nonlocality ratio $\sigma = 0.7$ and different values of power P. (b) – wavefunction profile for different values of nonlocality ratio σ and power $P = 2500$. (c-e) – Normalized intensity (blue) and nonlinear potential (magenta) distributions for one-peak (c), two-peak (d) and smoothed peak (e) states. Distributions are normalized so that $\psi_{max} = 1$ and $F_{max} = 1$. Dashed boxes are zooms of nonlinear potential shapes near beam center. After Ref. [205]. . . . 67
6.6 Scalar supermode states map for $N = K = 1, P = 2500$. Top graphs show intensity profiles calculated at $B = 0.7$ points marked by red circles on the bottom map. Profile colors correspond to map regions colors. Dashed line represents $\sigma = \sqrt[3]{B}$ curve. After Ref. [205]. 68
6.7 (a) – Two-hump soliton profiles for different values of wavelength ratio K and $B = 0.5, \sigma = 0.7, P = 2500$. (b) – Three-hump soliton profiles for $A = 0$ and $A = 1$, with the remaining parameters $K = 0.6, B = 0.6, \sigma = 0.6, P = 2500$. After Ref. [205]. 70
6.8 Vector supermode states map for $K = 0.6, P = 2500$. Top graphs show intensity profiles calculated at $B = 0.5$ points marked by red circles on the bottom map. Profile colors correspond to map regions colors. Dashed line represents $\sigma = \sqrt[3]{B}$ curve. After Ref. [205]. 70
6.9 Examples of two-hump vector soliton propagation for $B = 0.5, \sigma = 0.65, P = 2500$. (a) – Meta-stable propagation for $K = 1.2$. (b) – Soliton collapse for $K = 0.9$. (c) – Soliton evolution for $K = 0.9$ with absorption coefficient $\alpha_0 = 0.25$. After Ref. [205]. 72
6.10 Trajectory bending with controlled perturbation for $K = 1$ (left) and $K = 0.9$ (right). Top row – propagation with shift perturbation $\delta_{2s} = 0.003$. Middle row – propagation with asymmetry perturbation $\delta_{1a} = 0.1$. Bottom row – propagation with phase perturbation $\delta_{1p} = 0.1$. All simulations performed with initial parameters $B = 0.5, \sigma = 0.75$. . . . 78

6.11 Top – soliton center position and acceleration (yellow) for focusing (solid) and defocusing (dashed) component. Bottom – soliton acceleration and beam center misalignment $\langle X\rangle_1 - \langle X\rangle_2$ (black dotted curve). Initial parameters: $K = 0.9, B = 0.5, \sigma = 0.75, \delta_{1a} = 0.2$. 79

6.12 Trajectory bending of different initial supermode states for $K = 1$ (left column) and $K = 0.9$ (middle column). Right column presents initial state distribution for $K = 0.9$. All calculations were performed for $B = 0.5$ using shift perturbation $\Delta_{2,shift} = 0.003$. Each row corresponds to different value of nonlocality ratio. Top to bottom – $\sigma = 0.85; \sigma = 0.75; \sigma = 0.65; \sigma = 0.55$. 80

6.13 Perturbed soliton propagation for $B = 0.5, \sigma = 0.75, \Delta_{2,shift} = 0.003$ including different terms of coupled structure influence. Top left – pseudo-scalar case ($N = 1, K = 1$). Top right – two components with different diffractive terms and equal nonlinear terms ($N = 0.9, K = 1$). Bottom left – two components with equal diffractive terms and different nonlinear terms ($N = 1.11, K = 0.9$). Bottom right – two components with different diffractive and nonlinear terms ($N = 1, K = 0.9$). 81

List of Publications

The following publications form the basis of this thesis:

1. Zegadlo, K. B. and Hung, N. V. and Ramaniuk, A. and Trippenbach, M. and Malomed, B. A. (2018). "Symmetry Breakings in Dual-Core Systems with Double-Spot Localization of Nonlinearity." Symmetry-Basel 10(5).

2. Hung, N. V. and Zegadlo, K. and Ramaniuk, A. and Konotop, V. V. and Trippenbach, M. (2017). "Modulational instability of coupled ring waveguides with linear gain and nonlinear loss." Scientific Reports 7.

3. Ramaniuk, A. and Hung, N. V. and Giersig, M. and Kempa, K. and Konotop, V. V. and Trippenbach, M. (2018). "Vortex Creation without Stirring in Coupled Ring Resonators with Gain and Loss." Symmetry-Basel 10(6).

4. Ramaniuk, A. and Trippenbach, M. and Jung, P. S. and Christodoulides, D. N. and Krolikowski, W. and Assanto, G. (2021). "Scalar and vector supermode solitons owing to competing nonlocal nonlinearities." Optics Express 29(6): 8015-8023.

5. Ramaniuk, A. and Jung, P. S. and Christodoulides, D. N. and Krolikowski, W. and Trippenbach, M. (2021). "Transverse velocity instability and trajectory bending in two-beam supermode solitons." *In preparation.*

The following articles have been published during my Ph.D. studies outside the scope of this thesis.

1. Ramaniuk, A. and Jung, P. S. and Christodoulides, D. N. and Krolikowski, W. and Trippenbach, M. (2019). "Absorption-mediated stabilization of nonlinear propagation of vortex beams in nematic liquid crystals." Optics Communications 451: 338-344.

2. Dinh, Q. H. and Pniewski, J. and Le Van, H. and Ramaniuk, A. and Long, V. C. and Borzycki, K. and Xuan, K. D. and Klimczak, M. and Buczynski, R. (2018). "Optimization of optical properties of photonic crystal fibers infiltrated with carbon tetrachloride for supercontinuum generation with subnanojoule femtosecond pulses." Applied Optics 57(14): 3738-3746.

3. Van, L. C. and Anuszkiewicz, A. and Ramaniuk, A. and Kasztelanic, R. and Xuan, K. D. and Long, V. C. and Trippenbach, M. and Buczynski, R. (2017). "Supercontinuum generation in photonic crystal fibres with core filled with toluene." Journal of Optics 19(12).

4. Pniewski, J. and Ramaniuk, A. and Kasztelanic, R. and Smietana, M. and Trippenbach, M. and Buczynski, R. (2017). "Applicability of suspended-core fibres for attenuation-based label-free biosensing." Optics Communications 402: 290-295.

5. Pniewski, J. and Stefaniuk, T. and Le Van, H. and Long, V. C. and Van, L. C. and Kasztelanic, R. and Stepniewski, G. and Ramaniuk, A. and Trippenbach, M. and Buczynski, R. (2016). "Dispersion engineering in nonlinear soft glass photonic crystal fibers infiltrated with liquids." Applied Optics 55(19): 5033-5040.

6. Stefaniuk, T. and Le Van, H. and Pniewski, J. and Long, V. C. and Ramaniuk, A. and Grajewski, K. and Van, L. C. and Karpierz, M. and Trippenbach, M. and Buczynski, R. (2015). "Dispersion engineering in soft glass photonic crystal fibers infiltrated with liquids." Optical Fibers and Their Applications 2015 9816.

List of Abbreviations

KdV	**K**orteveg-**d**e **V**ries (Equation)
NLSE	**N**on**L**inear **S**chrödinger **E**quation
BEC	**B**ose-**E**instein **C**ondensate
SSB	**S**pontaneous **S**ymmetry **B**reaking
FD	**F**inite **D**ifference
SSFM	**S**plit-**S**tep **F**ourier **M**ethod
ITEM	**I**maginary **T**ime **E**volution **M**ethod
AITEM	**A**ccelerated **I**maginary **T**ime **E**volution **M**ethod
NCG	**N**ewton **C**onjugate **G**radient
CMT	**C**oupled **M**ode **T**heory
EPC	**E**xciton **P**olariton **C**ondensate
LC	**L**iquid **C**rystal

Chapter 1

Introduction

Our world is nonlinear. Every time we look at clay, hear thunderstorms or feel air drag during a car ride, we observe something more than the simple sum of its parts. Every time we explore anything deep enough, we find borders of our linear intuition. Classical mechanics is a special case of deeply nonlinear relativity theory. The linearity of Maxwell equations holds its ground until we switch from abstract charges and currents to atoms and molecules. Even fundamentally linear quantum mechanics is filled with nonlinear interactions. A simple, linear view of the universe is nothing more than an approximation of the reality [1].

The difference between linear and nonlinear worlds is defined by the superposition principle. The superposition principle states that the response of the complex input can be represented as a sum of the simpler inputs.

$$F(\sum_m a_m X_m) = \sum_m a_m F(X_m) \tag{1.1}$$

All linear systems follow the superposition principle. Every state of linear systems can be represented as a sum of basic solutions – modes. However, nonlinear states can't be exactly represented through the superposition of modes.

1.1 Brief history of nonlinear optics

Scientists have tried to describe the physical world in a purely linear manner since the very beginning of classical mechanics. Simple nonlinear systems, such as oscillating gravity pendulum or spring at the deformation limit, were known to the physicists, but they were approximated by the appropriately linear models. Development of the nonlinear physics started only in the 19th century. In 1834, John Scott Russell discovered "waves of translation" – the first experimentally observed example of the soliton [2]. Research of the liquid and gas thermodynamics led to the development of the kinetic theory of gases and the creation of the Boltzmann equation for molecular dynamics [3]. Works of Poincare on the three-body problem of celestial mechanics became foundational to the dynamical systems theory [4]. In 1895,

FIGURE 1.1: Photographies of water soliton waves at Nuevo Vallarta, Mexico. Photographs made by M.J. Ablowitz. After Ref. [11].

Diederik Korteweg and Gustav de Vries created the first explicitly nonlinear model that could explain solitary water waves – this model is known as KdV equation [5]. Nonlinear effects in electrodynamics were explored both in the fundamental theory of electron interactions, leading to the creation of the Born-Infeld model [6], and in the experimental research on the electrical circuits [7]. Even the classical mechanics itself was expanded to the nonlinear model of general relativity [8]. Nowadays, nonlinear processes are explored in every field of modern physics [9, 10].

This thesis focuses on the particular field of nonlinear sciences – nonlinear optics [12, 13]. Nonlinear optics examine the light propagation inside the nonlinear media. First nonlinear optical effects, such as two-photon absorption [14] and nonlinear quantum electrodynamics limit [15] were discussed in the 1930s, and the first nonlinear effects were experimentally observed only a decade later [16]. Nevertheless, nonlinear optics were propelled into modern physics with the invention of the laser in 1960 [17]. In the next year, both second harmonic generation [18] and two-photon absorption [19] were experimentally observed. The first theoretical model of nonlinear optics appeared in 1965 [20]. In 1973, Akira Hasegawa suggested the existence of the temporal solitons in the optical fibers [21]. Since then, nonlinear optics effects are observed in crystals, glasses, liquids, and gases [22]. One sub-field of nonlinear optics that deserves particular mention is nonlinear atom optics [23]. Particle-wave duality of the atoms was discovered theoretically by de Broglie [24] and shown experimentally by Stern [25]. Since then, physicists were trying to replicate optical phenomena in atomic matter. Observation of the four-wave mixing in atomic waves was the key experiment for the nonlinear atomic physics [26]. My thesis is based on the publications relevant to the fields of both classical and atomic nonlinear optics.

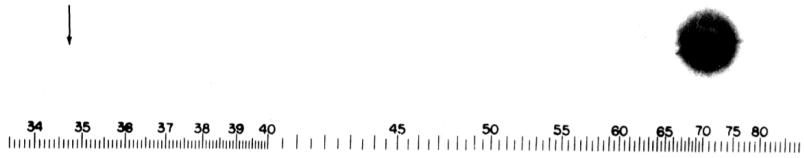

FIG. 1. A direct reproduction of the first plate in which there was an indication of second harmonic. The wavelength scale is in units of 100 A. The arrow at 3472 A indicates the small but dense image produced by the second harmonic. The image of the primary beam at 6943 A is very large due to halation.

FIGURE 1.2: First experimental observation of the nonlinear optical effect – second harmonic generation. Actual nonlinear signal was infamously mistaken for noise by the publisher and removed. After Ref. [18].

1.2 Nonlinear optical processes

Nonlinear effects in optics are usually established by expanding electric polarization into the power series of the electric field[27].

$$P = \chi^{(1)} \cdot E + \chi^{(1)} : E^2 + \chi^{(3)} \vdots E^3 + \dots \tag{1.2}$$

The order of nonlinearity is defined by the order of a power series of interacting fields. By this definition, first-order interaction is linear, KdV is an example of a second-order (quadratic) nonlinear system, and Nonlinear Schrödinger Equation (NLSE) is a third-order (cubic) nonlinear equation. Some nonlinear interactions, such as presented in Sine-Gordon equation [28] and Logarithmic Schrödinger equation [29], cannot be described by converging power series. In certain fields of mathematics, order of equation is defined through highest order of derivative [30] – NLSE is second-order in terms of derivative and third-order in terms of nonlinearity. In the following thesis, I will reference NLSE as a third-order nonlinear equation.

Third-order effects are particularly significant in nonlinear physics. In general, higher orders of nonlinearity require a bigger intensity of interacting fields, thus they are harder to induce [31]. Even then, third-order nonlinear effects appear alongside high-order terms [32, 33]. Second-order nonlinear effects, while having even smaller intensity requirements than third-order processes, are topologically limited. For example, second-order effects in nonlinear optics demand a lack of central symmetry in propagation media [22] – a condition that is not required by third-order processes. Furthermore, the cubic term describes phase-insensitive self-interaction. To conclude, third-order nonlinearity is the smallest nonlinear term applicable to every kind of optical media.

In general, both linear and nonlinear susceptibility tensors are anisotropic – dependent on the spatial orientation of the electric fields. Linear susceptibility is presented as a $3x3$ matrix, while third-order nonlinearity tensor has $3^4 = 81$ terms.

In practice, many nonlinear terms can be eliminated due to the symmetry considerations [34]. Anisotropy of the nonlinear refractive index is especially important in the crystalline structures and non-uniform media [35]. In my thesis, I assume the use of specific optical system geometries and precise optical field polarizations, stated in according chapters.

Nonlinear optical interactions usually require coherent light. The light source is considered coherent if it exhibits interference patterns in interaction with itself or other coherent sources, usually by maintaining identical frequency, waveform, and polarization. Incoherent nonlinear interactions are observed in some optical systems [36, 37], including liquid crystals [38]. In my thesis, I assume that all light sources are coherent. Instead, I use the word "coherent" as a substitute for "phase-sensitive". For example, the Kerr nonlinearity term $|E|^2$ is incoherent in the sense that it does not contain information about the phase of the electric field.

Nonlinear interactions may influence the amount of light or matter in the optical system. Optical interactions that change the number of particles are known as non-conservative. Examples of nonlinear non-conservative interactions include stimulated emission and two-photon absorption [22]. The process of increasing optical fields is called gain, while the decrease of the optical field is called loss. Exploration of gain and loss influence on the nonlinear system dynamics is one of the main goals of my thesis.

In most cases, nonlinear interactions are influenced only by the optical field in the exact place and time. These types of interactions are known as local. Nonlinear interactions can be temporally or spatially nonlocal. Temporal nonlocality means that the nonlinear response is not instantaneous and is influenced by the optical field from earlier moments. These interactions are often connected with optical scattering [39, 40]. Spatial nonlocality means that nonlinear interaction influences the whole area around the interaction region. This process is observed in the liquid crystals and photorefractive media [41]. Spatially nonlocal nonlinearities are the second main topic of my thesis.

1.3 Nonlinear Schrödinger Equation

My thesis is focused on the exploration of the Nonlinear Schrödinger Equation (NLSE). I use the abbreviation "NLSE" to describe families of both Nonlinear Schrödinger equations and closely related Gross-Pitaevskii equations. NLSE takes the following basic form

$$ik\partial_t\psi = -d\partial_{xx}\psi - \Gamma|\psi|^2\psi \tag{1.3}$$

In the equation above we used only one spatial dimension. However, in general, evolution depends on all three dimensions, and it is crucial to identify how many dimensions need to be included. Often dimensionality is presented as $(1+n)D$, where n is the amount of considered spatial dimensions, plus time as an additional dimension. Certain equations have strictly defined dimensionalities, such as Korteveg-de Vries (KdV) or Navier-Stokes equations. Other equations, such as NLSE or Klein-Gordon equations, can be applied to different numbers of dimensions. The dimensionality of the physical system influences its properties – solitons found in NLSE are stable in $(1+1)D$, unstable in $(1+2)D$, and non-existent for $(1+3)D$. I will focus on $(1+1)D$-dimensional systems in the following thesis.

NLSE-like equations are used in many fields of physical sciences [42, 43], such as atomic physics [44], superconductivity physics [45], meteorology [46], nonlinear optics [47] and hydrodynamics [48]. I would like to focus on two particular applications: Bose-Einstein Condensates (BEC) and high-intensity optics.

Bose-Einstein Condensate is an ultra-cold low-density state of matter, where multiple particles remain in the same quantum state, thus exhibiting quantum properties at macroscopic level [44, 49]. BEC was initially observed in cold atoms [50]. Nowadays media capable of supporting BEC include excitons – electron-hole pairs in semiconductors [51]; exciton-polaritons – quasiparticles, created by strong coupling between confined photons and excitons [52]; and magnons – quasiparticles of collective electron spin excitations in magnetic crystals [53]. In condensate physics, Gross-Pitaevskii equations model single boson wavefunction in pseudopotential under Hartree-Fock approximation [54].

$$i\hbar\partial_t\psi = \frac{-\hbar^2}{2m}\partial_{\vec{r}}^2\psi + V_{ext} + \sum_{j=2}^{N}\frac{4\pi\hbar^2 a_s}{m}\delta\left(\vec{r}-\vec{r}_j\right) \tag{1.4}$$

In this case, nonlinearity is introduced through many-body boson-boson interactions with negligible scattering lengths. To be more exact, the Gross-Pitaevskii equation describes a ground state of the single-particle wavefunction in variational approximation and its temporal dynamics.

NLSE is used in optics to describe light propagation in media with Kerr nonlinearity [22, 47]. The propagation of optical beams can be described by using paraxial approximation. Following equation models the spatial distribution of the monochromatic light beam.

$$2in_0k_0\partial_z E_0 = -\partial_{xx}E_0 - \left(n^2-n_0^2\right)k_0^2E_0 \tag{1.5}$$

Here, nonlinearity is contained in intensity-dependent refractive index $n =$

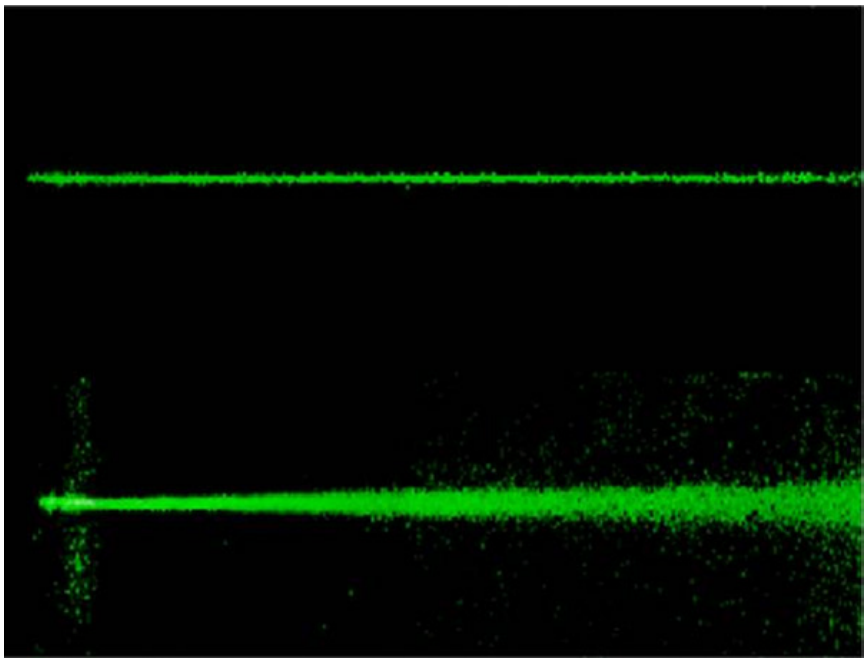

FIGURE 1.3: Formation of optical soliton beam (top) in the photorefractive medium. After Ref. [55].

$n_0 + n_2|E|^2$. A similar equation can be used to depict the transverse profile evolution of the optical pulse in time. Furthermore, a similar equation is used to model pulse propagation under a slowly varying envelope approximation. Instead of observing beam spatial distribution, we describe dependence in temporal pulse envelope structure from propagation distance, influenced by dispersion and Kerr nonlinearity.

$$i\partial_z A = \frac{\beta}{2}\partial_{tt} A + \gamma|A|^2 \tag{1.6}$$

Equations presented so far describe the evolution of the single element – beam, pulse, or condensate. In practice, we often observe multiple components interacting with each other. This interaction between components of the physical system is referred to as coupling, and solitons created by multiple interacting elements are called vector solitons [56]. Examples of vector solitons include condensates with two types of intrinsic spin structure [57], birefringent optical fibers with two polarization modes [58], and multicolor optical beams [59]. In my thesis, I focus on the two-component spatial vector solitons.

Basic NLSE can be easily extended to represent different physical processes. These modifications include high harmonic generation [60, 61], stimulated scattering processes [39, 40], self-steepening [62], four-wave mixing [63] and supercontinuum generation [64]. The introduction of several nonlinear effects simultaneously leads to systems with competing nonlinearities, which in turn provide additional points of equilibrium for stable soliton propagation. Examples of such models include competing local-nonlocal nonlinearities [65], quadratic-cubic [66] and cubic-quintic competing

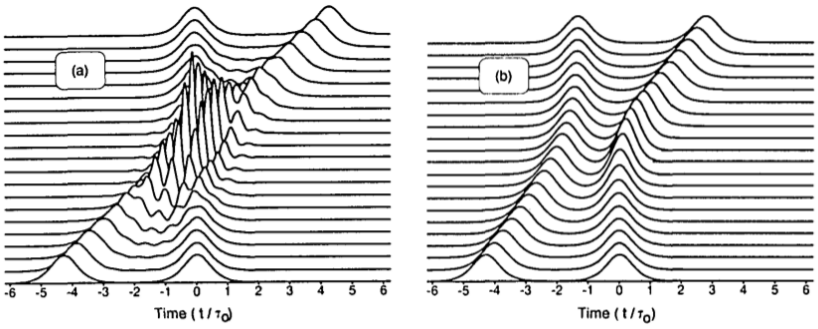

FIGURE 1.4: Simulation of bright soliton collision for in-phase solitons (left) and out-of-phase solitons (right). After Ref. [82].

nonlinearities [67, 68]. Other processes that stabilize solitons by preventing wavefunction over-concentration are nonlocality and saturable gain. In some media, such as liquid crystals and photorefractive materials, nonlinear interactions are nonlocal – function in each point is influenced not just by its value in this point, but also by its close vicinity [41, 69]. Other systems, such as polariton condensates and microresonators, introduce gain and losses – such systems are called non-conservative [70, 71]. Nonlocality and saturable gain are two specific effects that are analyzed in my thesis.

1.4 Solitons and nonlinear dynamics

Solitons are the most famous phenomena in nonlinear physics. Soliton can be defined as localized, shape-preserving excitation of nonlinear system. Since their discovery in water waves [72], solitons were observed in fluid dynamics [73], electronics [74], optics [75, 76], nuclear physics [77], quantum chemistry [78], and even microbiology [79] and neuroscience [80].

Soliton is an ambiguous term, its definition depends on the conventions of the chosen field of study. In the mathematical sense, a soliton is localized and stable excitation in the field, described by a partial differential equation, that maintains its shape and energy after arbitrary collisions with other solitons [81]. In experimental physics, such solitons are almost impossible to create. In practice, the definition of the soliton in the nonlinear optics is expanded to include all shape-preserving nonlinear excitations of the optical field, independent of their stability. I will use this definition of soliton – localized shape-preserving field excitation – in my thesis.

Under this definition of soliton, soliton stability becomes important for predicting its dynamics. For example, two-dimensional bright solitons in NLSE are unstable due to the catastrophic collapse – a small increase of the beam energy density focuses beam profile, further increasing energy density in the positive feedback loop [56]. Modulational instability – a process of nonlinear amplification of certain periodic sidebands [83] – is the type of instability inherent to the nonlinear systems. The modulational instability process typically leads to the fission of the background

excitation into the trail of several pulses. Modulational instability plays role in the creation of rogue surface waves [84] and the supercontinuum generation in fiber optics [85].

Certain solitons are partially stable to the external perturbations. However, as soliton is created under a certain combination of parameters, even small additional changes may lead to a different state. Large, qualitative change in system behavior, caused by a small change of the initial parameters, is known as bifurcation [86]. Phase transitions are the most popular examples of bifurcations [87]. Other examples of bifurcations are observed in the solid-state physics [88, 89], laser physics [90] and even cardiology [91].

Not every soliton state remains stationary. Conservative physical systems often have some form of oscillating solutions. However, only nonlinear systems feature stable permanently oscillating solutions, also known as limit cycle solutions. Limit cycle oscillations are not simply periodic – they are self-sustaining. In the case of stable limit cycle solutions, nonlinear systems naturally settle into an oscillating state. Limit cycle oscillations are present in aerodynamics [92], electronics [93], atomic physics [94], chemistry [95] and many instances of mathematical biology [96, 97, 98].

In certain cases, nonlinear system does not converge to either constant state or stable oscillation. Instead, we observe deterministic chaos – seemingly random irregular evolution, extremely sensitive to initial parameters [99]. Huge branch of mathematics, called chaos theory [100], explores chaos and its applications in, among other fields, meteorology [101], nanotechnology [102], astronomy [103], population dynamics [104], epidemiology [105], and even politics [106].

Multitude of solitons' variations was discovered over the decades, including breather solitons [107], multistable solitons [108, 109], Bragg solitons [110, 111], light bullets [112], vortex solitons [113, 114, 115] – and more general family of structured solitons [116, 117] – , parametric solitons [118], discrete solitons [119], incoherent or partially coherent solitons , dissipative solitons [120], self-written waveguide solitons [121], nonlocal solitons [122, 123] and more. Shape-preserving properties make solitons perfect means for information and matter transfer [124, 125] and even warp drive technology [126]. This thesis examines spatial solitons and accompanying nonlinear phenomena in physical systems modelled by Nonlinear Schrödinger Equations.

1.5 Thesis outline

Exploration of two-component spatial vector solitons in nonlocal and nonconservative media is the main purpose of my doctoral thesis. My research is divided into two categories: vector solitons in linearly coupled rings with saturable gain, based on exciton-polariton condensate systems, and multihump solitons in nonlocal media, based on nematic liquid crystals. In both cases, unusual dynamics, such as spontaneous vortex creation and trajectory bending, appear due to a lack of momentum conservation.

I present the fundamentals of vector soliton theory in Chapter 2. In it, I discuss types of scalar and vector solitons, soliton stability analysis, symmetry breaking, and integrals of motion. Conservation laws are expanded upon in Appendix 1.

Chapter 3 introduces numerical methods used in modeling coupled nonlinear systems. This chapter is separated into two parts – algorithms for finding solitons, and methods for exploring propagation in such systems. Several methods, such as finite difference, split-step, and imaginary time, are presented. The algorithm for one of the methods – Newton Conjugate Gradient – is tailored for coupled NLSE and derived in Appendix 2.

Chapter 4 shows an example of vector solitons in a conservative medium with local nonlinearity. Our model of two-channel coupled planar waveguides with nonlinear inclusions shows vector solitons with multiple types of symmetry breaking.

Chapter 5 explores our research on the coupled rings with saturated gain. It can be separated into three parts – model introduction, the case of homogeneous coupling, and the case of localized coupling. Homogeneously coupled rings present a rich variety of evolution scenarios, including limit cycle oscillations and chaotic behavior. Localized coupling allows for asymmetric oscillations resulting in spontaneous vortex generation.

Chapter 6 presents the results of exploring vector solitons in nematic liquid crystals. Instead of using a full system of equations for propagation, reorientation, and temperature, it is possible to apply a simplified model with nonlocal nonlinear effects. The family of multi-peak fundamental solitons is displayed. Bending of soliton trajectory emerges as a new type of instability, impossible in scalar soliton systems.

Chapter 2

Theory of solitons in coupled nonlinear systems

Solitary waves are localized excitations that preserve their shape during both free propagation and collisions with other solitons. Solitons are formed due to the mutual compensation of dispersive and nonlinear interactions. Dispersion tends to flatten any excitations. Nonlinear effect strength depends on local intensity, thus it amplifies present excitations.

Before further discussion, it is useful to introduce dimensionless form of NLSE, presented in equation (1.3), by rescaling coordinates as $Z = \frac{\Gamma}{k} z, X = \sqrt{\frac{\Gamma}{2d}} x$.

$$i\partial_Z \psi + \frac{1}{2}\partial_{XX}\psi \pm |\psi|^2 \psi = 0 \tag{2.1}$$

This form of rescaling assumes that k, d, Γ are real numbers. This presumption infers a lack of external amplification of attenuation and is often referred to as hermiticity.

The exact form of the soliton depends on the direction of nonlinear interactions. If nonlinear and diffraction terms have the same sign, nonlinearity has a focusing effect. In this case, we observe localized peaks of bright solitons [127]. If the nonlinear term sign is opposite to the diffraction sign, we observe respectively defocusing nonlinearity and dark solitons – localized low-intensity areas within constant background [128].

Not every soliton maintains its shape constant at every moment. Only fundamental solitons, also known as first-order solitons, maintain constant phase front and thus constant shape. It is possible to observe higher-order temporal solitons – solitons with periodically oscillating structure [56, 129]. In my thesis, I will focus purely on fundamental solitons.

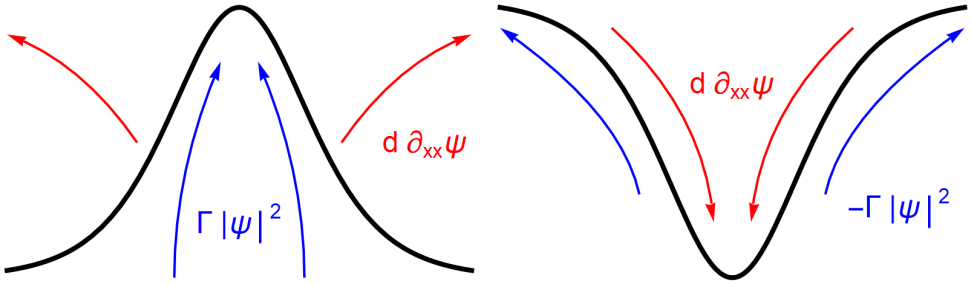

FIGURE 2.1: Schematic representation of diffraction term (red) and nonlinear term (blue) influence on the formation of bright (left) and dark (right) solitons.

Fundamental solitons can be separated into phase oscillation and transverse distribution term $u(x)$

$$\psi(x,z) = u(x)e^{i\mu z + i\beta x} \tag{2.2}$$

where β is transverse propagation velocity and μ is propagation constant. Physical interpretation of the propagation constant depends on the modeled system – in optics, μ is phase or group velocity for spatial and temporal solitons respectively, while in BEC μ is interpreted as chemical potential.

2.1 Integrals of motion - scalar case

Solutions of NLSE typically have multiple time-independent integrals of motion, also known as constants of motion. According to Noether's theorem, each constant of motion corresponds to a certain system symmetry [130]. Popularly considered constants of motion with simple physical interpretations are norm, energy, and momentum [30].

Norm is defined as total wavefunction intensity $N = \int_{-\infty}^{\infty} |\psi|^2 dx$. Norm is analogous to the amount of matter, particles, or probability density in the system. Norm can be changed by interaction with the outside world or coupling with other systems. Any coefficient in the equations with imaginary factor leads to gain or loss and norm, in general, is not conserved. The second mechanism of norm change is coherent coupling, which will be discussed later. If the initial system is hermitian, then the norm of the localized solution is conserved.

The next constant of motion is total system energy. Its formulation slightly depends on the exact form of NLSE. In case of equation (2.1) energy is defined as following

$$E = \frac{1}{2}\int_{-\infty}^{\infty} |\partial_x \psi|^2 \mp \Gamma |\psi|^4 dx \tag{2.3}$$

Momentum is defined as the total current of the wavefunction. Conservation of momentum requires additional assumption – neither dispersion nor nonlinearity coefficients can be non-constant.

$$M = \int_{-\infty}^{\infty} j dx = i \int_{-\infty}^{\infty} \left(\psi \partial_x \psi^* - \psi^* \partial_x \psi\right) dx \tag{2.4}$$

2.2 Scalar solitons

Equation (2.1) belongs to the category of integrable equations, as it can be solved by using inverse scattering method [131] or soliton perturbation theory [132]. The inverse scattering method allows us to derive bright and dark solitons for scalar NLSE. However, most modifications of NLSE are non-integrable and require numerical calculations to find possible solitons. These methods will be thoroughly discussed in the next chapter.

For simplicity of derivation I assume $\beta = 0$, constant phase front ($u \in \mathcal{R}$) and focusing nonlinearity. First, we substitute separated wavefunction (2.2) into (2.1).

$$-\mu u + \frac{1}{2}\partial_x x u + u^3 = 0 \tag{2.5}$$

The next step is to multiply the equation by $4\partial_x u$.

$$2\partial_x u \partial_{xx} u = 4u\partial_x u - 4u^3 \partial_x u \tag{2.6}$$

This equation is simplified by applying $\partial_x u^2 = 2u\partial_x u$ and integrating over x

$$(\partial_x u)^2 = 2\mu u^2 - u^4 + C \tag{2.7}$$

Integration constant C is assumed to be zero, as $u|_{x=\pm\infty} = \partial_x u|_{x=\pm\infty} = 0$. Remaining differential equation has a solution in form $u = a\,\mathrm{sech}(ax)$.

Similar calculations can be performed for self-defocusing nonlinearity. In this case, instead of the localized peak, we observe localized dip with phase shift in the constant background. Complete formulas for bright and dark solitons take the following form

$$\psi_b = \psi_0 \,\mathrm{sech}\left[a\left(X - vZ\right)\right] e^{ivX} \exp\left(i\frac{a^2 - v^2}{2} Z\right)$$
$$\psi_d = \psi_0 \left[\tanh\left(\psi_0\left[X - \psi_0 \sin\phi Z\right]\cos\phi\right)\cos\phi + i\sin\phi\right] e^{-i\psi_0^2 Z} \tag{2.8}$$

where ψ_0 is maximal amplitude, a is bright soliton width, v is bright soliton velocity, and ϕ is dark soliton phase shift parameter.

2.3 Linear stability analysis

As mentioned in the introduction, "solitons" in their physical sense are not guaranteed to endure external interactions. Soliton stability is required to ensure its robustness to unavoidable external perturbations. Nonlinear systems are particularly prone to modulational instability – spontaneous nonlinear amplification of certain background frequencies.

The easiest, brute-force way to confirm stability is to simulate the propagation of soliton with the small random perturbation. Analytical criteria for stability analysis are based on perturbation theory. The most popular method for integrable systems is linear stability analysis [133].

To provide an example of linear stability analysis, I will consider trivial plane wave background in NLSE. It is easy to show that $\psi = \psi_0 e^{i\beta X + i\mu Z}$ is a solution for NLSE, as long as $\mu = \psi_0^2 - \frac{\beta^2}{2}$. The first step of stability analysis is an introduction of perturbation.

$$\psi_{per} = e^{i\beta X + i\mu Z}\left[\psi_0 + U(X)e^{\lambda Z} + V^*(X)e^{\lambda^* Z}\right] \tag{2.9}$$

Here U, V are complex functions of X, representing perturbation distribution. These functions should form a complete basis, to cover every possible perturbation that can be created due to random noise. λ is a parameter responsible for perturbation component dynamics. If $\Re(\lambda) > 0$, this perturbation will increase during propagation, leading to state instability.

Next step is to substitute (2.9) into (2.1) and linearize the equation in terms of $U, V \ll 1$. Nonlinear term is linearized in the following manner

$$\begin{aligned}|\psi_{per}|^2\psi_{per} = \psi_0^2 e^{i\beta X + i\mu Z}\Big[\psi_0 + 2Ue^{\lambda Z} + 2V^* e^{\lambda^* Z} + \\ + U^* e^{\lambda^* Z} + Ve^{\lambda Z}\Big] + \mathcal{O}\left(U^2, V^2, UV\right)\end{aligned} \tag{2.10}$$

The linearized equation can be separated according to exponential terms.

$$\left[i\lambda U + \frac{1}{2}\partial_{XX}U + \psi_0^2\left(U+V\right)\right]e^{\lambda Z} + \left[i\lambda^* V^* + \frac{1}{2}\partial_{XX}V^* + \psi_0^2\left(U^*+V^*\right)\right]e^{\lambda^* Z} = 0 \tag{2.11}$$

This relation is maintained at every point of propagation, which is possible only if both terms in square parentheses are simultaneously equal to zero. Furthermore, we represent perturbation in the basis of plane waves $U, V = U_0, V_0 e^{ikX}$. This allows to transform equation (2.11) into the following eigenproblem.

$$\begin{bmatrix} i\psi_0^2 - i\frac{k^2}{2} & i\psi_0^2 \\ -i\psi_0^2 & i\frac{k^2}{2} - i\psi_0^2 \end{bmatrix} \begin{bmatrix} U_0 \\ V_0 \end{bmatrix} = \lambda \begin{bmatrix} U_0 \\ V_0 \end{bmatrix} \tag{2.12}$$

with following eigenvalues

$$\lambda = \pm\frac{k}{2}\sqrt{4\psi_0^2 - k^2} \tag{2.13}$$

This analysis shows that perturbation waves with $|k| < 2\psi_0$ become amplified. This modulational instability leads to the generation of the periodic bright solitons.

Finally, linear stability analysis can be generalized for arbitrary soliton states. For single-peak fundamental solitons this generalization leads to Vakhitov-Kolokolov stability criterion [134]

$$\partial_\mu N > 0 \tag{2.14}$$

where N is the soliton norm. Vakhitov-Kolokolov stability criterion can also be applied to modified versions of NLSE, as long as the nonlinearity term can be described by a function of $|\psi|^2$ [135].

2.4 Vector solitons

The analysis presented above considered single component scalar solitons. This model requires purification and separation of possible parameters – for example, optical scalar solitons are monochromatic and maintain single polarization. If these components are not separated, we observe multicomponent coupled solitons – vector solitons. In this thesis, I will focus on two-component vector solitons.

Two coupled NLSE can be generalized to take the following form

$$\begin{cases} i\partial_t\psi_1 = d_1\partial_{xx}\psi_1 + \gamma_1\psi_1 + \Gamma_1|\psi_1|^2\psi_1 + \kappa_1\psi_2 + C_1|\psi_2|^2\psi_1 + K_1\psi_2^2\psi_1^* \\ i\partial_t\psi_2 = d_2\partial_{xx}\psi_2 + \gamma_2\psi_2 + \Gamma_2|\psi_2|^2\psi_2 + \kappa_2\psi_1 + C_2|\psi_1|^2\psi_2 + K_2\psi_1^2\psi_2^* \end{cases} \tag{2.15}$$

Here d_m is diffraction coefficient, γ_m is linear potential, Γ_m is nonlinear self-phase modulation term, κ_m is linear coupling term, C_m is nonlinear incoherent coupling term, and K_m is nonlinear coherent coupling coefficient. All coefficients $d, \gamma, \Gamma, \kappa, K, C$ are functions – or, in case of nonlocal systems, distributions – of x.

In most cases, one coupling type dominates over other terms. Linear coupling κ appears due to the modal approach. In certain systems, such as collinear waveguides, the nonlinear term can be simplified by specific components definition, at a cost of introducing linear coupling term. Coherent coupling term K represents phase-sensitive processes that appear in weakly anisotropic birefringent media. Incoherent coupling C appears as the result of phase-insensitive refractive index change, such as the Kerr effect or molecular reorientation in anisotropic media.

Many different types of vector solitons can be observed depending on the nonlinearity. If nonlinear terms in both channels maintain the same sign, we observe vector bright solitons [136] and vector dark solitons [137] for focusing and defocusing interactions respectively. Other possibilities include mixed bright-dark solitons in media with opposing nonlinearities [138], multihump solitons [139] and waveguides induced by both bright [140] and dark [141] solitons.

Linear stability analysis can still be applied to vector solitons. For example, in the case of NLSE with incoherent coupling Vakhitov-Kolokolov criterion can be expanded to the condition for Hessian matrix [133].

$$H_{mn} = \frac{\partial N_m}{\partial \mu_n} > 0 \text{ for every } m, n \tag{2.16}$$

Additional modes of instability occur in vector solitons. One of such examples is walk-off instability – separation of soliton components due to discrepancy in group velocities [142]. Overall, linear stability analysis is much more complicated in vector NLSE.

2.4.1 Constants of motion in coupled NLSE

Integrals of motion, previously discussed for the scalar case, can still be applied to vector solitons. In vector systems, total norm $N = N_1 + N_2$, total momentum $M = M_1 + M_2$ and total energy E are conserved under certain conditions. Hermiticity of coupled NLSE – lack of imaginary terms in all dispersion, potential and coupling coefficients – and action-reaction symmetry ($C_1 = C_2, \kappa_1 = \kappa_2, K_1 = K_2$) are sufficient conditions for norm and energy conservation. Momentum conservation additionally requires that neither potential nor coupling terms depend on x. Complete derivation conservation laws and conditions for coupled NLSE are presented in Appendix 1.

Integrals of motion for each channel separately are not conserved, as components actively interact with each other. Energy cannot be defined for a single channel and has to be reformulated for the whole system.

$$E = \int_{-\infty}^{\infty} \left[-d_1|\partial_x\psi_1|^2 - d_2|\partial_x\psi_2|^2 + \gamma_1|\psi_1|^2 + \gamma_2|\psi_2|^2 + \right. \\ \left. + \frac{\Gamma_1}{2}|\psi_1|^4 + \frac{\Gamma_2}{2}|\psi_2|^4 + \kappa\left(\psi_1\psi_2^* + \psi_1^*\psi_2\right) + K|\psi_1|^2|\psi_2|^2 \right] dx \quad (2.17)$$

Norm is a particular integral of motion that can be conserved for each component under particular circumstances. The norm in each channel is changed by interaction with the outside world or coupling with other systems. Any coefficient in the equations with imaginary factor leads to gain or loss and norm, in general, is not conserved. The second mechanism of norm change is coherent coupling, both linear and nonlinear. The current between channels can be described as following:

$$J_\perp = \int_{-\infty}^{\infty} j_\perp dx = -i\int_{-\infty}^{\infty} \kappa_1\left(\psi_1^*\psi_2 - \psi_2^*\psi_1\right) + K_1\left(\left[\psi_1^*\psi_2\right]^2 - \left[\psi_2^*\psi_1\right]^2\right) dx \quad (2.18)$$

Incoherent coupling does not influence inter-channel current – if a system is hermitian and coherent coupling is absent, the norm is also conserved in each channel separately.

Chapter 3

Numerical methods for coupled nonlinear systems simulation

Coupled NLSE in general are non-integrable and cannot be solved analytically. Numerical methods are required to explore such systems. Some algorithms assume linear differential equations and thus cannot be used for NLSE. A vast array of techniques was developed to solve specifically nonlinear differential equations [143, 144, 145].

This section will be divided into two parts. The first part explains basic approaches to initial value problems – simulating propagation in a system for a known state. The second part considers boundary value problems – methods for finding soliton states.

3.1 Propagation methods

Simulations are the fundamental way of exploring state evolution in physical systems. Many algorithms were developed for initial value problems, such as Galerkin method [146], method of lines [147] and meshless methods [148]. In my thesis, I will discuss two main families of approaches – finite difference (FD) methods and spectral methods. I will use the following notation for two coupled NLSE.

$$i\partial_t \psi_m = d_m \partial_{xx} \psi_m + N_m \tag{3.1}$$

where $m \in \{1, 2\}$ is channel index, and $N_m = \gamma_m \psi_m + \Gamma_m |\psi_m|^2 \psi_m + \kappa_m \psi_{3-m} + C_m |\psi_{3-m}|^2 \psi_m + K_m \psi_{3-m}^2 \psi_m^*$ is total potential and coupling term.

Both FD and spectral methods require the creation of mesh – discretization of space and time coordinates onto a grid. Typically mesh grids are uniform. Size of mesh step is the key parameter of a simulation – smaller step size increases accuracy at time and memory cost.

3.1.1 Finite difference methods

The main idea of the FD methods is to present derivatives as finite differences on the established mesh. The simplest example of the FD algorithm is the forward-time centered-space (FTCS) scheme. To use it, we substitute the following definitions of derivatives into (3.1)

$$\partial_t \psi_{m(x,t)} = \frac{\psi_{m(x,t+1)} - \psi_{m(x,t)}}{\Delta t}$$

$$\partial_{xx} \psi_{m(x,t)} = \frac{\psi_{m(x+1,t)} + \psi_{m(x-1,t)} - 2 * \psi_{m(x,t)}}{(\Delta x)^2} \tag{3.2}$$

where $\psi_{m(x,t)}$ represent wavefunction in particular mesh point (x,t).

FTCS is called an explicit scheme because every point in the next step explicitly depends only on previous points. Even though it's simple, FTCS has problems with its stability and accuracy. This method has second-order accuracy in space and only first-order accuracy in time. Furthermore, if the time step is not small enough, this method becomes numerically unstable [144]. The largest possible time step is defined by the von Neumann stability condition:

$$\frac{d\Delta t}{\Delta x^2} \leq \frac{1}{2} \tag{3.3}$$

One way to fix stability issues is to use implicit methods. In implicit schemes, the future state depends on both the previous and the new state. The most famous example is the Crank-Nicholson algorithm, which is based on averaging implicit and explicit time steps [149].

$$i\frac{\psi_{m(x,t+1)} - \psi_{m(x,t)}}{\Delta t} =$$

$$= d_m \frac{\psi_{m(x-1,t+1/2)} + \psi_{m(x+1,t+1/2)} - 2\psi_{m(x,t+1/2)}}{\Delta x^2} + N_{m(x,t+1/2)} \tag{3.4}$$

where $\psi_{m(x,t+1/2)} = \frac{\psi_{m(x,t+1)} + \psi_{m(x,t)}}{2}$.

The biggest benefit of this method is that it's always numerically stable. The downside is that these equations are much harder to solve for nonlinear systems – it is impossible for general coupled NLSE. Solutions used for intrinsic methods are approximated by linearizing solved equations. One example of linearization is Newton's method.

$$\psi_{m(t+1)} = \psi_{m(t)} - \omega \frac{F\left(\psi_{m(t)}\right)}{F'\left(\psi_{m(t)}\right)} \tag{3.5}$$

where ω is relaxation parameter [150], and $F(\psi_m) = i\partial_t\psi_m - d_m\partial_{xx}\psi_m - N_m$ is defined depending on differentiation algorithm.

Numerical methods used for coupled NLSE are typically extrinsic, as problems of stability can be overcome by simpler means. Issue of accuracy in explicit methods can be corrected through intermediate point calculations. Generally, calculations with intermediate points belong to the family of Runge-Kutta (RK) methods [144]. The simplest example is RK2, also known as the "midpoint method". RK2 calculates state at $(t + 1/2)$ step and uses it to calculate time derivative. Most popular is the RK4 method, which is relatively easy to implement and has a fourth-order of accuracy in time.

$$\begin{aligned} \frac{\psi_{m(t+1)} - \psi_{m(t)}}{\Delta t} &= \frac{k_1 + 2k_2 + 2k_3 + k_4}{6} \\ k_1 &= f(\psi_{m(t)}) \\ k_2 &= f(\psi_{m(t)} + k_1\Delta t/2) \\ k_3 &= f(\psi_{m(t)} + k_2\Delta t/2) \\ k_4 &= f(\psi_{m(t)} + k_3\Delta t) \end{aligned} \tag{3.6}$$

where $f(\psi_m) = -i\left(d_m\partial_{xx}\psi_m + N_m\right)$.

Runge-Kutta methods can be upgraded in different manners. It is possible to derive intrinsic RK methods, even though they are not used in nonlinear systems [151]. Another useful upgrade is the adaptive time step, for example, Runge-Kutta-Fehlberg method [152]. The adaptive time step allows shortening simulation time by focusing on more dynamic parts of the simulation.

3.1.2 Spectral methods

Spectral methods substitute explicit differentiation of FD methods by using the following property of Fourier Transform (FT).

$$\partial_{xx}\psi = \mathcal{F}^{-1}\left((ik)^2\tilde{\psi}\right) \tag{3.7}$$

where $\tilde{\psi} = \mathcal{F}(\psi)$. We can use the Fast Fourier Transform algorithm [153] to calculate space derivatives faster than using the FD approach. The downside of this method is that its accuracy decreases in presence of discontinuous or complex potentials, as they depend on Fourier transforms. Another thing to consider is that FT assumes periodic boundary conditions. In practice, we can assume periodicity if a solution is well localized. Additional damping, such as Evanescent Boundary

Conditions [154] can be introduced on simulations borders to eliminate radiative waves.

The combination of spectral approach for space derivative and Runge-Kutta for time propagation is known as pseudospectral method [143]. Properties and modifications of RK methods before – explicit calculations, fourth-order of accuracy, adaptive time step – can be applied in the pseudospectral method. Stability condition for spectral methods takes a slightly different form:

$$\frac{\Delta t}{\Delta x^2} \leq \frac{2\sqrt{2}}{\pi^2} \tag{3.8}$$

It is possible to modify the system even further by performing FT of NLSE and using substitution $\tilde{\psi_m} = \tilde{\phi_m} e^{id_m k^2 t}$. This leads to integrating-factor method:

$$\partial_z \tilde{\phi_m} = -ie^{-id_m k^2 t} \mathcal{F}(N_m) \tag{3.9}$$

This method is slightly more stable than the pseudospectral method. The integrating-factor method should be used when potential, nonlinearity, and coupling coefficients do not depend on x.

3.1.3 Split-step methods

Split-step methods are popular alternatives to finite difference and pseudospectral methods. Split-Step Fourier Method (SSFM) uses a spectral approach for space derivative and evolution operators instead of finite time differences. A general idea of SSFM is to calculate propagation using a unitary evolution operator

$$\hat{\psi}_{(t+\Delta t)} = e^{-i(\hat{D}+\hat{N})\Delta t} \hat{\psi}_{(t)} \tag{3.10}$$

where $\hat{\psi} = \begin{bmatrix} \psi_1 \\ \psi_2 \end{bmatrix}$ is state vector, $\hat{D} = \begin{bmatrix} d_1 \partial_{xx} \psi_1 & 0 \\ 0 & d_2 \partial_{xx} \psi_2 \end{bmatrix}$ is dispersive operator and

$$\hat{N} = \begin{bmatrix} \gamma_1 + \Gamma_1 |\psi_1|^2 + C_1 |\psi_2|^2 & \kappa_1 + K_1 \psi_1^* \psi_2 \\ \kappa_2 + K_2 \psi_2^* \psi_1 & \gamma_2 + \Gamma_2 |\psi_2|^2 + C_2 |\psi_1|^2 \end{bmatrix} \tag{3.11}$$

is the nonlinear operator.

The "Split-step" approach is based on the idea that we can calculate evolution for both operators separately. Baker–Campbell–Hausdorff formula [155] allows us to present total evolution as series of interchanging operators

$$e^{(\hat{D}+\hat{N})\Delta t} \simeq e^{\alpha_1 \hat{D} \Delta t} e^{\beta_1 \hat{N} \Delta t} \ldots e^{\alpha_n \hat{D} \Delta t} e^{\beta_n \hat{N} \Delta t} \tag{3.12}$$

The most popular variation of SSFM is symmetrical split-step [156], also known as Strang splitting.

$$\psi_{t+\Delta t} = e^{-i\hat{D}\Delta t/2} e^{-i\hat{N}\Delta t} e^{-i\hat{D}\Delta t/2} \psi_t \tag{3.13}$$

This method is second-order accurate in time. SSFM method with fourth-order time accuracy takes the following form.

$$\psi_{t+\Delta t} = e^{-i\frac{c_1}{2}\hat{D}\Delta t} e^{-ic_1\hat{N}\Delta t} e^{-i\frac{1-c_1}{2}\hat{D}\Delta t} e^{-i(1-2c_1)\hat{N}\Delta t} \times \\ \times e^{-i\frac{1-c_1}{2}\hat{D}\Delta t} e^{-ic_1\hat{N}\Delta t} e^{-i\frac{c_1}{2}\hat{D}\Delta t} \psi_t \tag{3.14}$$

where $c_1 = \dfrac{1}{2-\sqrt[3]{2}}$.

SSFM is an explicit method and has slightly less straining stability condition.

$$\frac{\Delta t}{\Delta x^2} \leq \frac{1}{\pi} \tag{3.15}$$

SSFM can be modified to introduce adaptive step size [157]. Additionally, SSFM maintains both norm and energy in long-term simulations of conservative systems. It has similar downsides as other spectral methods.

3.2 Soliton relaxation methods

If we can't solve equations analytically (and usually we can't), we need numerical methods to find soliton states in our system. Because original equations are nonlinear, we can't simply solve the eigenproblem – we need some original guess of the state. There are several techniques, such as finite elements analysis [158], Petviashvili method [159] or Modified Squared Operator method [160]. In this work I will focus on two techniques: Imaginary Time methods [161] and Newton Conjugate Gradient method [162].

3.2.1 Imaginary time method

Imaginary Time Evolution Method (ITEM) is based on the change of standard propagation in time t into fictitious diffusion in imaginary time it. In this case, different components of the initial state will vanish at different speeds, with the slowest decline for the fundamental state. If we renormalize the norm with every step, the resulting state will slowly converge into the fundamental soliton of a physical system. This gives us an algorithm for the classic imaginary time method.

$$\psi_{m(n+1)} = \sqrt{\frac{P}{\int |\psi_{m(n+1)}|^2 dx}} \left[\psi_{m(n)} + \Delta t L_0 \psi_{m(n)}\right] \tag{3.16}$$

where $\psi_{m(n)}$ is n-th iteration of the wavefunction, $P = \int |\psi_{m(0)}|^2 dx$ is initial power, and $L_0\psi_{m(n)} = d_m \partial_{xx}\psi_{m(n)} + N_m$ is propagation operator.

The biggest benefit of this method is the ability to easily repurpose propagation code for the imaginary time method. Such an algorithm can be based on any of the previously discussed methods, such as Split-Step or Finite Difference. However, standard ITEM is very slow, as stability conditions require very small time steps. This issue could be fixed by using implicit methods of propagation, but in nonlinear systems, we encounter the same problems as in propagation equations. Another limitation of imaginary time methods is that it converges only for fundamental solitons, and thus it's impossible to find excited states and higher-order solitons with this method.

The imaginary time method can be accelerated by using a preconditioning operator and accounting for phase velocity on every time step. In this case equation for Accelerated Imaginary Time Evolution Method (AITEM) takes the following form

$$\partial_t \psi_m = M^{-1} \left(L_0 \psi_m - \mu \psi_m\right) \tag{3.17}$$

where $\mu = \dfrac{\int \left(M^{-1}\psi_m^*\right) L_0 \psi_m dx}{\int \left(M^{-1}\psi_m^*\right) \psi_m dx}$ is phase velocity of soliton and M is self-adjoint, positive-definite and easily invertible preconditioning operator. In case of spectral methods standard choice of preconditioning operator is $M = c - \partial_{xx}$, because $M^{-1}\psi = \mathcal{F}^{-1}\left(\dfrac{\tilde{\psi}}{c + k^2}\right)$. c is positive constant adjusted manually to particular problems. In case of localised potentials $c \simeq \mu$ leads to fastest convergence results.

AITEM is significantly faster than classic ITEM. Furthermore, conditions for convergence of AITEM intersect with conditions for linear stability of fundamental soliton. Therefore, we can guarantee that solitons generated from AITEM are linearly stable.

3.2.2 Newton Conjugate Method

Newton Conjugate Gradient (NCG) method is in general even faster than AITEM. NGG method is based on iterative linearization of the original equation using the Newton method, described above. This leads to a linearized set of equations.

$$L_1 \begin{bmatrix} \delta_{1(n)} \\ \delta_{2(n)} \end{bmatrix} = L_0 \begin{bmatrix} \psi_{1(n)} \\ \psi_{2(n)} \end{bmatrix} \tag{3.18}$$

where L_0 is full nonlinear operator, L_1 is its linearized version and $\delta_{m(n)} = \psi_{m(n+1)} - \psi_{m(n)}$ is error correction term. Equation for error correction is solved through conjugate gradient method [163]. Complete derivation of linearization operator and conjugate gradient iterations is presented in Appendix 2.

NCG method has several benefits - it is orders of magnitude faster than AITEM and it can be used to find higher-order solitons. The biggest drawback of NCG is its relatively complicated implementation algorithm. Furthermore, NCG methods are not convergent in a strict sense, thus in some rare cases, this method requires subtle adjustments to achieve sensible results, especially in cases of linear coupling. In particular, the NCG method assumes the hermiticity and coupling symmetry of the original system. In the case of non-conservative systems, NCG is substituted by the biconjugate gradient stabilized method [164].

Chapter 4

Vector solitons in planar waveguides with nonlinear inclusions

This chapter introduces our research on coupled planar waveguides with sub-wavelength nonlinear inclusions, presented in [165]. The goal of this chapter is to introduce an example of vector solitons with analytical solutions before studying non-conservative and nonlocal systems. Additionally, this model serves as an example of several types of symmetry breaking.

Even though the system itself can be symmetrical, states in the system don't have to be. Spontaneous symmetry breaking (SSB) is a process, by which symmetry of the ground state differs from system symmetry [166]. SSB can be observed in both linear and nonlinear systems. In nonlinear systems, symmetry of the ground state may depend on state energy, thus allowing for energy-dependent bifurcation curves. Symmetry breaking can appear slowly, through a subcritical phase change, or with a supercritical phase change – sudden qualitative jump due to the instability of intermediary states [167]. SSB is used in nano-optics to create optoelectronic devices and regulate the strength of the nonlinear effects [168].

Both one-dimensional BEC traps and planar optical waveguides are modeled by linearly coupled equations with nonlinear inclusions. In this chapter, I will focus on model derivation from the integrated optics' point of view.

4.1 Planar waveguides

The technology of guiding light through the total internal reflection was invented in the 19th century, but waveguide and fiber optics started to develop only after the formulation of electromagnetism theory [169]. Nowadays, planar waveguides are the essential blocks used in integrated optics [170, 171].

A basic planar waveguide is constructed from slabs of optically dense material inside the substrate with a smaller refractive index. Refractive index difference serves as a potential trap, confining light beam in transverse directions. Examples of planar waveguides are shown in Figure (4.1).

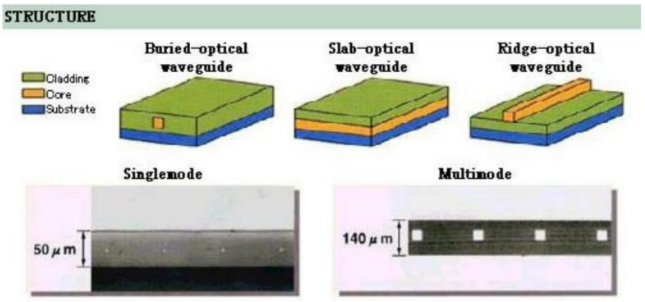

FIGURE 4.1: Schematic representation of the planar waveguides (top) and photos of silicon-based waveguides (bottom). Image from NTT-AT archives www.keytech.ntt-at.co.jp/optic2/prd_e0015.html.

Propagation in planar waveguides follows modified Helmholtz equation with slowly varying envelope approximation [172]

$$i\beta\partial_z E = \partial_{xx}E + \left(\frac{4\pi^2\omega^2}{c^2}n^2(x) - \beta^2\right)E - \mu_0\omega^2 P_{pert} \tag{4.1}$$

where E is the scalar electric field component of the monochromatic wave with frequency ω, β is the mode propagation constant, and $n(x)$ is the linear refractive index. This formulation assumes that waveguide structure confines light in the y direction and mode distribution in this direction is eliminated through the separation of variables.

Perturbation polarization P_{pert} is combined from different terms, depending on the underlying mechanism. In this chapter I focus on two perturbation terms – nonlinearity term P_{nl} and coupling term P_{cp}. Nonlinear polarization appears due to the third-order process [22].

$$P_{nl} = \epsilon_0 \hat{\chi}^{(3)} \vdots E^3 \tag{4.2}$$

If phase-matching conditions are not satisfied, third harmonic generation process becomes negligible and we can simplify tensor multiplication down to the Kerr nonlinearity $P_{nl} = \epsilon_0\chi^{(3)}|E|^2E$. Nonlinear effects can be introduced in localized spots of the waveguide through the holographic techniques [173] or through the doping processes [174].

Coupling polarization P_{cp} is calculated by applying the Coupled Mode Theory (CMT) [175]. CMT models a system of multilayer stacked waveguides as a combination of single waveguide solutions and perturbations introduced by the presence of the other waveguides $n_{1+2}(x,y) = n_1 + \Delta n_2 = n_2 + \Delta n_1$. Polarization perturbation appears due to the overlap of the second channel mode with the first channel structure perturbation and vice versa.

$$P_{cp,1} = \epsilon_0 \Delta n_1^2 E_2 \tag{4.3}$$

Substitutions of polarization terms into equations 4.1 and following rescaling lead to a system of dimensionless equations

$$\begin{cases} i\partial_z \psi_1 + \frac{1}{2}\partial_{xx}\psi_1 + g(x)|\psi_1|^2\psi_1 + \kappa\psi_2 = 0 \\ i\partial_z \psi_2 + \frac{1}{2}\partial_{xx}\psi_2 + g(x)|\psi_2|^2\psi_2 + \kappa\psi_1 = 0 \end{cases} \tag{4.4}$$

where $g(x)$ is nonlinear doping distribution function. Total norm and energy are defined in the following manner.

$$N = \int_{-\infty}^{\infty} \left[|\psi_1|^2 + |\psi_2|^2\right] dx \tag{4.5}$$

$$E = \frac{1}{2}\int_{-\infty}^{+\infty} \left[|\partial_x\psi_1|^2 + |\partial_x\psi_2|^2 + g\,(x)\left(|\psi_1|^4 + |\psi_2|^4\right) - 2\kappa\left(\psi_1\psi_2^* + \psi_1^*\psi_2\right)\right] dx \tag{4.6}$$

Nonlinear material distribution is often modelled as a sum of Gaussian-shaped inclusions $g(x) = \sum_m \frac{G_m}{w_m\sqrt{\pi}} \exp\left(\frac{-(x-x_{0m})^2}{w_m^2}\right)$. If the inclusion size is much smaller than optical wavelength, Gaussian distribution approaches Dirac Delta function $\delta(x_{0m})$. Introduction of Dirac Delta distributions allows to solve system of equations 4.4 analytically. Following sections present soliton states for single-delta and double-delta cases respectively. Final section presents numerical examples of symmetry-breaking in two-dimensional rectangular waveguide structure.

4.2 Single-delta waveguides

The following set of equations models two parallel waveguides stacked on top of each other, each with single subwavelength nonlinear inclusion in $x = 0$.

$$\begin{cases} i\partial_z \psi_1 + \frac{1}{2}\partial_{xx}\psi_1 + \delta(x)|\psi_1|^2\psi_1 + \kappa\psi_2 = 0 \\ i\partial_z \psi_2 + \frac{1}{2}\partial_{xx}\psi_2 + \delta(x)|\psi_2|^2\psi_2 + \kappa\psi_1 = 0 \end{cases} \tag{4.7}$$

To find soliton states, we assume stationary solutions with constant phase velocity

$$\psi_m(x,t) = \phi_m(x)e^{-i\mu t} \tag{4.8}$$

and substitute them into equations (4.7).

$$\begin{cases} \mu\phi_1 = -\frac{1}{2}\partial_{xx}\phi_1 - \delta(x)|\psi_1|^2\phi_1 - \kappa\phi_2 \\ \mu\phi_2 = -\frac{1}{2}\partial_{xx}\phi_2 - \delta(x)|\phi_2|^2\phi_2 - \kappa\phi_1 \end{cases} \tag{4.9}$$

Nonlinearity is present only in $x = 0$, thus we can solve equations at every other point and then enforce continuity. Outside of nonlinear influence we can represent coupled system in basis of $w_1 \equiv \phi_1 + \phi_2$ and $w_2 \equiv \phi_1 - \phi_2$.

$$\begin{cases} \partial_{xx} w_1 = \mu_+ w_1 \\ \partial_{xx} w_2 = \mu_- w_2 \end{cases} \tag{4.10}$$

where $\mu_\pm = -2(\mu \pm k)$. We can easily solve 4.10 and substitute exponential solutions into 4.9.

$$\phi_1 = \begin{cases} Ae^{\sqrt{\mu_+}x} + Ce^{\sqrt{\mu_-}x} & x < 0 \\ Ae^{-\sqrt{\mu_+}x} + Ce^{-\sqrt{\mu_-}x} & x > 0 \end{cases} \tag{4.11}$$

$$\phi_2 = \begin{cases} Ae^{\sqrt{\mu_+}x} - Ce^{\sqrt{\mu_-}x} & x < 0 \\ Ae^{-\sqrt{\mu_+}x} - Ce^{-\sqrt{\mu_-}x} & x > 0 \end{cases} \tag{4.12}$$

Our next step is to introduce continuity conditions. This form of the solutions automatically satisfies continuity condition at $x = 0$. Jump of derivative is estimated by integrating equations 4.9 around $x = 0$, which gives $\partial_x \phi_m|_{x=0} = -2\phi^3_{x=0}$. This condition for derivatives leads to the following set of equations.

$$\begin{cases} \sqrt{\mu_+}A + \sqrt{\mu_-}C = (A + C)^3 \\ \sqrt{\mu_+}A - \sqrt{\mu_-}C = (A - C)^3 \end{cases} \tag{4.13}$$

This set of equations has three distinct solutions. Symmetric and antisymmetric states can be easily found by assuming $C = 0$ and $A = 0$ respectively

$$A^2_{sym} = \sqrt{\mu_+/2}, \qquad N_{sym} = 2, \qquad E_{sym} = -\kappa \tag{4.14}$$

$$C^2_{anti} = \sqrt{\mu_-/2}, \qquad N_{anti} = 2, \qquad E_{anti} = \kappa \tag{4.15}$$

The third solution leads to the family of asymmetric states

$$A = \pm\frac{1}{2}\sqrt{\frac{3}{2}\sqrt{\mu_-} - \frac{1}{2}\sqrt{\mu_+}} \tag{4.16}$$

$$C = \pm\frac{1}{2}\sqrt{\frac{3}{2}\sqrt{\mu_+} - \frac{1}{2}\sqrt{\mu_-}} \tag{4.17}$$

with the following norm and energy

$$N_{asym} = \frac{-3\mu - \sqrt{\mu^2 - \kappa^2}}{2\sqrt{\mu^2 - \kappa^2}} \tag{4.18}$$

$$E_{asym} = -\frac{3}{8}\kappa\left[\sqrt{\frac{\mu_-}{\mu_+}} - \sqrt{\frac{\mu_+}{\mu_-}}\right] \tag{4.19}$$

Asymmetric states exist only if $C > 0$ in equation 4.16, which leads to the following bifurcation condition

$$\mu < \frac{-5}{4}\kappa \tag{4.20}$$

To measure state asymmetry, we introduce channel asymmetry coefficient Θ_c.

$$\Theta_c = \frac{\int_{-\infty}^{\infty} |\phi_1|^2 - |\phi_2|^2 dx}{\int_{-\infty}^{\infty} |\phi_1|^2 + |\phi_2|^2 dx} \tag{4.21}$$

We find channel asymmetry coefficient for single-delta asymmetric states by substituting 4.16 into 4.21

$$\Theta_c = \frac{4\sqrt{5\sqrt{\mu^2 - \kappa^2} + 3\mu} \cdot \sqrt{\mu^2 - \kappa^2}}{\left(-3\mu - \sqrt{\mu^2 - \kappa^2}\right)\left(\sqrt{-2(\mu + \kappa)} + \sqrt{-2(\mu - \kappa)}\right)} \tag{4.22}$$

All results presented in this section are summed up in Figure (4.2). Channel asymmetry coefficient figure shows that transition to asymmetric states is subcritical – $\Theta_c(\mu)$ is a continuous function.

Numerical stability analysis shows that asymmetric states found in this configuration are always unstable for Delta functions. In the case of wider Gaussian nonlinear potentials, stable asymmetric states are observed. This fact shows that model with Dirac Delta functions can be used to explore general soliton states, but it doesn't provide good predictions of the soliton dynamics.

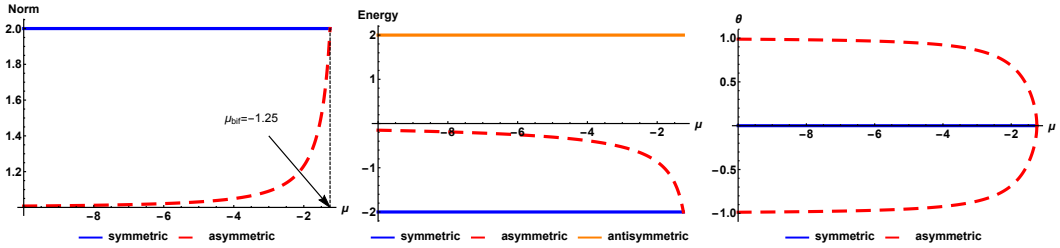

FIGURE 4.2: Norm (left), energy (center) and asymmetry coefficients (right) for the stationary states in one-delta system for $\kappa = 1$. Dashed lines represent unstable states. After Ref. [165].

4.3 Double-delta waveguides

Our next step is to introduce double nonlinear inclusions in $x = \pm 1$ for each channel.

$$\begin{cases} i\partial_z\psi_1 + \frac{1}{2}\partial_{xx}\psi_1 + [\delta(x-1) + \delta(x+1)]\,|\psi_1|^2\psi_1 + \kappa\psi_2 = 0 \\ i\partial_z\psi_2 + \frac{1}{2}\partial_{xx}\psi_2 + [\delta(x-1) + \delta(x+1)]\,|\psi_2|^2\psi_2 + \kappa\psi_1 = 0 \end{cases} \tag{4.23}$$

The general algorithm used to find soliton states remains the same. However, the introduction of the second impurity leads to the possibility of the second symmetry breaking type – spatial symmetry breaking. This process will be measured by the spatial asymmetry coefficient.

$$\Theta_s = \frac{\int_0^\infty |\phi_1|^2 + |\phi_2|^2 dx - \int_{-\infty}^0 |\phi_1|^2 + |\phi_2|^2 dx}{\int_{-\infty}^\infty |\phi_1|^2 + |\phi_2|^2 dx} \tag{4.24}$$

Double-impurity soliton states take the following form

$$\phi_1 = \begin{cases} Be^{\sqrt{\mu_+}(1+x)} + De^{\sqrt{\mu_-}(1+x)} & x < -1 \\ B_0e^{\sqrt{\mu_+}(1+x)} + D_0e^{\sqrt{\mu_-}(1+x)} + A_0e^{\sqrt{\mu_+}(1-x)} + C_0e^{\sqrt{\mu_-}(1-x)} & -1 < x < 1 \\ Ae^{\sqrt{\mu_+}(1-x)} + Ce^{\sqrt{\mu_-}(1-x)} & x > 1 \end{cases} \tag{4.25}$$

$$\phi_2 = \begin{cases} Be^{\sqrt{\mu_+}(1+x)} - De^{\sqrt{\mu_-}(1+x)} & x < -1 \\ B_0e^{\sqrt{\mu_+}(1+x)} - D_0e^{\sqrt{\mu_-}(1+x)} + A_0e^{\sqrt{\mu_+}(1-x)} - C_0e^{\sqrt{\mu_-}(1-x)} & -1 < x < 1 \\ Ae^{\sqrt{\mu_+}(1-x)} - Ce^{\sqrt{\mu_-}(1-x)} & x > 1 \end{cases} \tag{4.26}$$

Continuity of the wavefunctions at $x = \pm 1$ leads to the following substitutions.

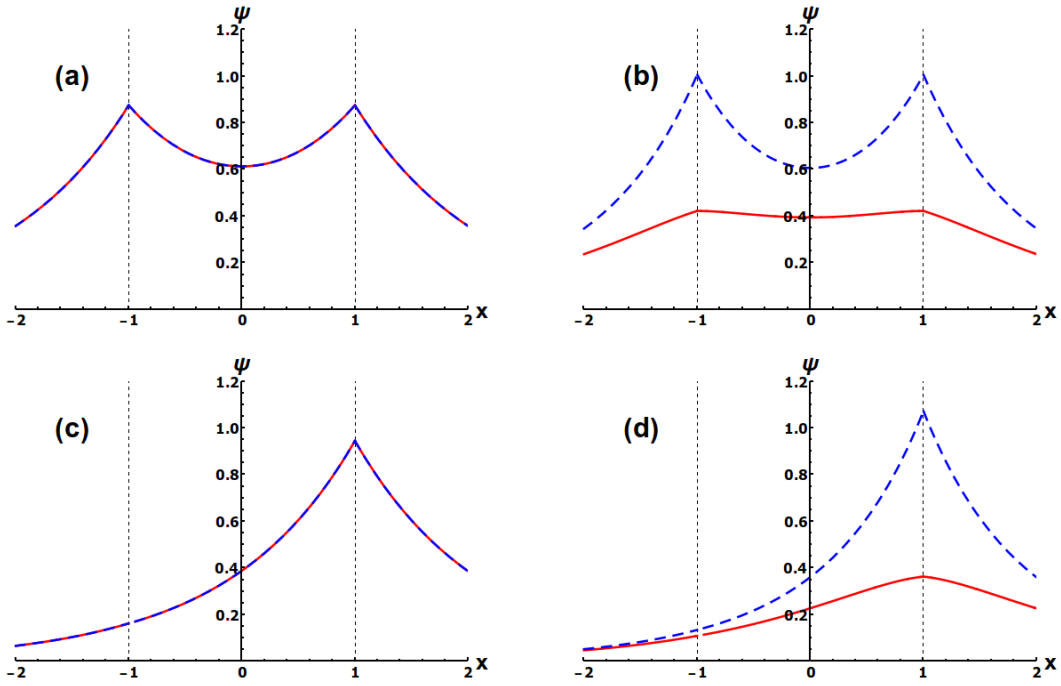

FIGURE 4.3: Examples of states with different symmetry properties. (a) – fully symmetric state; (b) – "inter-symmetric" state; (c) – "intra-symmetric" state; (d) – fully asymmetric state. After Ref. [165].

$$A_0 = \frac{e^{2\sqrt{\mu_+}}B - A}{e^{4\sqrt{\mu_+}} - 1}, B_0 = \frac{e^{2\sqrt{\mu_+}}A - B}{e^{4\sqrt{\mu_+}} - 1}, C_0 = \frac{e^{2\sqrt{\mu_-}}D - C}{e^{4\sqrt{\mu_-}} - 1}, D_0 = \frac{e^{2\sqrt{\mu_-}}C - D}{e^{4\sqrt{\mu_-}} - 1} \quad (4.27)$$

The condition for derivatives continuity leads to the following set of equations.

$$\begin{cases} \sqrt{\mu_+}e^{2\sqrt{\mu_+}}\left(e^{2\sqrt{\mu_+}}B - A\right) = \left(e^{4\sqrt{\mu_+}} - 1\right)B(B^2 + 3D^2) \\ \sqrt{\mu_+}e^{2\sqrt{\mu_+}}\left(e^{2\sqrt{\mu_+}}A - B\right) = \left(e^{4\sqrt{\mu_+}} - 1\right)A(A^2 + 3C^2) \\ \sqrt{\mu_-}e^{2\sqrt{\mu_-}}\left(e^{2\sqrt{\mu_-}}C - D\right) = \left(e^{4\sqrt{\mu_-}} - 1\right)C(C^2 + 3A^2) \\ \sqrt{\mu_-}e^{2\sqrt{\mu_-}}\left(e^{2\sqrt{\mu_-}}D - C\right) = \left(e^{4\sqrt{\mu_-}} - 1\right)D(D^2 + 3B^2) \end{cases} \quad (4.28)$$

This system of equations has 81 solutions in general, with 20 unique non-trivial solutions. Some of the resulting states are presented in Figure (4.3). This system of equations cannot be solved analytically, however, the solutions can be simply calculated with numerical methods. For example, states with two simultaneously broken symmetries can be found only numerically. States with certain symmetries can be found analytically.

We observe two different types of symmetry breaking, separately or simultaneously. First, we can calculate a fully symmetrical state (A=B, C=D=0).

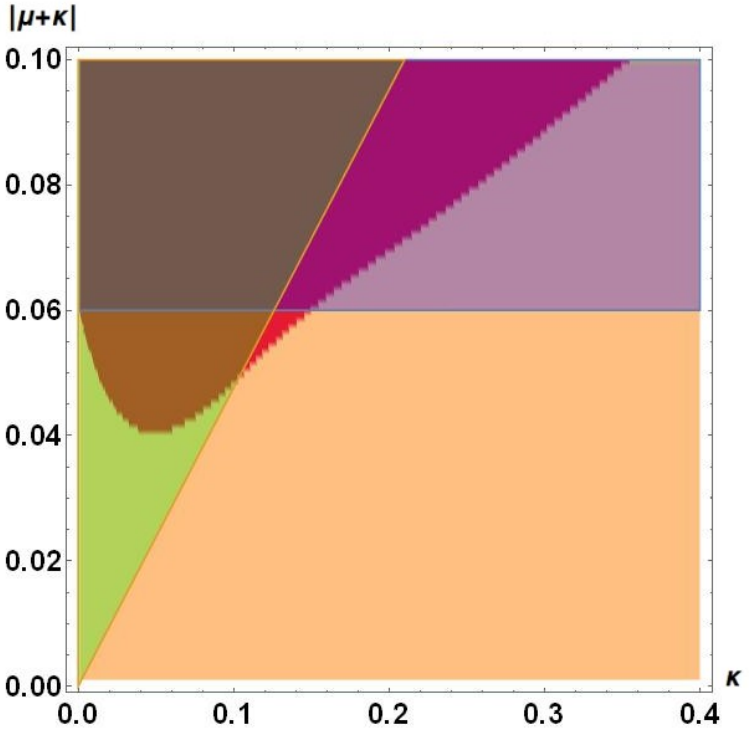

FIGURE 4.4: Map of solution types for different values of κ and μ_+. Fully asymmetric states are found numerically in the red region, while fully symmetric states exist in both red and peach areas. Additional color filters represent areas with present intra-symmetric states (blue region defined by the equation 4.31) and inter-symmetric states (green region defined by the equation 4.33). After Ref. [165].

$$A = B = \sqrt{\frac{\sqrt{\mu_+}}{1+e^{-2\sqrt{\mu_+}}}} \tag{4.29}$$

Symmetry breaking in space with maintaining symmetry between channels (C=D=0) creates "intra-symmetric" states.

$$A = \frac{\sqrt[4]{\mu_+}\left(\sqrt{1+2e^{-2\sqrt{\mu_+}}}+\sqrt{1-2e^{-2\sqrt{\mu_+}}}\right)}{2\sqrt{1-e^{-4\sqrt{\mu_+}}}}$$
$$B = \frac{\sqrt[4]{\mu_+}\left(\sqrt{1+2e^{-2\sqrt{\mu_+}}}-\sqrt{1-2e^{-2\sqrt{\mu_+}}}\right)}{2\sqrt{1-e^{-4\sqrt{\mu_+}}}} \tag{4.30}$$

Such "intra-symmetric" states break spatial symmetry below the bifurcation line.

$$\mu_+ = \left(\frac{\log 2}{2}\right)^2 \tag{4.31}$$

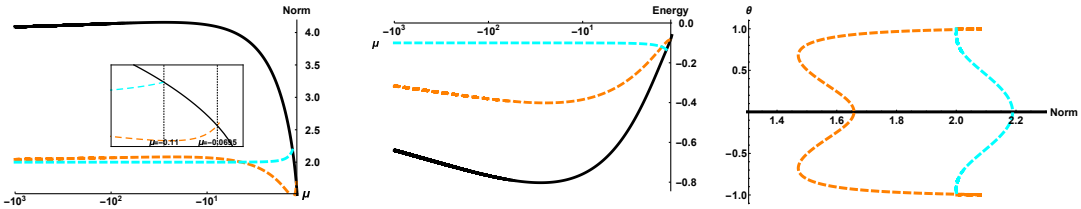

FIGURE 4.5: Norm (left), energy (center) and asymmetry coefficients (right) for the stationary states in two-delta system for $\kappa = 0.05$. Black curves represent fully symmetric states, orange curves – "inter-symmetric" states, cyan curves – "intra-symmetric" states. Inset in subfigure (a) zooms on bifurcation points for both asymmetry states. Orange and cyan curve in subfigure (c) represent Θ_c and Θ_s respectively. After Ref. [165].

Breaking symmetry between channels and maintaining spatial symmetry (A=B, C=D) leads to "inter-symmetric" states.

$$A = B = \frac{3\sqrt{\mu_-}\left(1+e^{-2\sqrt{\mu_+}}\right) - \sqrt{\mu_+}\left(1+e^{-2\sqrt{\mu_-}}\right)}{8\left(1+e^{-2\sqrt{\mu_+}}\right)\left(1+e^{-2\sqrt{\mu_-}}\right)}$$
$$C = D = \frac{3\sqrt{\mu_+}\left(1+e^{-2\sqrt{\mu_-}}\right) - \sqrt{\mu_-}\left(1+e^{-2\sqrt{\mu_+}}\right)}{8\left(1+e^{-2\sqrt{\mu_+}}\right)\left(1+e^{-2\sqrt{\mu_-}}\right)} \tag{4.32}$$

These "inter-symmetric" states exist below the following bifurcation curve.

$$3\sqrt{\frac{\mu_+}{\mu_-}} = \frac{e^{2\mu_+}+1}{e^{2\mu_-}+1} \tag{4.33}$$

A general map of symmetry breaking types is presented in Figure (4.4). Multiple types of symmetry breakings appear for large phase velocities. States with both broken symmetries always appear before both types of single symmetry breakings occur. It is even possible to observe a small region around $\kappa \simeq 0.13$, where both symmetries are broken simultaneously before any single process occurs.

Norm, energy, and asymmetry coefficients can be calculated analytically for fully and partially symmetric states. Resulting curves for $\kappa = 0.05$ and $\kappa = 0.2$ are presented in Figures (4.5) and (4.6) respectively. A fully symmetric state remains both the lowest energy state and the only stable state in both cases. Bifurcation of channel symmetry breaking (cyan curve) remains subcritical for every value of κ, similar to the single-delta result. On the other side, spatial symmetry breaking becomes supercritical – Θ_s is no more a function of N, as it allows for multiple unstable states. This result depends on the exact shape of the nonlinearity distribution, as this kind of bifurcation is supercritical for Gaussian nonlinearity [176] and is never subcritical for double-well structure [177].

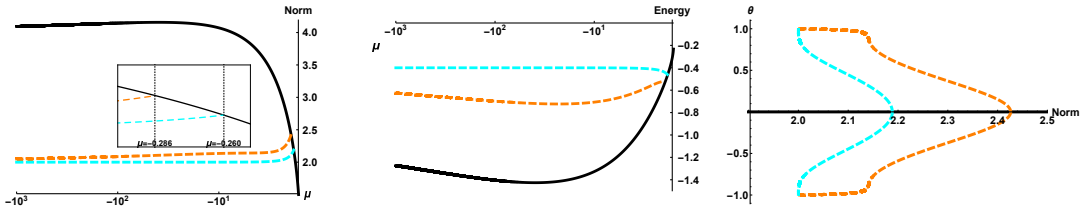

FIGURE 4.6: Norm (left), energy (center) and asymmetry coefficients (right) for the stationary states in two-delta system for $\kappa = 0.2$. Black curves represent fully symmetric states, orange curves – "inter-symmetric" states, cyan curves – "intra-symmetric" states. Inset in subfigure (a) zooms on bifurcation points for both asymmetry states. Orange and cyan curve in subfigure (c) represent Θ_c and Θ_s respectively. After Ref. [165].

4.4 Two-dimensional waveguide model

As mentioned in the previous section, all types of asymmetric states are linearly unstable. This result is known to be dependent on nonlinear distribution shape, especially for highly degenerate distributions of Dirac Delta. The main goal of our numerical calculations is to check whether stable asymmetric states exist in the two-dimensional double inclusion configuration.

$$i\frac{\partial\psi}{\partial t} = -\frac{1}{2}\left(\frac{\partial^2\psi}{\partial x^2} + \frac{\partial^2\psi}{\partial y^2}\right) + g\,(x,y)\,|\psi|^2\psi + U(x)\psi, \tag{4.34}$$

The schematic of this two-dimensional system is presented in Figure (4.7). In the case of the big coupling strength, corresponding to the small distance between waveguides, the assumption of variables separability is no longer fulfilled and CMT is not applicable [178]. The introduction of the second dimension instead of the coupled equation allows us to confirm CMT assumptions. Formulation of the model as double-well potential was used to compare our results to the present models of the atomic BEC [179].

Soliton states were calculated using ITEM, and their stability was confirmed by SSFM propagation. Resulting states are shown in Figure (4.8). The main numerical result of these simulations is the existence of stable solitons with every type of possible symmetry breaking. Additionally, we've found that symmetry breaking is observed even in the case of the small gap between waveguides. Solitons maintain their shape even after the addition of two-dimensional random amplitude noise up to 5% of the maximum soliton amplitude.

In conclusion, we've explored a double-waveguide coupled system with single and double nonlinear inclusions. Our results show large variability in possible types of symmetry breaking, including double symmetry breaking. It is also important to note that linear stability analysis may give non-applicable results for integrable

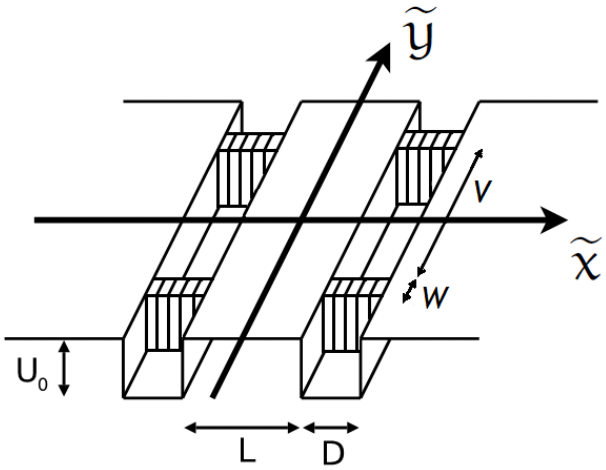

FIGURE 4.7: Schematic representation of two potential wells with double nonlinear inclusions. After Ref. [165].

models, and thus an exploration of soliton dynamics must always be confirmed by the numerical simulations.

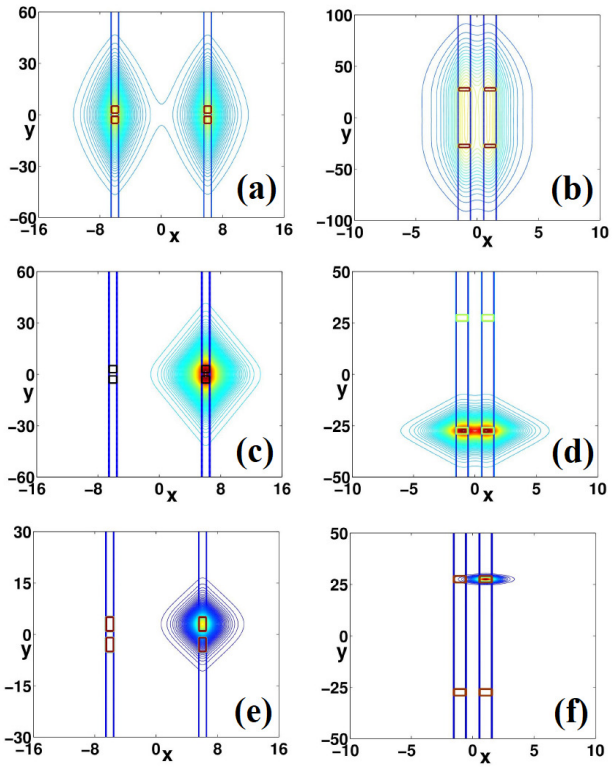

FIGURE 4.8: Contour plots of wavefunction distribution of the stable two-dimensional solitons. Panels present fully symmetric states (a-b), states with single symmetry breaking (c-d) and states with double symmetry breaking (e-f). Parameters for the (a,c,e) simulations – $L = 11, D = 1, W = 4, V = 2$ and $N = 0.6(a), N = 1.5(c), N = 2.5(e)$. Parameters for the (b,d,f) simulations – $L = 1, D = 1, W = 3, V = 52$ and $N = 1(b), N = 4(d), N = 5.1(f)$. After Ref. [165].

Chapter 5

Gain and loss in coupled nonlinear systems

Losses are omnipresent in every field of physical sciences. Attenuation is the main limiting factor in signal transmission. Solitons can be observed in dissipative media [180, 181, 182], but they still have limited lifetime. There are multiple ways to counteract this effect – one of them is continuous pumping of energy.

In this chapter I would like to focus on one example of a physical system with continuous pumping - Exciton-Polariton Condensate (EPC) [52]. The biggest difference of EPC from other types of condensates is its non-equilibrium nature.

5.1 Exciton polariton condensates

EPC is created inside semiconductor quantum wells, such as presented in Figure (5.1.a). Light is trapped inside the cavity by two Bragg mirrors. Inside quantum well, light serves two purposes. First, pumping creates excitons – electron-hole pairs – in semiconductor materials. Second, light strongly couples with excitons, creating exciton-polaritons. These polaritons emit energy through phonons, as presented in Figure (5.1.b), and condensate in a fundamental state. The lifespan of exciton-polaritons rarely exceeds several nanoseconds due to photons escaping from the cavity. Because of this, EPC requires constant light flow to support condensated state.

EPC is described by the combination of the mean-field equation for polariton wavefunction and population equation for exciton reservoir [183].

$$i\partial_t\psi = -\nabla^2\psi + 2g_c|\psi|^2\psi + g_r n_r^0\psi + U(\vec{r})\psi + i\left(Rn_r^0 - \gamma_c\right)\psi \tag{5.1}$$

where $n_r^0 = \dfrac{P}{\gamma_R + R|\psi|^2}$ is exciton reservoir density. Exciton reservoir remains saturable near equilibrium intensity $I_s = |\psi_s|^2 = 1/R$. We can transform combination of saturable gain and linear dissipation into linear gain and nonlinear loss system by expanding formula for low intensities

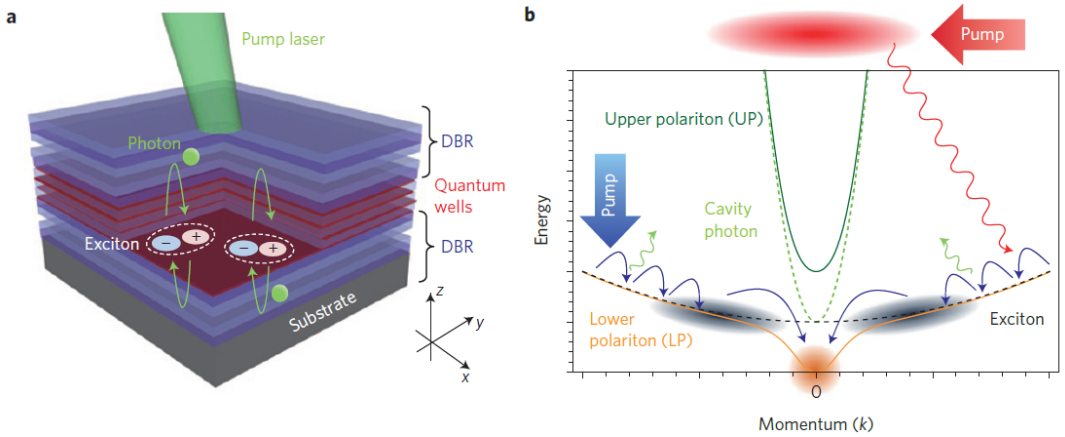

FIGURE 5.1: Fundamentals of exciton-polariton condensation. (a) – structure of quantum well used for polariton excitation. (b) – scheme of exciton-polariton pumping and condensation. After Ref. [52].

$$\partial_t I = \frac{PR}{\gamma_R + RI} - \gamma_c \simeq (\frac{PR}{\gamma_R} - \gamma_c) - \frac{PR^2}{\gamma_R^2} I \equiv \gamma - \Gamma I \tag{5.2}$$

This formula is similar to the description of laser pumping with nonlinear absorber [184]. Even though this model does not conserve norm at every point locally, its total intensity is expected to remain close to equilibrium point $I = \gamma/\Gamma$.

By default, EPC is generated in two-dimensional quantum wells. The dimensionality of EPC is further regulated by inducing ring geometry. This can be done by limiting geometry to the closed loop and observing whispering gallery modes[185, 186], or by observing vortices generated by structured pumping light [187, 188]. An example of ring-shaped EPC is presented in Figure (5.2).

EPC can be separated into two components in a magnetic field due to the intrinsic spin structure of excitons [189]. Linear coupling between components is induced through the Feshbach resonance mechanism [190, 191]. Feshbach's resonance is controlled with the additional optical beam. Change of beam structure allows controlling coupling distribution.

Our main goal is to model coupled ring structures in EPC. However, resulting equations can also be applied in other physical systems, such as plasmonic resonators [192]. Pumping can be introduced into plasmonic waveguides through active optical material [193]. Typically, nonlinear effects accompanying optical resonators are self-focusing; however, it is possible to create solitons in media with defocusing nonlinearity [194]. We have proposed a microresonator system, based on two-layered microresonators, in [195]. The general design of such a system is presented in Figure (5.3).

Coupled ring resonators with gain and loss are described by the following equations

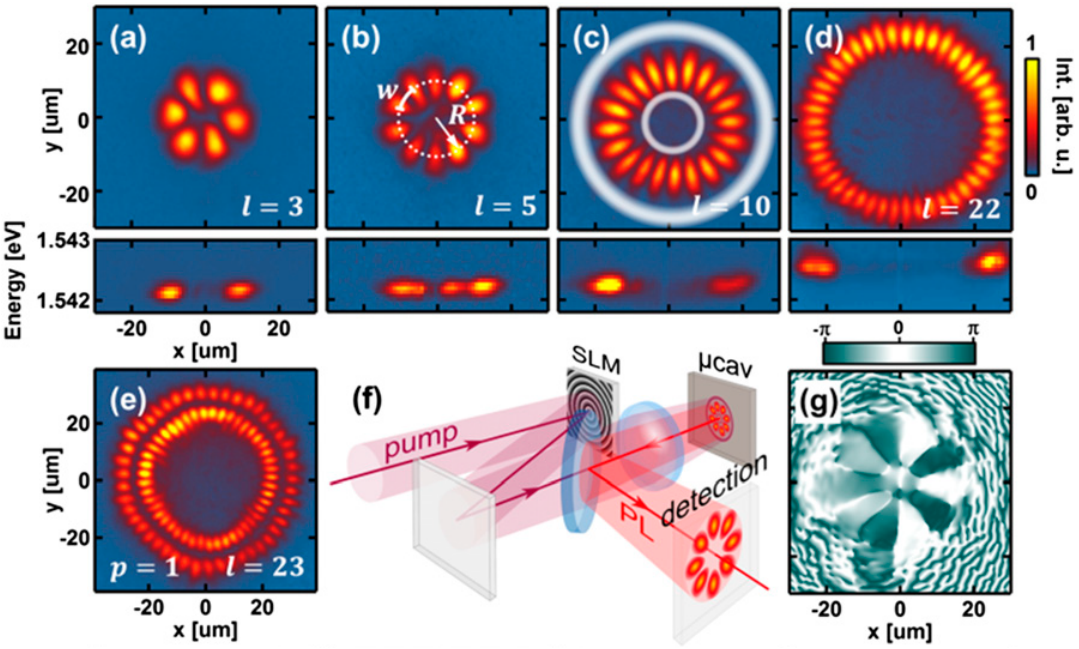

FIGURE 5.2: Experimental observation of exciton-polariton ring condensates. (a-d) – single-ring condensate. (e) – double-ring condensate. (f) – schematic of ring condensate observation device. (g) – phase portrait of the condensate in example (b). After Ref. [188].

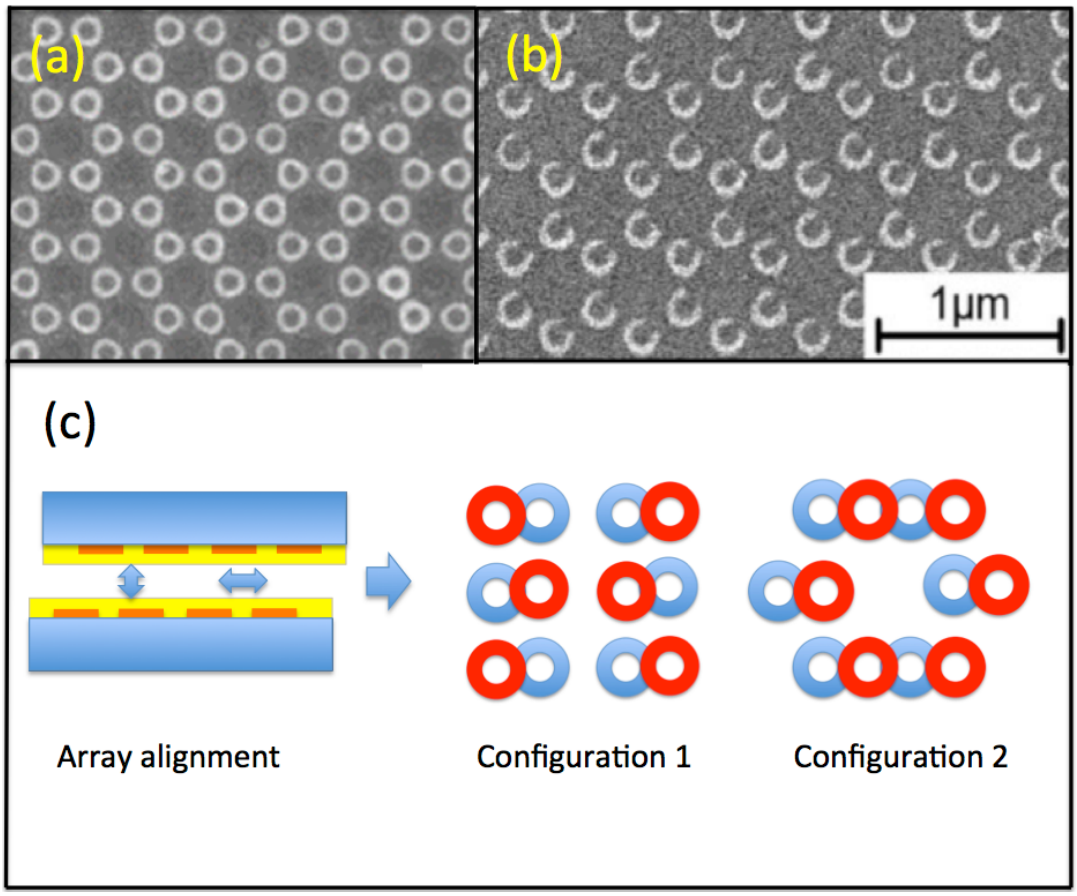

FIGURE 5.3: (a-b) – examples of fabricated microresonator array. (c) – possible configurations of microresonators with inhomogeneous coupling. After Ref. [195].

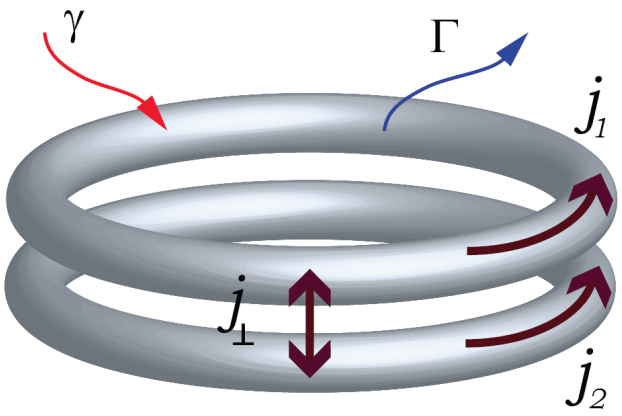

FIGURE 5.4: Schematic of double-ring structure described by Equations 5.3. After Ref. [196].

$$\begin{cases} i\partial_t\psi_1 = -\partial_{xx}\psi_1 + i\gamma\psi_1 + (1 - i\Gamma)\,|\psi_1|^2\psi_1 + c\psi_2 \\ i\partial_t\psi_2 = -\partial_{xx}\psi_2 + i\gamma\psi_2 + (1 - i\Gamma)\,|\psi_2|^2\psi_2 + c\psi_1 \end{cases} \tag{5.3}$$

Spatial coordinates were rescaled so that $x \in [0, 2\pi)$. By definition, this system has periodic boundary conditions. Note that in terms of both conservation laws and spectral numerical methods loops are even easier to work with, as any soliton becomes localized by default. Currents inside and between channels are defined as $J = \int_0^{2\pi} j dx$, where

$$j_m = \frac{\psi_m^*\partial_x\psi_m - \psi_m\partial_x\psi_m^*}{2i}\ ,\ j_\perp = \frac{c}{2i}\left(\psi_1^*\psi_2 - \psi_1\psi_2^*\right) \tag{5.4}$$

I will explore two cases in separate sections. Section 5.2 explores homogeneous coupling $c = \text{const}$, based on [196] and [197]. Section 5.3 is based on [195] and explores inhomogeneous coupling with Gaussian distribution $c \sim e^{-x^2/w^2}$.

5.2 Homogeneous coupling

We are looking for fundamental solutions in the following form.

$$\psi_m = \rho_m e^{i\kappa x - i\mu t \pm i\theta} \tag{5.5}$$

Here κ is an integer number representing angular velocity; μ is propagation constant or, in the context of BEC, chemical potential; and 2θ is the relative phase between channels. In the context of whispering gallery modes, κ can be treated as vorticity or topological charge. This approach is similar to vortex states analysis of structured light [198].

We can easily find solution for decoupled rings ($c = 0$): $\rho = \sqrt{\gamma/\Gamma}, \mu = \gamma/\Gamma + \kappa^2$. If rings are coupled, we substitute 5.5 into 5.3 and get following equation

$$\left(\rho_1^2 - \rho_2^2\right)\left(\mu - \kappa^2 - \rho_1^2 - \rho_2^2\right) = 0 \tag{5.6}$$

This equation in general gives us 4 solutions. Two of them are symmetric and antisymmetric states respectively:

$$\rho_{sym} = \sqrt{\frac{\gamma}{\Gamma}}, \qquad \mu_{sym} = \frac{\gamma}{\Gamma} + \kappa^2 + c, \qquad \theta_{sym} = 0 \tag{5.7}$$

$$\rho_{anti} = \sqrt{\frac{\gamma}{\Gamma}}, \qquad \mu_{anti} = \frac{\gamma}{\Gamma} + \kappa^2 - c, \qquad \theta_{anti} = \pi/2 \tag{5.8}$$

Additionally, we found two branches of asymmetric solutions.

$$\tilde{\mu}_\pm = \frac{3\Gamma^2 - 1 \pm \sqrt{\left(\Gamma^2+1\right)^2 - 8\tilde{c}^2\Gamma^2\left(\Gamma^2-1\right)}}{2\Gamma\left(\Gamma^2-1\right)}$$

$$\rho_{1,\pm} = \frac{\gamma}{2}\left(\tilde{\mu}_\pm - \sqrt{\frac{2\tilde{\mu}_\pm}{\Gamma} - \tilde{\mu}_\pm^2}\right)$$

$$\rho_{2,\pm} = \frac{\gamma}{2}\left(\tilde{\mu}_\pm + \sqrt{\frac{2\tilde{\mu}_\pm}{\Gamma} - \tilde{\mu}_\pm^2}\right)$$

$$\cos^2(2\theta_\pm) = \frac{\tilde{\mu}_\pm}{2\tilde{c}}\left(\tilde{\mu}_\pm - \frac{1}{\Gamma}\right) \tag{5.9}$$

where following normalizations were applied: $\tilde{c} = \frac{c}{\gamma}, \tilde{\mu} = \frac{\mu - \kappa^2}{\gamma}$. Normalized chemical potentials can also simplify formulas for symmetric and antisymmetric states: $\tilde{\mu}_{sym,anti} = \frac{1}{\Gamma} \pm \tilde{c}$.

Several conditions define regions of asymmetric modes' existence. Amplitudes and phase mismatches must be real. This fact restricts chemical potential

$$\frac{1}{\Gamma} \le \tilde{\mu}_\pm \le \frac{2}{\Gamma} \tag{5.10}$$

$\tilde{\mu}_\pm$ must be real, which gives condition for critical losses

$$\Gamma < \Gamma_{crit} = \frac{1}{\sqrt{4\tilde{c}\left(\sqrt{\tilde{c}^2+1} - 1\right) - 1}} \tag{5.11}$$

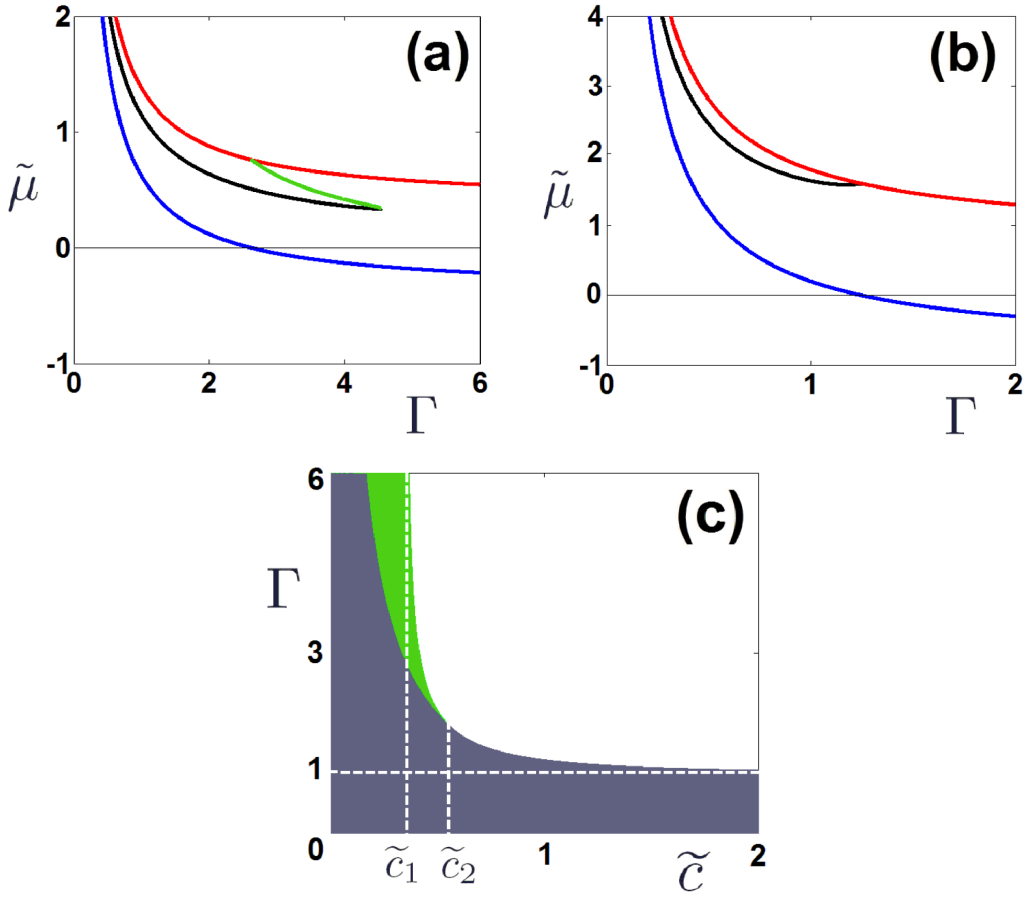

FIGURE 5.5: Asymmetric branches domains. (a-b) – Branches of stationary solutions for $\tilde{c} = 0.38 < \tilde{c}_2$ (a) and $\tilde{c} = 0.8 > \tilde{c}_2$ (b). Red and blue curves represent symmetric and antisymmetric solutions, green and black curves represent asymmetric solutions μ_+ and μ_-. (c) – domains of existence for asymmetric states. Both asymmetric states exist inside green area, but only $\tilde{\mu}_-$ solutions exist in gray area. Upper border of both areas is defined by Γ_{crit}, lower bound of green area is described by Γ_{bif}. After Ref. [196].

Asymmetric states can be achieved for sufficiently small coupling, as condition 5.11 is always fulfilled for $\tilde{c} < \tilde{c}_1 = \frac{1}{\sqrt{8}}$. On the other side, one of the asymmetric solutions μ_+ merges with symmetric branch at bifurcation curve $\Gamma_{bif} = \frac{1}{\tilde{c}}$. Comparing Γ_{bif} and Γ_{crit} leads to upper limit on μ_+ state existence – $\tilde{c} < \tilde{c}_2 = \frac{1}{\sqrt{3}}$. Second asymmetric solution μ_- does not have similar limitations. Parametric curves and conditions presented above are shown in Figure (5.5).

Current densities in symmetric and antisymmetric states are trivial – current between channels is absent, while current in each ring is constant and equal to topological charge κ. Wavefunction momenta for asymmetric states remain the same, however, we observe non-zero transverse current.

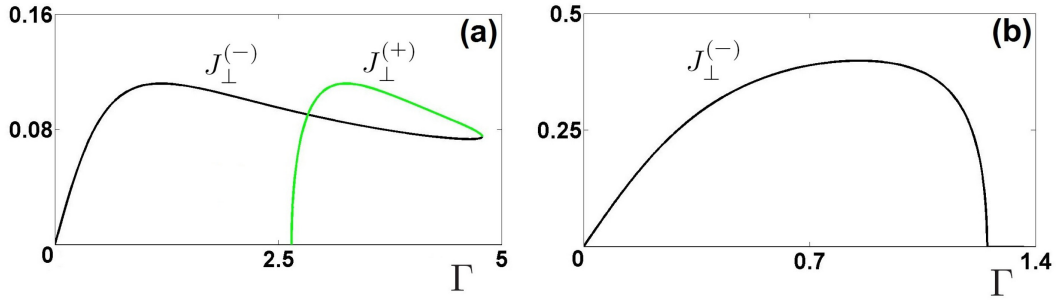

FIGURE 5.6: Transverse currents in asymmetric states for $\tilde{c} = 0.38 < \tilde{c}_2$ (a) and $\tilde{c} = 0.8 > \tilde{c}_2$ (b). After Ref. [196].

$$|J_{\perp,\pm}| = \pi\gamma^2\sqrt{\tau_\pm\left(2\tilde{c}^2 - \tau_\pm\right)} \tag{5.12}$$

where $\tau_\pm = \tilde{\mu}_\pm^2 - \dfrac{\tilde{\mu}_\pm}{\Gamma}$. In asymmetric states we observe spontaneous symmetry breaking – both rings are identical, thus both current directions are equally valid. Examples of intra-channel currents are presented in Figure (5.6).

5.2.1 Stability analysis

The next step in soliton exploration is stability analysis. As we've found analytic formulas for wavefunctions, we can use a linear stability analysis framework. We follow the procedure from Chapter 2, starting with the definition of perturbed states.

$$\tilde{\psi}_m = e^{i\kappa x - i\mu t}\left[\rho_m e^{i(-1)^m\theta} + e^{\lambda t}U_m(x) + e^{\lambda^* t}V_m^*(x)\right] \tag{5.13}$$

We assume spectral form of perturbations $U, V \sim e^{ikx}$, as they represent a complete basis. Note that perturbation wavenumbers k are limited to integers due to periodic boundary conditions. After substitution of 5.13 into 5.3 and linearization with respect to $U, V \ll \rho_m$, we get following eigenproblem

$$\begin{bmatrix} \alpha_1 & \beta_1^* & -ic & 0 \\ \beta_1 & \alpha_1^* & 0 & ic \\ -ic & 0 & \alpha_2 & \beta_2^* \\ 0 & ic & \beta_2 & \alpha_2^* \end{bmatrix} \begin{bmatrix} U_1 \\ V_1 \\ U_2 \\ V_2 \end{bmatrix} = \lambda \begin{bmatrix} U_1 \\ V_1 \\ U_2 \\ V_2 \end{bmatrix} \tag{5.14}$$

where

$$\alpha_m = \gamma - 2\Gamma\rho_m^2 + i\left(\mu - (k+\kappa)^2 - 2\rho_m^2\right) \tag{5.15}$$

$$\beta_m = \rho_m^2 e^{2i(-1)^m\theta}\left(i - \Gamma\right) \tag{5.16}$$

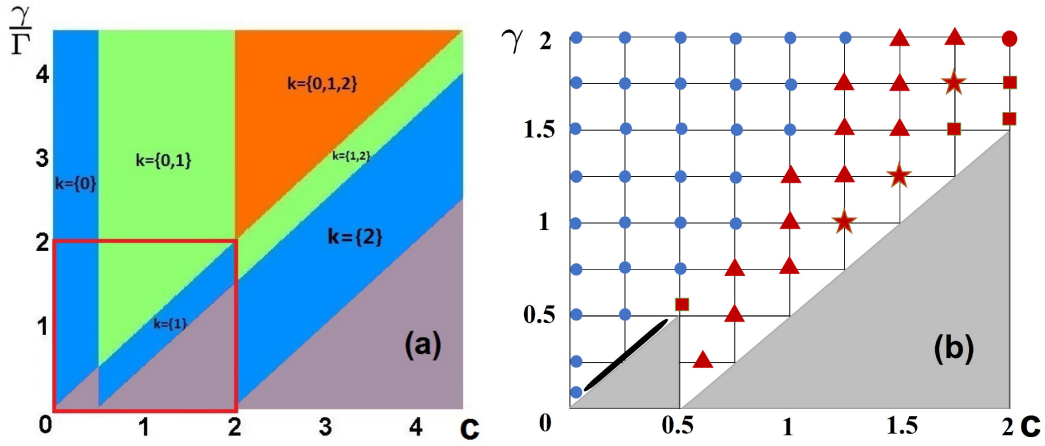

FIGURE 5.7: Stability analysis of symmetric states. (a) – instability domains. Wavenumbers of unstable modes are noted in each domain. Colours signify different amount of unstable modes, gray color denotes stable domains. Red square outlines parametric area explored numerically. (b) – states reached through propagation of perturbed symmetrical state. Gray areas correspond to stable domains. Blue dots show symmetric states evolving into antisymmetric states; red triangles – into out-of-phase vortices with $\kappa = 1$; red stars show limit cycle oscillations with homogeneous density; red squares lead to stationary inhomogeneous states; red circle at $\gamma = c = 2$ represents chaotic motion; black stripe in lower left corner shows evolution into asymmetric state. Points on left axis correspond to $c = 0.01$. All calculations were made for $\Gamma = 1$. After Ref. [196].

Stability matrix depends on vorticity only as a combination $k + \kappa$, thus states with the same amplitudes and chemical potentials have the same stability, independent from state vorticity. I will concentrate on the linear stability of states with zero vorticity.

Substitution of four possible states into 5.14 shows that antisymmetric and asymmetric states are always stable. Symmetric states are unstable in domains, where perturbation wavevector satisfies inequation $2\left(c - \frac{\gamma}{\Gamma}\right) < k^2 < 2c$. Domains of instability for symmetric states are shown in Figure (5.7.a).

The evolution of unstable states in dissipative systems typically leads to stable solutions – attractors [167]. Our next step is a simulation of symmetric state evolution using SSFM. Additional periodic perturbation around 5% of the original amplitude is introduced to stimulate modulational instability. Results of simulations are presented in Figure (5.7.b).

We observed abundant variability in soliton dynamics, which is shown in Figure (5.7.b). Our simulations confirmed theoretical stability domains. Unstable states typically evolve into antisymmetric states (blue circles). In the case of low coupling states near stability regions (black stripe) tend to evolve into asymmetric states described earlier. Other observed states include stationary inhomogeneous solutions (red squares), out-of-phase pairs of vortices with $\kappa = 1$ (red triangles), periodically

oscillating homogeneous symmetric solutions (red stars), and even chaotic motion (red circle). Types of exhibited behaviors roughly correlate with wavenumber instability domains – instability of $k = 0$ wavenumber typically signifies evolution to antisymmetric states, while $k = 1$ instability typically leads to vortex creation. More dynamic solutions appear near borders of instability domains.

5.2.2 Inhomogeneous states

Inhomogeneous states were explored deeper, as they present simultaneous spatial and intra-channel symmetry breaking. An example of such a state is presented in Figure (5.8). Inhomogeneity of state takes the form of periodic modulation. If an initial state has non-zero vorticity, inhomogeneity becomes modulated in time with the same total vorticity. The exact position of wavefunction maximum depends on initial perturbation. Inhomogeneity of final states leads to permanent current flow structure, as presented in (5.8.d).

The inhomogeneous state has a period of one ring length. This fact suggests a small number of modes involved in evolution dynamics. Fourier decomposition, presented in (5.8.b), shows dominant contribution of $k = \pm 1$ components and constant background $k = 0$. Based on these facts, we hypothesize that state evolution can be estimated through Galerkin approximation [199]. The general idea of the Galerkin methods is to represent the continuous problem as a system of coupled discrete equations. The initial state under the Galerkin approximation is represented as a sum of basis functions. We chose the Fourier basis, as it is natural for periodical geometry.

$$\psi_m(x,t) = e^{i\kappa x - i\mu t} \sum_{n=-\infty}^{\infty} B_{m,n}(t) e^{inx} \tag{5.17}$$

Numerical simulations show several symmetries present in case of inhomogeneous states. First, Galerkin coefficients in one channel define coefficient in another: $B_{1,n} = (-1)^n B_{2,n}$. Second, Fourier transform maintains symmetry around initial vorticity: $|B_{m,n}| = |B_{m,2K-n}|$, where K is the vorticity of initial state.

We've explored inhomogeneous state with no initial vorticity with the assumption that only three Galerkin terms play role in evolution. This leads to the following system of ordinary differential equations.

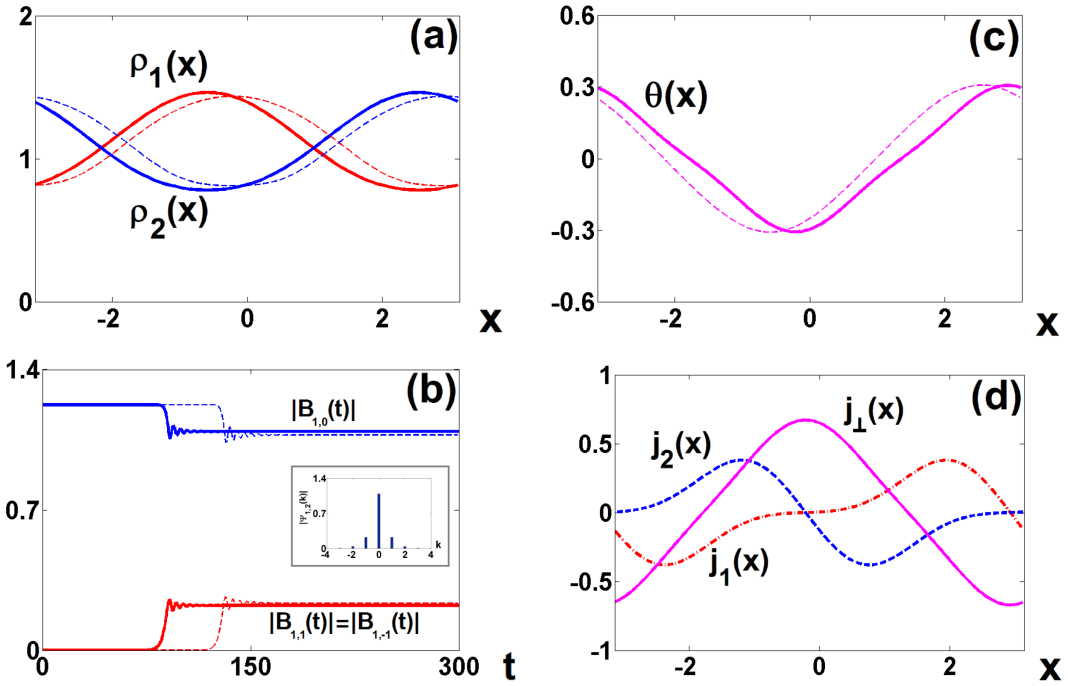

FIGURE 5.8: Inhomogeneous state, obtained for $\gamma = 1.5, \Gamma = 1, c = 1.75$. (a) – wavefunctions amplitudes. (b) – time evolution of central Fourier components. Inset present final Fourier spectrum of inhomogeneous state. (c) – relative phase θ. Figures (a-c) present full numerical simulation (solid line) and Galerkin approximation with $k = \{-1, 0, 1\}$ modes (dashed line). (d) – Intra-ring current $j_\perp$ (solid line) and inner ring currents j_m (dashed and dotted curves). After Ref. [196].

$$i\partial_t B_{1,n} = \left(i\gamma + (\kappa + n)^2 - \mu\right) B_{1,n} + cB_{2,n} + (1 - i\Gamma) \sum_{p=-1}^{1} \sum_{q=-1}^{1} B^*_{1,p+q-n} B_{1,p} B_{1,q} \tag{5.18}$$

$$i\partial_t B_{2,n} = \left(i\gamma + (\kappa + n)^2 - \mu\right) B_{2,n} + cB_{1,n} + (1 - i\Gamma) \sum_{p=-1}^{1} \sum_{q=-1}^{1} B^*_{2,p+q-n} B_{2,p} B_{2,q} \tag{5.19}$$

Results of Galerkin approximation are compared with full simulation in Figure (5.8.a-c). Galerkin approximation accurately represents the final state. The biggest discrepancy is observed in the evolution time needed to reach an inhomogeneous state. This delay appears as the initial perturbation profile involves higher modes, which are comparable in numerical simulations but neglected in Galerkin approximation.

5.2.3 Dynamic states

Another type of state that demands our attention is dynamic states - limit cycle oscillations and chaotic oscillations. Limit cycle oscillations can be distinguished from converging, diverging or chaotic oscillations through the construction of phase portraits [167]. In particular, we use multidimensional phase space consisting of total norm value in different moments of time $N(t), N(t+\Delta t), N(t+2\Delta t)$ with arbitrary delay Δt. Idea of expanding scalar function onto multidimensional space is based on Takens-Mane theorem [200, 201]. Essentially, this phase portrait visualizes predictions on future total norm value based on two previous points. Phase portraits for both limit cycle oscillations and chaotic oscillations are presented in Figure (5.9). Total norm (presented in the small frame) oscillates near $N_{eq} = 4\pi\dfrac{\gamma}{\Gamma}$ in both cases. Two dynamic regimes differ with intensity and frequency of norm jumps – both are regular for limit cycle and irregular for chaotic oscillations.

Galerkin approximation can be used to simulate limit cycle and even chaotic behavior. Results of Galerkin approximation for chaotic oscillations are presented in Figure (5.10). Full analysis of bifurcation between limit cycle and chaotic oscillations was performed by my colleagues in [197].

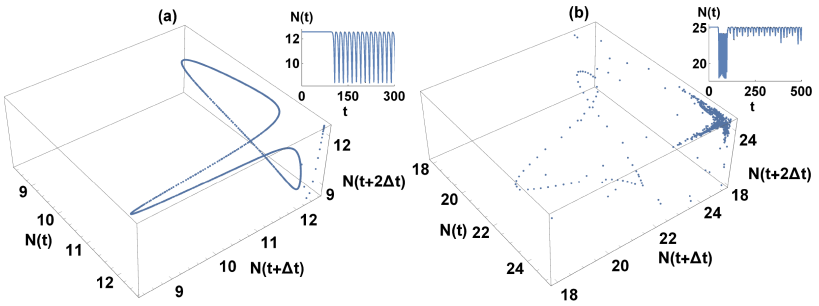

FIGURE 5.9: Phase portraits of norm oscillations. (a) – limit cycle oscillations, observed at $\Gamma = 1, \gamma = 1, c = 1.25$. (b) – chaotic oscillations at $\Gamma = 1, \gamma = 2, c = 2$. Small frames show corresponding time evolution of total norm. After Ref. [196].

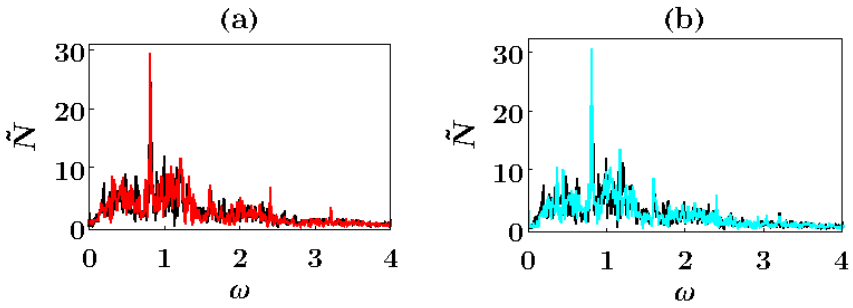

FIGURE 5.10: Comparison of norm dynamics Fourier spectra for numerical simulations (black) and Galerkin approximation using 11 modes (color). Two frames correspond to different initial perturbations. Initial parameters $\Gamma = 1, \gamma = 1.75, c = 1.81$. After Ref. [197].

5.3 Inhomogeneous coupling

Previous section scrutinized case of constant, evenly distributed coupling. In this chapter, I analyze case of linear coupling localized in finite spot. I will use local Gaussian coupling in particular:

$$c(x) = \frac{c_0}{\sqrt{\pi}w} e^{-\frac{x^2}{w^2}} \tag{5.20}$$

This coupling function is defined only by two parameters – coupling strength c_0 and width w. Similar states with identical conditions, thresholds and general shapes, were also achieved for super-Gaussian coupling shapes $c(x) \sim e^{-(x/w)^p}$ with $p \in [8, 20]$.

System of equations 5.3 with inhomogeneous coupling does not have analytic solutions. Because of this, our approach is based on the inherent instability of symmetric stationary states shown in the previous chapter. Results are obtained by the propagation of a homogeneous symmetric state with an initial small perturbation using SSFM.

$$\psi_{1,2}(t = 0) = \sqrt{\frac{\gamma}{\Gamma}}(1 + \beta \sin[kx]) \tag{5.21}$$

Symmetric initial states show different possible attractors. Evolution results do not depend on perturbation strength or wavenumber. All results remain qualitatively similar for different values of γ and Γ, as long as $\gamma \geq \Gamma$. Case of losses dominating over gain $\gamma < \Gamma$ are not presented. All results exhibited below assume $\gamma = 3, \Gamma = 1$, unless stated otherwise.

Simulations show that antisymmetric states always converge to stationary antisymmetric states, similarly to the constant coupling case. Antisymmetric states can also be achieved from initial symmetric states if the initial coupling is relatively weak ($c_0 \leq 1$). Examples of antisymmetric states are presented in Figure (5.11).

The general shape of the stationary state can be understood by considering the coupling term as a perturbation of the initial uncoupled state. In antisymmetric case, coupling term $c(x)\psi_{3-m} = -c(x)\psi_m$ serves as a potential well, increasing wavefunction presence inside coupled region. Average wavefunction level remains close to the expected value for uncoupled case $\rho(c = 0) = \sqrt{\frac{\gamma}{\Gamma}}$. Another interesting property of antisymmetric states is the appearance of two minima in points, different from $x = \pm\pi$, for strong or narrow coupling. This effect appears as a point furthest from coupling influence competes to maintain value close to $\frac{\gamma}{\Gamma}$, as if it was unperturbed.

At this point, three coupling regimes can be considered. Wide coupling $w \gg \pi$ converges to homogeneous coupling, discussed in the previous chapter. Simulations

show that narrow coupling $w \ll 1$ allows for asymmetric stationary states, meanwhile, both narrow and intermediate coupling range $w \simeq 1$ lead to limit cycle oscillating states in presence of sufficiently strong coupling.

5.3.1 Narrow coupling

Asymmetric stationary states, recovered from narrow coupling simulations, are presented in Figure (5.12). Constant phase oscillation term is removed through by assuming first channel phase $\phi_1(x = \pm\pi) = 0$. Symmetry breaking appears in the narrow window for $c_0 \simeq 1.5$. One of the channels maintains a single minimum at $x = \pm\pi$, while the second channel develops two minima, similarly to the antisymmetric case described above. Furthermore, we observe unusual current distribution near the coupling region. We observe local minimum in relative phase distribution ϕ_1 of the more populated channel at $x = 0$, while the less populated channel maintains local phase maximum at the same point. This means that current in a more populated ring flows outwards from the center, while current in a less populated channel flows towards the coupling region. Even more interesting is the fact that $j_\perp(x = 0) > 0$, thus intra-channel current flows from less populated channel to more populated channel. This behavior can be explained through the nonlinear absorption term – high-intensity peak in the first channel serves as a faster sink than a similar structure in the second channel.

An increase of coupling strength in narrow coupling case leads to limit cycle oscillations. Similar oscillations are observed for broader coupling.

5.3.2 Broad coupling

Pseudocolor plots and norm evolution curves, representing limit cycle oscillations for $w = 1$, are presented in Figure (5.13). The case of broad coupling simulations shows evolution into stationary antisymmetric states for $c_0 \lesssim 3.5$, similarly to the narrow coupling case. Stationary asymmetric states were not observed for broader coupling – instead, symmetrical oscillations appear. Both oscillations frequency and

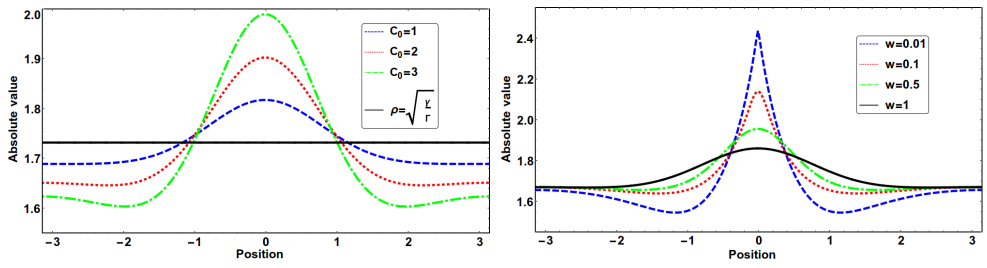

FIGURE 5.11: Antisymmetric stationary states in inhomogeneously coupled system. Left – amplitudes (absolute values) of wavefunction ψ_1 for various coupling strengths and fixed coupling width $w = 1$. Black curve represents homogeneous state of the decoupled system. Right – amplitudes of ψ_1 for fixed coupling strength $c_0 = 1$ and varying widths. After Ref. [195].

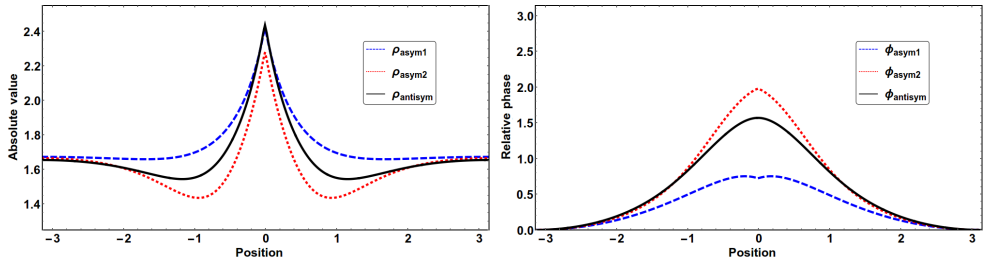

FIGURE 5.12: Absolute value $|\psi_1|$ (left) and relative phase (right) of the asymmetric (blue and red) and antisymmetric (black) states in case of narrow coupling $w = 0.01$. Antisymmetric and asymmetric state are calculated for $c_0 = 1$ and $c_0 = 1.5$ respectively. Phase oscillation term is calibrated so that $\phi_1(x = \pm\pi) = 0$. After Ref. [195].

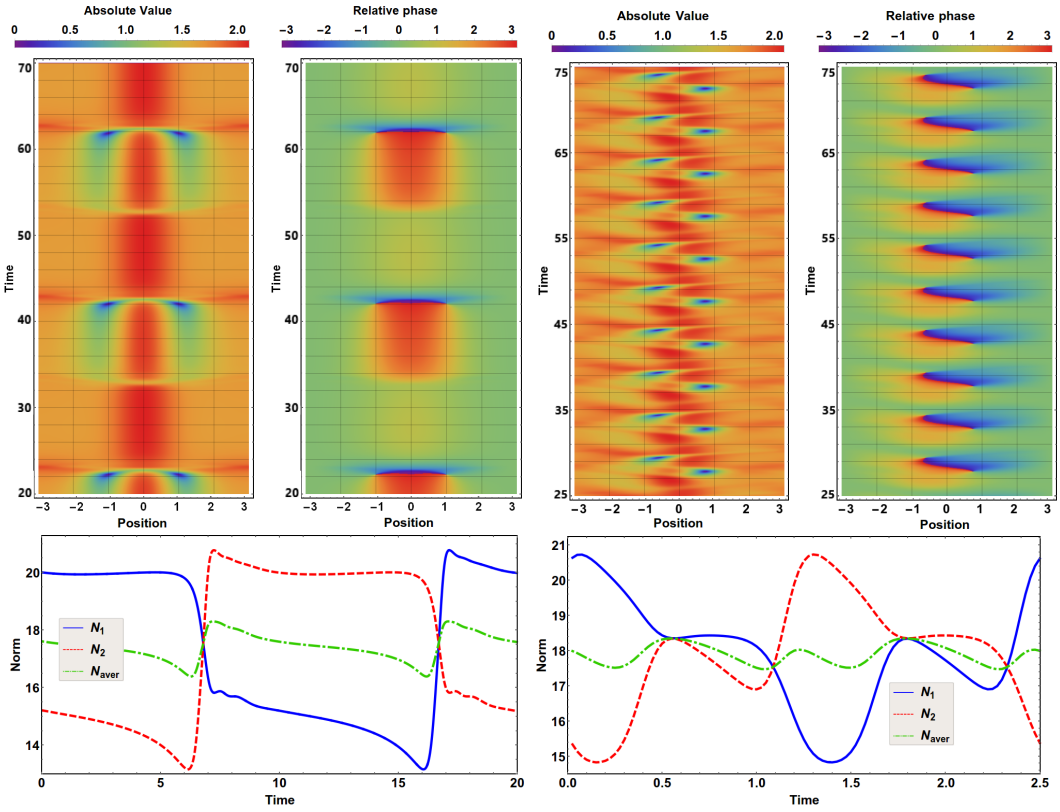

FIGURE 5.13: Top: pseudocolor plots of absolute values and relative phases of ψ_1 wavefunction component during limit cycle oscillations for $c_0 = 4$ (left) and $c_0 = 5$ (right). Oscillations of the second channel are shifted by half-period and reflected around $x = 0$ axis in case of asymmetric oscillations. Phase oscillation term is calibrated so that $\phi_1(x = \pm\pi) = 0$. Bottom: total norms in both channels and norm average during one oscillation period for $c_0 = 4$ (left) and $c_0 = 5$ (right). Coupling width is equal to $w = 1$ in both cases. After Ref. [195].

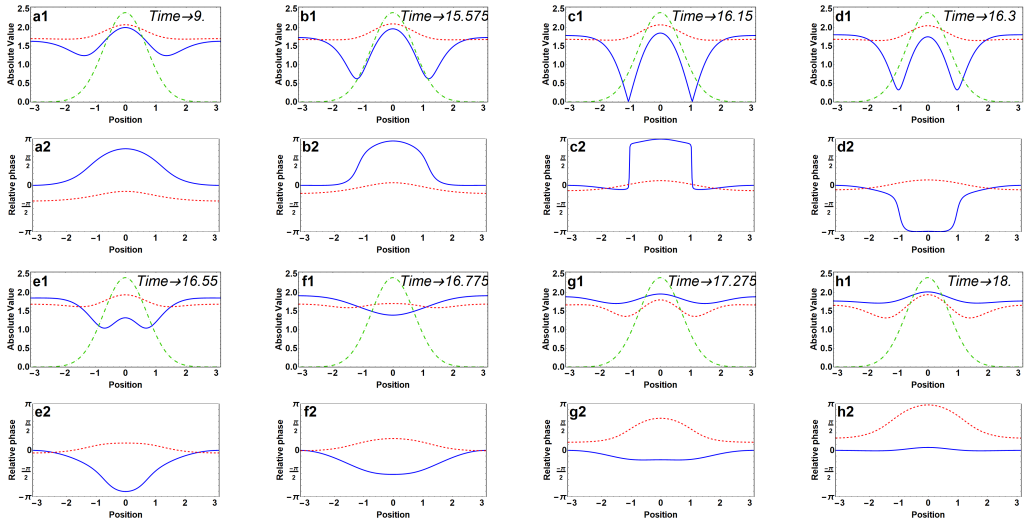

FIGURE 5.14: Snapshots of symmetric limit cycle oscillations, representing half-period of oscillation for $c_0 = 4, w = 1$. Frames are presented in pairs – top frames (a1-h1) show absolute values of wavefunctions ψ_1 and ψ_2 (blue and red curve respectively) and rescaled coupling distribution (green curve); bottom frames (a2-h2) show relative phases in both channels. Phase oscillation term is calibrated so that $\phi_1(x = \pm\pi) = 0$ (blue curve). After Ref. [195].

transience time – the time of transition from the initial state to established oscillations – increase with coupling strength. Snapshots of symmetric oscillations dynamics are shown in Figure (5.14).

The process of phase difference buildup can be explained once again through the treatment of coupling as a perturbation. The phase difference between two channels remains close to π during the whole oscillation period. Wavefunction phase inside the coupled region of one channel experiences additional drift due to the presence of coupling term, building up phase mismatch between coupled and uncoupled region. The formation of phase gradient leads to the depopulation of the regions around the coupled area. After a slight jump of phase velocity in coupled area, channels switch their roles and oscillations continue.

Further increase in coupling strength leads to new behavior, not observed in narrow coupling case – the creation of phase jumps on both sides of coupling potential loses simultaneity. This leads to periodic creation and annihilation of topological charges in both channels. Vortices, periodically appearing in each channel, maintain the same direction, opposing to vorticity reappearing in the other channel. Snapshots of asymmetric limit cycle oscillations are presented in Figure (5.15).

Oscillations frequency was also investigated. Results are presented in Figure (5.16). The panel on the left shows changes in oscillation frequency for different gain and coupling strengths. Frequency rapidly grows up with coupling strength until a jump from symmetric to asymmetric oscillations occurs. The frequency of asymmetric oscillations is linearly proportional to the coupling strength.

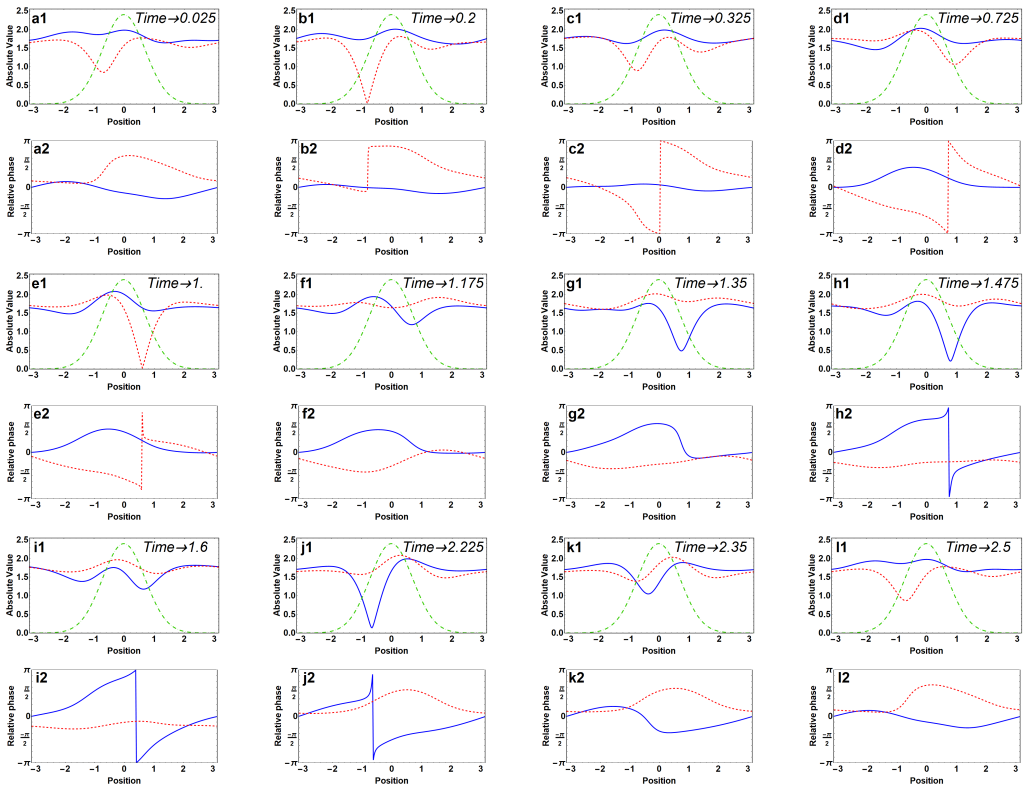

FIGURE 5.15: Snapshots of asymmetric limit cycle oscillations, representing full period of oscillation for $c_0 = 5, w = 1$. Frames are presented in pairs – top frames (a1-h1) show absolute values of wavefunctions ψ_1 and ψ_2 (blue and red curve respectively) and rescaled coupling distribution (green curve); bottom frames (a2-h2) show relative phases in both channels. Phase oscillation term is calibrated so that $\phi_1(x = \pm\pi) = 0$ (blue curve). After Ref. [195].

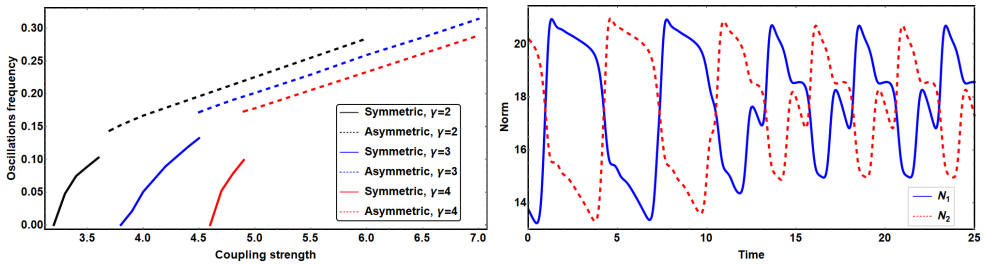

FIGURE 5.16: Left – frequency of the symmetric (solid lines) and asymmetric (dashed lines) limit cycle oscillations for three different values of γ. All calculations performed for $w = 1, \Gamma = 1$. Right – norm in both channels during oscillations transition for $c_0 = 4.5$ (point of blue line discontinuity on the left panel). After initial propagation (not shown) systems temporarily develops symmetric oscillations, which morph into asymmetric oscillations after several periods of oscillation. After Ref. [195].

One particularly interesting example can be observed near the point of transition between oscillation types (in the case of $\gamma = 3$ it appears around $J \simeq 3.5$). In this example, the initial state temporarily converges to a symmetrically oscillating state. Symmetric oscillations hold for 3-4 periods, depending on the perturbation. After that, the system develops an asymmetric type of oscillations. Right panel of Figure (5.16) shows changes in total norm during transition period, while Figure (5.17) presents snapshots of oscillations transition.

Asymmetric oscillations introduce a new method of ring state tailoring. In polariton condensates, the coupling is controlled through the additional laser beam, thus it can be instantly turned on and off. We've already established that homogeneous coupling can lead to the simultaneous creation of vortices in both rings. Asymmetric oscillations observed for inhomogeneous coupling temporarily create a vortex in one channel at a time. Simulations show that after removal of linear coupling states conserve their topological charge and quickly relax into homogeneous stationary states. Thus, we can turn off the coupling term during a certain interval of oscillation to conserve the vortex in one channel while having zero vorticity of the second channel.

Conclusion

Non-conservative coupled ring structures present a surprisingly rich landscape of attractors, including inhomogeneous, oscillating, and even chaotic states. We have identified several cases of symmetry breaking, both between and inside rings. Precise control over coupling allows for topological charge manipulation without additional stirring or a complex structure of interacting elements.

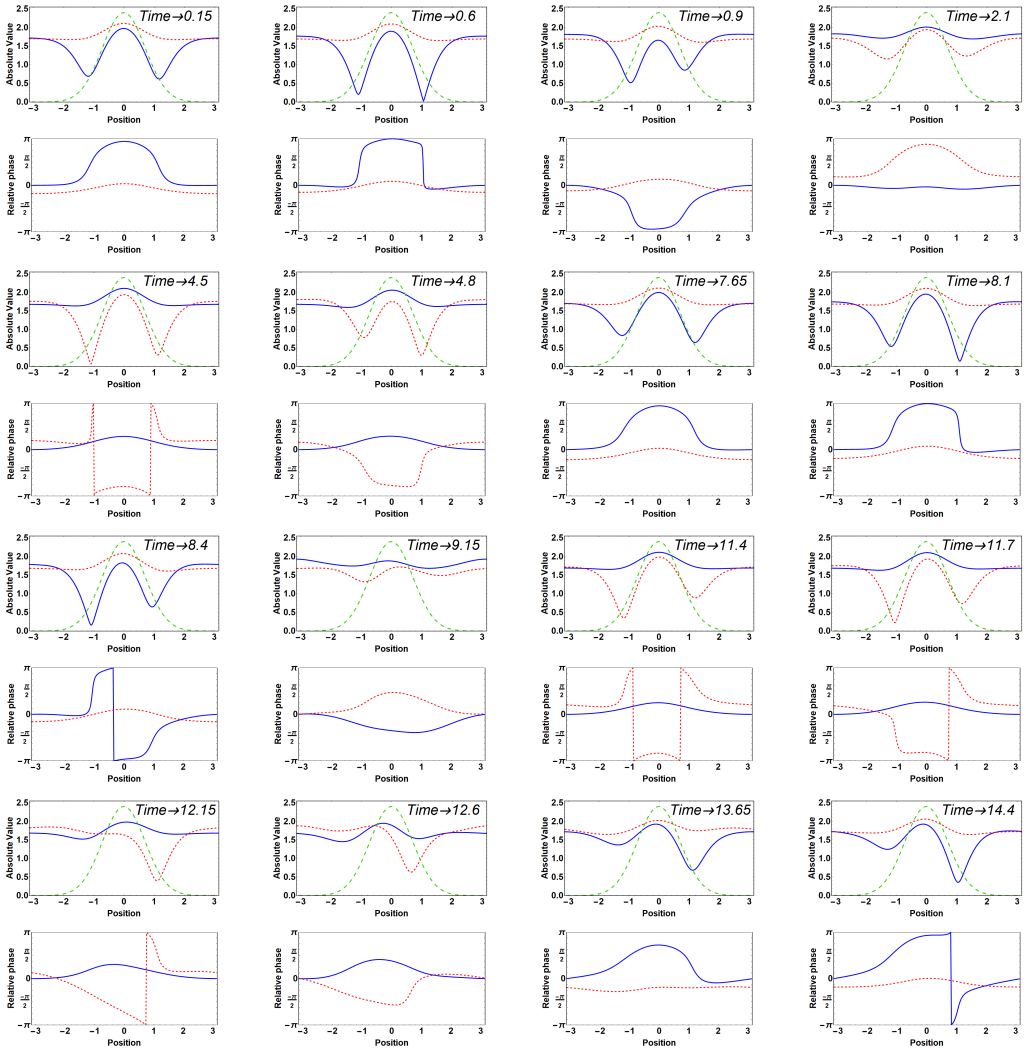

FIGURE 5.17: Snapshots of transition from symmetric to asymmetric oscillations for $c_0 = 4.5, w = 1$. Frames are presented in pairs – top frames show absolute values of wavefunctions ψ_1 and ψ_2 (blue and red curve respectively) and rescaled coupling distribution (green curve); bottom frames show relative phases in both channels. Phase oscillation term is calibrated so that $\phi_1(x = \pm\pi) = 0$ (blue curve). After Ref. [195].

Chapter 6

Nonlocal nonlinearity in coupled systems

Bright optical solitons have been investigated in various forms over the years [72, 47]. The main problem of traditional spatial solitons in Kerr optical media is their instability due to catastrophic collapse. Different approaches are used to counteract soliton instability, including spatial limitation of one transverse dimension [202], use of saturable media [203] or introduction of nonlocal nonlinearity [41]. This chapter specifically focuses on nematic liquid crystals as an example of a nonlocal nonlinear medium.

This chapter is divided into three sections. First, I introduce liquid crystals (particularly nematic liquid crystals) as an optical medium, and a special form of optical solitons, characteristic for nematic liquid crystals – nematicons. In the second section, I display the system of equations used for nematicons simulation and its approximation with interacting nonlocal nonlinearities based on [204]. The third section presents my research of supermode solitons, published in [205], and expands on it with the analysis of trajectory bending instability.

6.1 Nematic liquid crystals and nematicons

Liquid crystals (LCs) are an intermediate state of matter between solid and liquid phase [206, 207]. Typically LCs are formed from long organic molecules. These molecules interact with each other, maintaining correlation in their positions, while simultaneously being able to flow like a liquid. Liquid crystalline phases – also known as mesophases – are categorized according to the parameters required for mesophase existence. Mesophase creation may depend on molecules concentration in the solvent in the case of lyotropic LC, or the presence of inorganic elements in the case of metallotropic LC. In this chapter I will focus on thermotropic LCs – their phase transitions are defined by temperature – as the temperature can be easily and reversibly changed in LC cells.

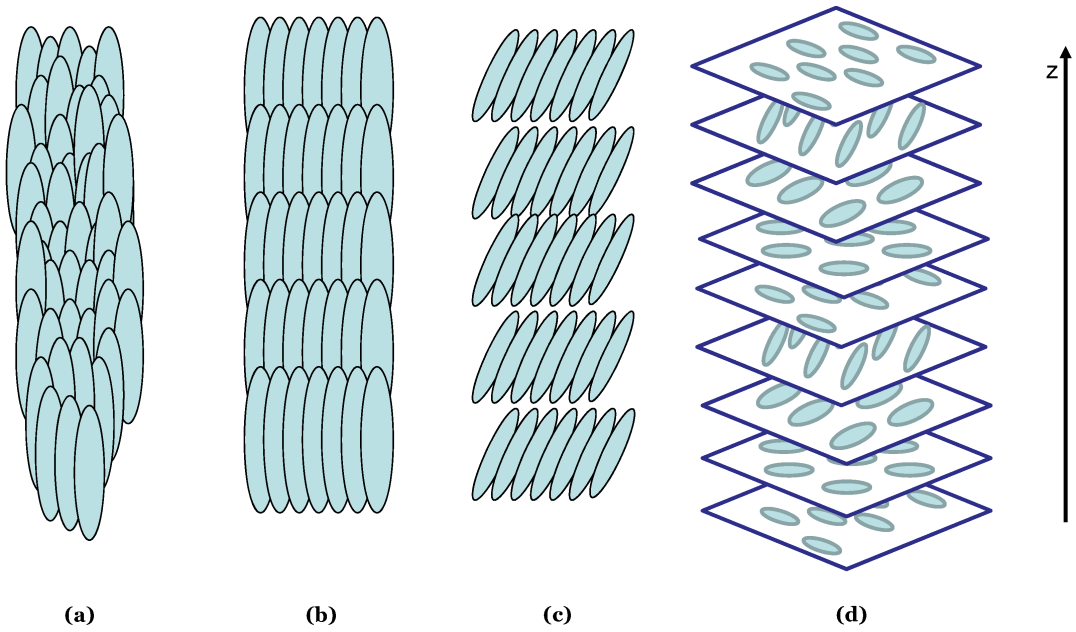

FIGURE 6.1: Schematic representation of molecules positioning in different LC phases. (a) – Nematic, (b) – Smectic A, (c) – Smectic C, (d) – Cholesteric (chiral nematic). After Ref. [208].

LCs mesophases are divided into multiple types, based on molecules distribution. The most known types of LC phases are nematic and smectic phases. Molecules of nematic LC have randomly distributed centers of mass, while all molecules have approximately the same direction of their long axes. Smectic LC is additionally structured – molecules in smectics are packed in layers. Furthermore, molecules directions may change from layer to layer, creating helical structures. These forms are known as chiral nematics/smectics or cholesterics. Visual representations of different mesophases are presented in Figure (6.1).

The molecular structure of LC directly impacts its optical properties. Rod-like molecular shapes induce high anisotropy of electric permittivity and refractive index. Waves oscillating perpendicular or parallel to the molecule central axis are called ordinary and extraordinary waves respectively.

Just as molecules orientation influences multiple LC properties, there are many ways to influence LC orientation. Temperature rise decreases molecules ordering, in extreme cases leading to phase transition and total loss of crystalline structure. LC orientation can also be controlled through the presence of an external electric field [209, 210]. Borders of LC cells can be designed through rubbing so that molecules next to the cell borders have precisely defined initial orientation [211, 212]. The influence of boundary conditions on the orientation decreases inside LC bulk, however, it is still the defining condition in an equilibrium state.

Reorientation of LC molecules can be induced by optical beam propagation. Reorientation nonlinearity appears because the optical field exerts a torque on molecules,

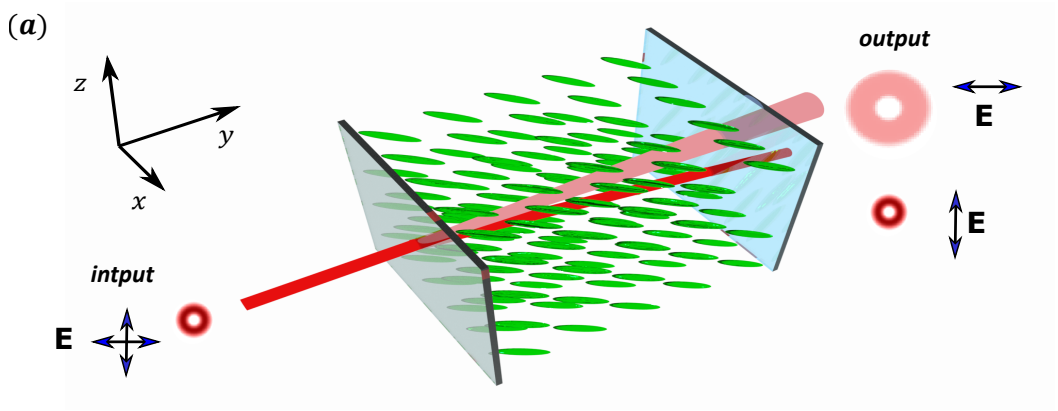

FIGURE 6.2: Example of experimental setup for exploration of soliton propagation in nematic LC cell. Initial beam propagates in linear regime or forms a soliton depending on the polarization in respect to the LC molecules. After Ref. [213].

rotating them to stand according to the electric field. In turn, reorientation shifts birefringence axes and influences the refractive index. Reorientation nonlinearity is incoherent, due to the slow reaction time of LC, nonlocal, due to the intramolecular interactions in the fluid, and saturable, as reorientation angle has the maximum value.

An optical beam can increase the refractive index of the material proportionally to its intensity due to the mechanism described above. Beam becomes confined in a self-induced waveguide, limiting its diffraction. This process creates a new type of solitons, characteristic for nematic LC – nematicon [214, 215]. An example of an experimental setup used for nematicon research is presented in Figure (6.2).

Nematicons have been extensively researched in literature [216, 217, 218]. This section focuses specifically on coupled beams in nematic LC – vector nematicons [219, 220, 221]. Vector nematicons are created by injecting several beams with different wavelengths at the same place and direction. Molecules of LC experience the total intensity of the combination of the beams. An example of experimentally observed vector nematicon is presented in Figure (6.3).

Vector nematicon dynamics can be changed through the addition of wavelength-specific absorption. Introduction of absorptive dye, while depleting soliton power, drastically increases nonlinear response [222]. Furthermore, the absorption process increases LC temperature in the propagation area, thus influencing LC refractive index. Temperature effects create additional defocusing interaction, which can be used for further beam stabilization [115, 223]. To conclude, the analysis of nonlocal coupling in the following chapters is based on vector nematicons with competing reorientation and temperature interactions.

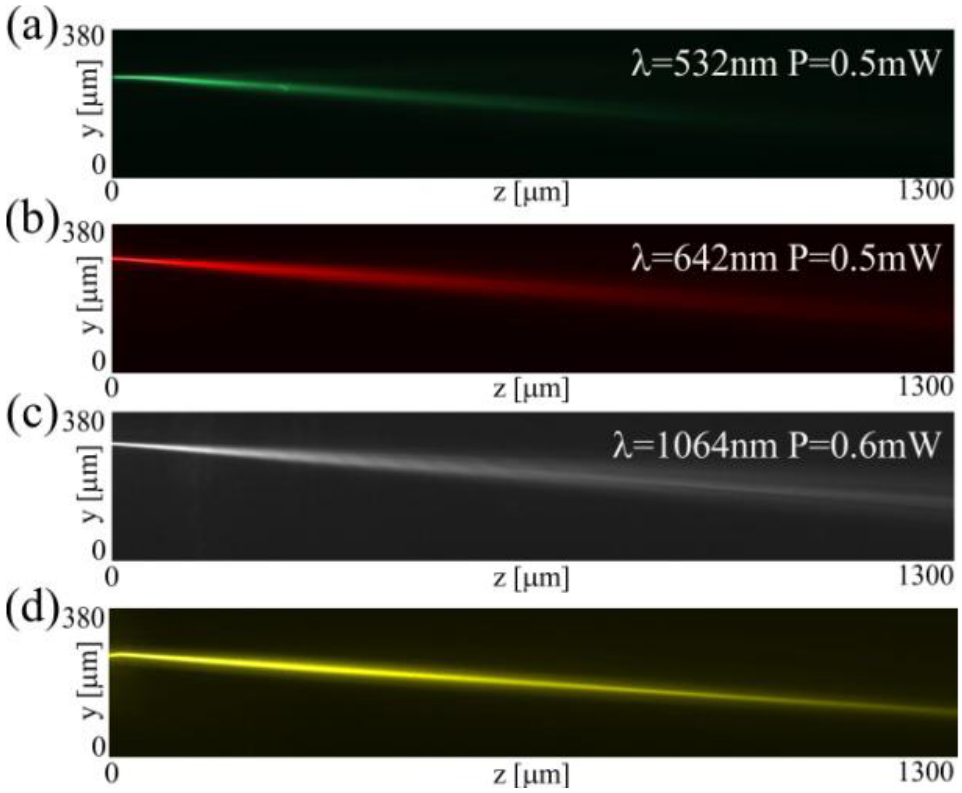

FIGURE 6.3: Experimental observation of three-colour vector nematicon. Each of the three components diffracts during separate propagation (a-c), but they form soliton once launched together (d). After Ref. [221].

6.2 Nonlocal model of liquid crystal medium

The full model of beam propagation in nematic LC includes differential equations for the optical field, molecular orientation, and temperature. Electric field propagation is based on paraxial equation for the uniaxial anisotropic media [224, 225].

$$2ik_0 n_{ref}\left(\partial_z E + \tan\delta\partial_x E\right) = \partial_{yy}E + D_a\partial_{xx}E + k_0^2\left(n^2(\theta,T) - n_{ref}^2\right)E \tag{6.1}$$

where E is electric field amplitude, $k_0 = \dfrac{2\pi}{\lambda}$ is the central propagation constant, n_{ref} is reference frame refractive index, $n(\theta,T)$ is LC refractive index dependent on molecules orientation angle θ and temperature T, D_a is dispersion anisotropy coefficient and $\delta(\theta)$ is walk-off angle. Choice of n_{ref} is arbitrary, but typically $n_{ref} = n(\theta_0, T_0)$ gives best results from numerical point of view [226].

Derivation of equation 6.1 assumes specific orientation of LC cell and light polarization – LC molecules are aligned in yz plane and electric field is polarized in y direction, as presented in Figure (6.4). Dispersion term in y direction can be compensated through a combination of geometric confinement and nonlinear processes and will be neglected in the following steps.

Anisotropy of nematic LC leads to the appearance of the walk-off angle δ. This effect can be compensated by applying moving frame substitution $E' = Ee^{i(2k_0 n_{ref}\tan\delta)x}$. In the case of multiple co-propagating nematicons, walk-off angles may be slightly different for different components. This misalignment might be compensated by focusing different beams entering LC under corrected angles.

Geometry considerations presented above lead to the one-dimensional form of the propagation equation.

$$2ik_0 n_{ref}\partial_z E' = D_a\partial_{xx}E' + k_0^2\left(n^2(\theta,T) - n_{ref}^2\right)E' \tag{6.2}$$

Nematic LC is a birefringent material, defined by ordinary and extraordinary refractive indices n_o and n_e. Typically, $n_e < n_o$. The refractive index of liquid crystals is approximately time-independent, as we are interested in stationary solutions, and LC response time is much slower than oscillation period [227]. Refractive index, perceived by optical beam, depends on relative molecules orientation

$$n(\theta,T) = \frac{n_o(T)n_e(T)}{\sqrt{n_o^2(T)\sin^2\theta + n_e^2(T)\cos^2\theta}} \tag{6.3}$$

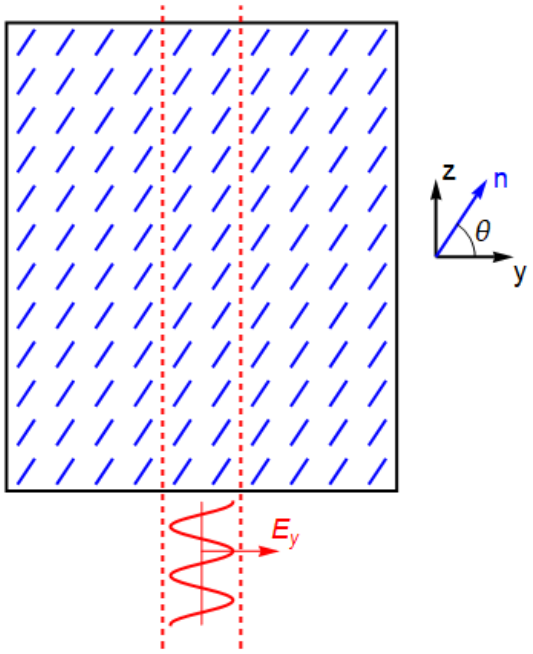

FIGURE 6.4: Schematic representation of optical beam (red) propagation in LC cell with planar orientation of molecules (blue). E_y is the electric field polarization vector and n is the molecule orientation vector.

where θ is an angle between molecule orientation vector $\vec{n}$ and beam polarization vector $\hat{E}_y$. Both n_e and n_o are temperature-dependent. Temperature increase lowers LC ordering and decreases LC birefringence $\Delta\epsilon = n_o^2(T) - n_e^2(T)$. Exact temperature effect on the refractive index is typically measured experimentally [228].

Molecules orientation is calculated by minimizing LC energy density f. LC energy density consists of electric field interaction term f_{el} and LC deformation term, based on Frank's equation [229].

$$f_{el} = -\frac{\epsilon_0}{2}\left[\left(n_e^2 - 1\right)|E|^2 + \Delta\epsilon\left(\vec{E}\cdot\vec{n}\right)^2\right] \tag{6.4}$$

$$f_{fr} = \frac{K_{11}}{2}\left(\nabla\cdot\vec{n}\right)^2 + \frac{K_{22}}{2}\left(\vec{n}\cdot\nabla\times\vec{n} + G\right)^2 + \frac{K_{33}}{2}\left(\vec{n}\times\nabla\times\vec{n}\right)^2 \tag{6.5}$$

where K is the elasticity coefficient, and G is the chirality number. Total energy density can be minimized through Euler-Lagrange equations [230]. The general result depends on a huge system of equations for two orientation angles. This system can be remarkably simplified through a combination of assumptions and particular cell geometry [231]. Elasticity constants are assumes to be mutually equal and independent from temperature $K_{11} = K_{22} = K_{33} = K$. This assumption, combined with previously established LC cell architecture – molecules are aligned in yz plane, the electric field is linearly polarized in y direction – final equation for molecular orientation.

$$\partial_{xx}\theta = \frac{\epsilon_0 \Delta\epsilon}{2K}|E|^2 \sin(2\theta) \tag{6.6}$$

The temperature of LC is influenced by the absorption of optical beam energy. The temperature distribution is governed by the heat equation

$$\partial_{xx}T = -\frac{c\epsilon_0 \alpha}{2\kappa}|E|^2 \tag{6.7}$$

Combined equations 6.2, 6.6 and 6.7 can be used to simulate nematicon propagation in a precise manner. One of my publications explores the influence of temperature and absorption effects on vortex solitons stability [115]. This publication remains out of the scope of my thesis, as the model presented above is not based on NLSE.

Full system of equations (6.2, 6.6, 6.7) is numerically demanding in terms of calculations. Instead, reorientational and thermal nonlinearity can be presented as nonlocal nonlinear responses [204], leading to NLSE-like equation.

This representation is based on two assumptions of variables separation. First, we neglect temperature dependence of $\frac{\Delta\epsilon\epsilon_0}{K}$ – in other words, we assume that orientation angle depends only on the electric field intensity. Second, we transform refractive index term, using $\frac{\Delta\epsilon}{n_o^2} \ll 1$

$$n^2(\theta,T) - n_{ref}^2(\theta_0,T) = n_o^2 n_e^2 \left[\frac{1}{n_o^2 + \Delta\epsilon\cos^2\theta} - \frac{1}{n_o^2 + \Delta\epsilon\cos^2\theta_0}\right] \simeq$$
$$\simeq \frac{n_e^2 \Delta\epsilon}{n_o^2}\left(\cos^2\theta - \cos^2\theta_0\right) = P(T)\Theta(\theta,\theta_0) \tag{6.8}$$

If the LC cell is sufficiently large, its boundaries don't influence temperature and orientation near the propagation region. In this case, both responses can be substituted with nonlinear response distributions. Equation 6.1 with nonlocal response takes the following rescaled form

$$i\partial_Z\psi = \frac{1}{2}\partial_{XX}\psi + \alpha\left(|\psi|^2\right)\beta\left(|\psi|^2\right)\psi \tag{6.9}$$

where $\alpha\left(|\psi|^2\right)$ and $\beta\left(|\psi|^2\right)$ represent phenomenological functions of reorientational and thermal nonlinearity respectively

$$\alpha\left(|\psi|^2\right) = \left[R_\alpha(X) * |\psi|^2\right], \beta\left(|\psi|^2\right) = 1 - B\left[R_\beta(X) * |\psi|^2\right], \tag{6.10}$$

B is the relative strength of thermal defocusing nonlinearity,

$$R_{\alpha,\beta} = \frac{1}{\sigma_{\alpha,\beta}\sqrt{\pi}} \exp\left[-\left(\frac{X}{\sigma_{\alpha,\beta}}\right)^2\right] \tag{6.11}$$

is normalized nonlocal response function, and $f(x) * g(x) = \int f(x-x')g(x')dx'$ is convolution operation.

Convolution operation has several advantages from a numerical point of view. The appearance of convolution in coupled equations does not influence conservation laws. Numerically, convolutions can be calculated with an FFT algorithm.

$$f(x) * g(x) = \mathcal{F}^{-1}\left(\tilde{f}\tilde{g}\right) \tag{6.12}$$

Equation 6.9 presents so-called multiplicative model of nonlinearity [232, 233], as different nonlinear terms are multiplied. As a result, thermal effects have fifth order of nonlinearity. Another approach uses the additive model of nonlinearity [234]. In this case, rescaled nonlinear function maintains its linear and nonlinear components

$$\alpha\left(|\psi|^2\right) = n + \left[R_\alpha(X) * |\psi|^2\right], \beta\left(|\psi|^2\right) = 1 - B\left[R_\beta(X) * |\psi|^2\right] \tag{6.13}$$

The resulting nonlinear term can be limited to third-order effects

$$\alpha\left(|\psi|^2\right)\beta\left(|\psi|^2\right) = n + \left[R_\alpha * |\psi|^2\right] - nB\left[R_\beta * |\psi|^2\right] + \mathcal{O}(|\psi|^4) \simeq n_{lin} + \alpha' - \beta' \tag{6.14}$$

Substitution $\psi' = \psi e^{-inZ}$ eliminates linear term. Final additive model equation takes following form.

$$i\partial_Z\psi' = \frac{1}{2}\partial_{XX}\psi' + \alpha'\left(|\psi'|^2\right)\psi' - \beta'\left(|\psi'|^2\right)\psi' \tag{6.15}$$

The additive model uses only third-order nonlinearity terms, thus it can be applied to a wider range of materials. The next section considers two coupled nonlocal nonlinear equations with additive nonlinearity.

6.3 Supermode spatial solitons in nonlocal media

Competing nonlocal nonlinearities lead to the creation of a new soliton family – supermode solitons [204, 228]. Typically fundamental spatial solitons have a one-peak bell shape. Supermode solitons possess multiple peaks while maintaining constant phase front characteristics for fundamental solitons. Two-peak supermode solutions

were found in the case of both multiplicative and additive models [234]. The primary goal of my research [205] was to explore possible vector supermode solitons.

6.3.1 Rescaled coupled model

The following model assumes co-propagation of both beam components. One of the components induces defocusing. Energy loss due to absorption is neglected unless stated otherwise. We assume that the nonlinear refractive index is wavelength-independent. For simplicity's sake, a component with both focusing and defocusing elements is described as a "defocusing channel", while a component without defocusing term is called "focusing channel".

Initially coupled equations are based on beam evolution with slowly varying envelope

$$\begin{cases} -2in_{01}k_{01}\partial_z E_1 = \partial_{xx}E_1 + 2n_{01}n_{NL}k_{01}^2 E_1 \\ -2in_{02}k_{02}\partial_z E_2 = \partial_{xx}E_2 + 2n_{02}n_{NL}k_{02}^2 E_2. \end{cases} \tag{6.16}$$

where E_1 is focusing beam electric field, E_2 is defocusing beam electric field, n_{0m} are reference linear refractive indices in m-th channel, $k_{0m} = \frac{\omega_m}{c}$ are m-th propagation constants, and n_{NL} is nonlinear refractive index, consisting of the following terms

$$n_{NL} = \rho_1 \left[R_f * |E_1|^2\right] + \rho_2 \left[R_f * |E_2|^2\right] - \beta \left[R_d * |E_2|^2\right] \tag{6.17}$$

Here $R_{f,d} = \frac{1}{\sqrt{\pi}\sigma_{f,d}} e^{-x^2/\sigma_{f,d}^2}$ are focusing and defocusing nonlocal response functions respectively. Equations 6.16 and 6.17 can be rescaled into dimensionless form with $X = \frac{x}{\sigma_f}$, $Z = \frac{-z}{2n_{02}k_{02}\sigma_f^2}$, $\psi_m = \sqrt{\frac{2n_{02}k_{02}^2\sigma_f^2\alpha \int |E_1|^2 dx}{\int |E_m|^2 dx}} E_m$. In order to gain dimensions intuition, we can assume values of parameters, typical for LC experiments – $n_{01} = 1.5, \lambda_1 = \frac{2\pi}{k_{01}} = 1\mu m, \sigma_f = 10\mu m$. These parameters lead to $x = 10\mu m * X, z \simeq 1.9mm * Z$.

Coupled nonlinear equations take the following rescaled form

$$\begin{cases} i\partial_Z \psi_1 = \frac{1}{NK}\partial_{XX}\psi_1 + KF\left(\psi_1, \psi_2\right)\psi_1 \\ i\partial_Z \psi_2 = \partial_{XX}\psi_2 + F\left(\psi_1, \psi_2\right)\psi_2 \end{cases} \tag{6.18}$$

with a following joint nonlinear potential:

$$F\left(\psi_1, \psi_2\right) = A\left[R_f * |\psi_1|^2\right] + (1-A)\left[R_f * |\psi_2|^2\right] - \mathrm{B}\left[R_d * |\psi_2|^2\right] \tag{6.19}$$

Here $K = \frac{k_{02}}{k_{01}}$ represents wavelength ratio between beam components, $N = \frac{n_{02}}{n_{01}}$ is linear refractive index ratio, $\mathrm{A} = \frac{\rho_1 \int |E_1|^2 dx}{\rho_1 \int |E_1|^2 dx + \rho_2 \int |E_2|^2 dx}$ is the relative focusing strength of the focusing channel, and $\mathrm{B} = \frac{\beta \int |E_2|^2 dx}{\rho_1 \int |E_1|^2 dx + \rho_2 \int |E_2|^2 dx}$ is the defocusing strength. In the above, beam amplitudes are scaled to identical powers $P = \int |\psi_1|^2 dx = \int |\psi_2|^2 dx$. Nonlinear response functions take following rescaled form

$$R_f = \frac{1}{\sqrt{\pi}} e^{-X^2}, R_d = \frac{1}{\sqrt{\pi}\sigma} e^{-X^2/\sigma^2} \tag{6.20}$$

where $\sigma = \frac{\sigma_d}{\sigma_f}$ is nonlocality range ratio. All simulation results presented below were also performed with Lorenzian profiles $R \sim \frac{\sigma^2}{X^2 + \sigma^2}$ – distribution shape has negligible effects on both soliton shape and its stability properties. Note that two channels in equations 6.18 are not symmetrical in terms of coupling interactions.

6.3.2 Family of supermode states

Nonlocal coupled nonlinear equations are generally non-integrable, thus a system of equations 6.18 was explored with numerical methods. The accelerated imaginary time method was used to find soliton states, and the finite-difference beam propagation method was utilized to explore soliton propagation and stability.

Pseudo-scalar soliton case

Vector soliton equations 6.18 can be degenerated back to scalar system in two cases. If $A = 0$, the focusing beam does not influence nonlinear effects at all – it simply co-propagates inside the waveguide, induced by defocusing beam. Wave equation for defocusing beam takes the exact form discussed in [234]. Physically $A = 0$ case corresponds to focusing beam with negligible power in comparison with the defocusing beam. On the other hand, in case of $K = N = 1$ both equations become identical and have symmetric solutions $\psi_1 = \psi_2$. Physically $N = K = 1$ case corresponds to two components with very similar wavelengths. It is worth mentioning, that even though both cases lead to the same scalar equation and the same supermode states, their dynamics are significantly different. I will discuss the scalar supermode case based on the $N = K = 1$ assumption. Examples of scalar supermode states are presented in Figure (6.5).

The appearance of multiple humps can be analyzed through nonlinear potential exploration. Nonlinear potential in its scalar limit takes the following form.

$$F(\psi) = \left[R_f * |\psi|^2\right] - B\left[R_d * |\psi|^2\right] \tag{6.21}$$

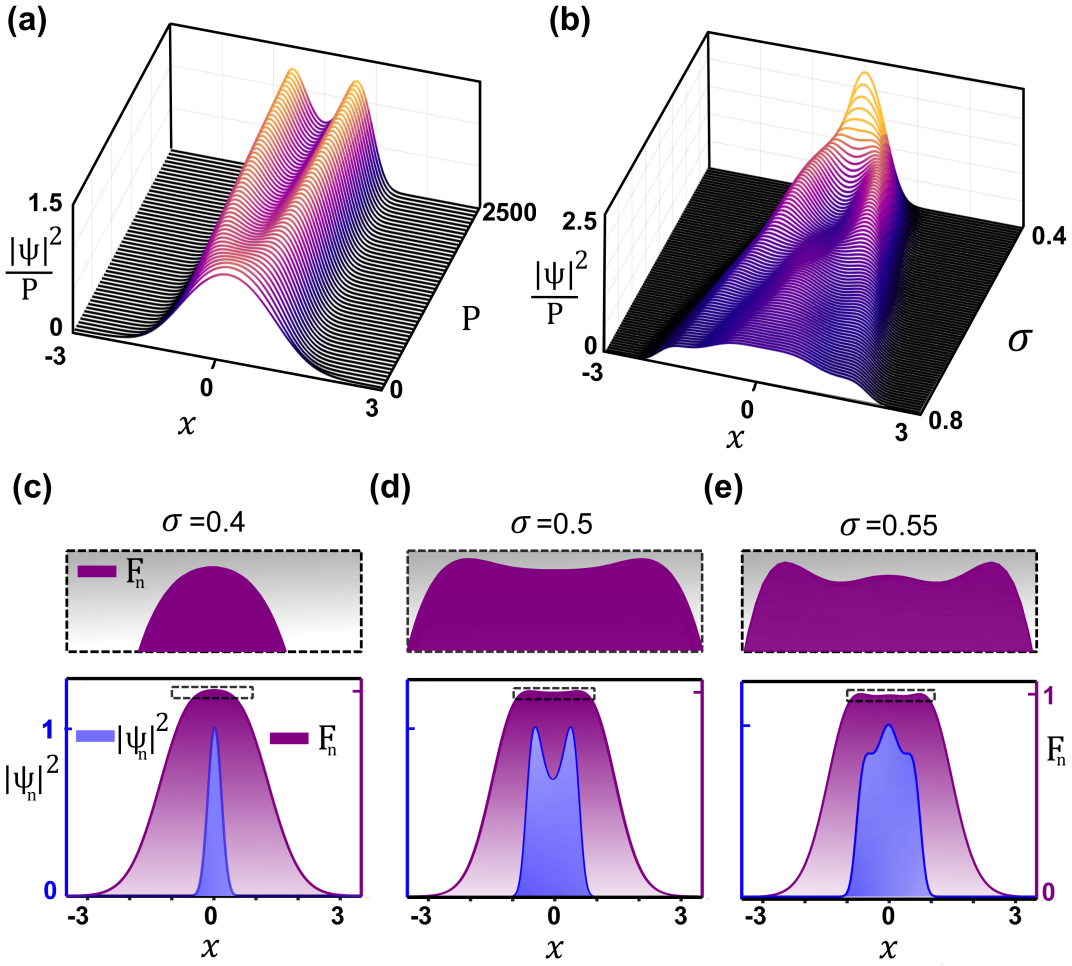

FIGURE 6.5: Formation of scalar supermode solitons for $N = K = 1, A = 1, B = 0.5$. (a) – wavefunction profile for nonlocality ratio $\sigma = 0.7$ and different values of power P. (b) – wavefunction profile for different values of nonlocality ratio σ and power $P = 2500$. (c-e) – Normalized intensity (blue) and nonlinear potential (magenta) distributions for one-peak (c), two-peak (d) and smoothed peak (e) states. Distributions are normalized so that $\psi_{max} = 1$ and $F_{max} = 1$. Dashed boxes are zooms of nonlinear potential shapes near beam center. After Ref. [205].

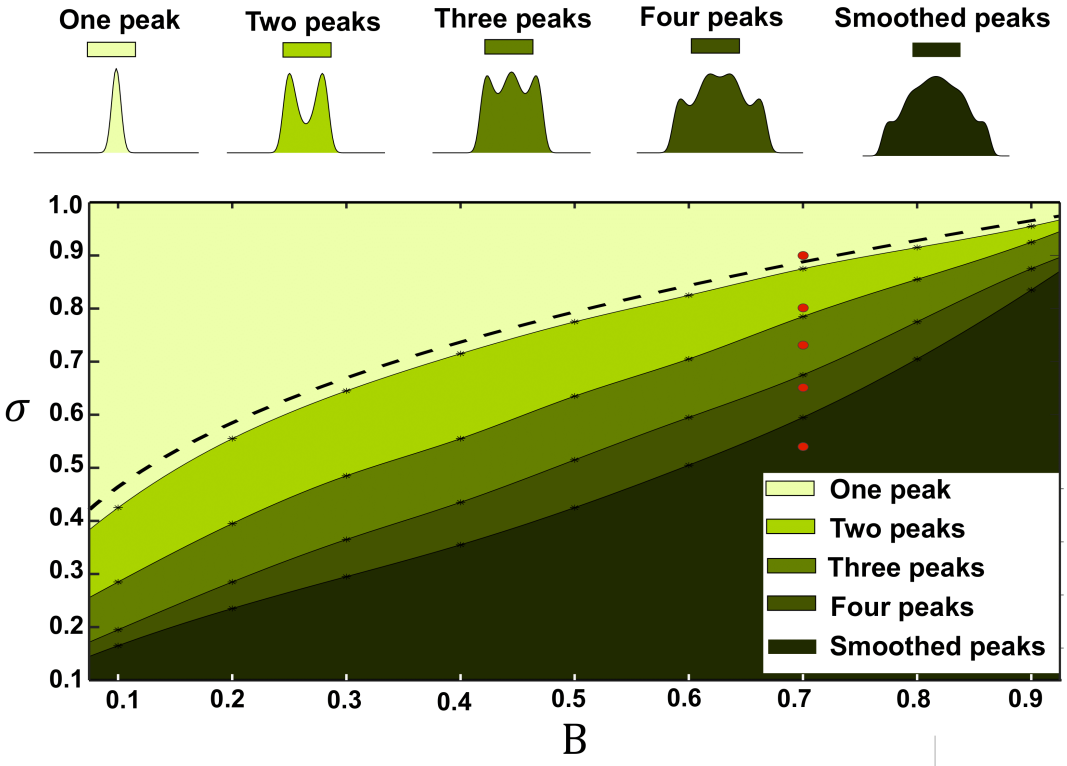

FIGURE 6.6: Scalar supermode states map for $N = K = 1, P = 2500$. Top graphs show intensity profiles calculated at $B = 0.7$ points marked by red circles on the bottom map. Profile colors correspond to map regions colors. Dashed line represents $\sigma = \sqrt[3]{B}$ curve. After Ref. [205].

In a low power regime, soliton maintain a one-hump shape, which can be approximated with Gaussian function

$$\psi_1 = \psi_2 = \psi_{max} \exp\left(-\frac{X^2}{w^2}\right) \tag{6.22}$$

Nonlinear potential maintains similar shape with potential width $w_f \simeq \sqrt{w^2+1}$. Power increase leads to potential flattening inside the beam region, due to increasing competition between focusing and defocusing nonlinear processes.

Several conditions for supermode appearance can be introduced through this approach. First, bright solitons require positive nonlinearity, leading to defocusing strength limit $0 < B < 1$. Formation of multihump structure requires the appearance of local minimum in nonlinear potential. Defocusing nonlinearity has to be more localized, thus $0 \leq \sigma < 1$. Third condition is found by evaluating second derivative condition $\partial_{XX} F|_{X=0} > 0$.

$$\left(\frac{\sqrt{w^2+2\sigma^2}}{\sqrt{w^2+2}}\right)^3 < B \tag{6.23}$$

This condition can be simplified by assuming high medium nonlocality $\sigma \geq w$.

$$\sigma < \sqrt[3]{B} \tag{6.24}$$

As the nonlocality ratio decreases, peaks are separated further and additional structures begin to form. Eventually, additional peaks merge into the smoothed triangular profile. A complete map of supermode states in the scalar case is shown in Figure (6.6).

Vector soliton case

Next step is to explore vector supermodes for $K \neq 1$. For simplicity's sake, we assume $N = 1$, as refractive index dispersion is relatively small within optical frequencies. Changes in focusing beam strength A have no qualitative influence on supermode states. Examples of supermode solitons for $A = 0$ and $A = 1$ are shown in Figure (6.7.b). The following analysis assumes $A = 1$ unless stated otherwise.

Simulations show a significant difference between $K > 1$ and $K < 1$ cases. Accelerated imaginary time does not converge into supermode states for $K > 1$, revealing the linear instability of these states. Supermode states still can be explored for $K > 1$ by utilizing the imaginary time method without preconditioning and acceleration terms. This "stripped" imaginary time temporarily converges to meta-stable fundamental states. For $K \leq 1$ accelerated imaginary time method finds linearly stable supermode states.

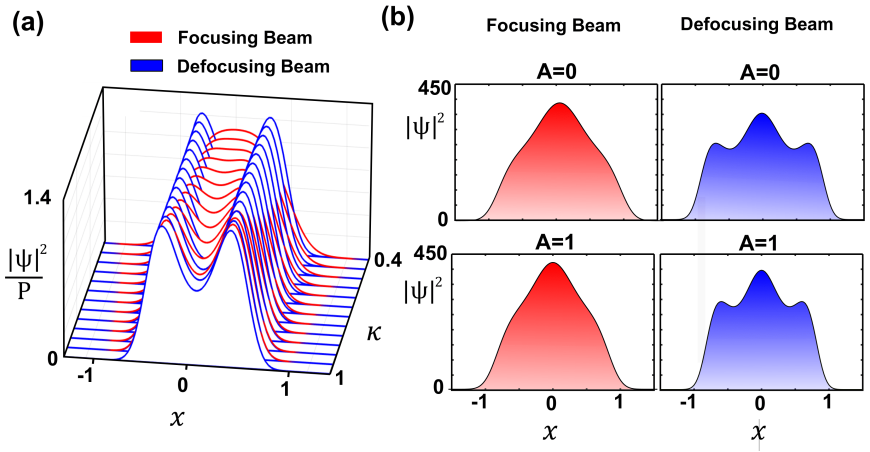

FIGURE 6.7: (a) – Two-hump soliton profiles for different values of wavelength ratio K and $B = 0.5, \sigma = 0.7, P = 2500$. (b) – Three-hump soliton profiles for $A = 0$ and $A = 1$, with the remaining parameters $K = 0.6, B = 0.6, \sigma = 0.6, P = 2500$. After Ref. [205].

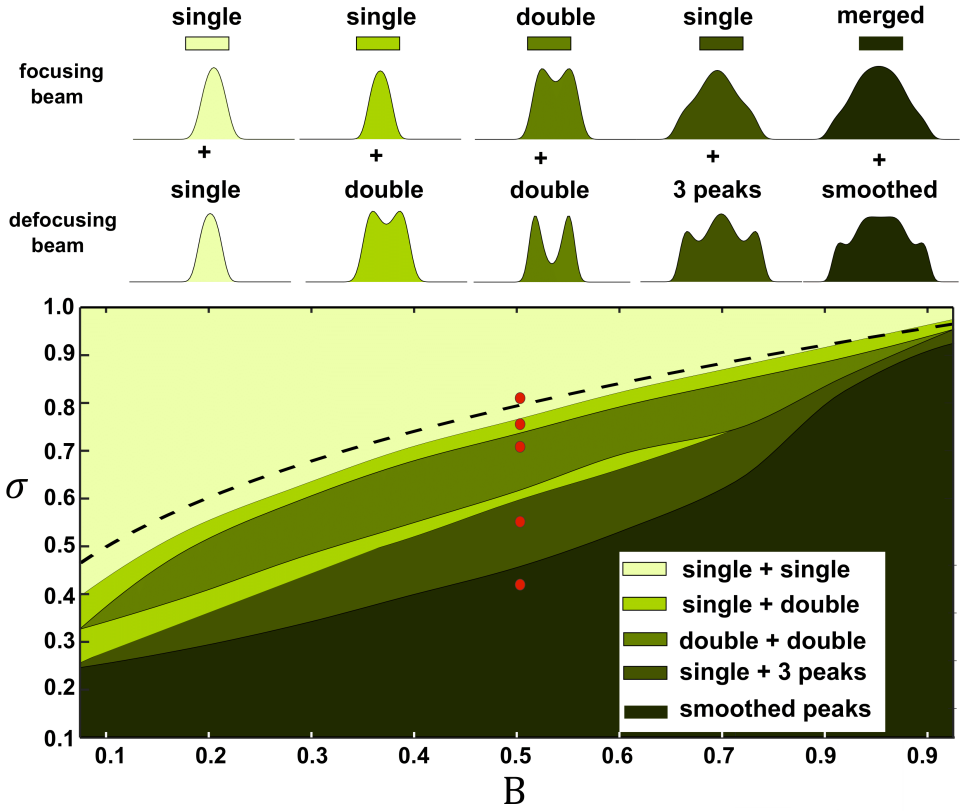

FIGURE 6.8: Vector supermode states map for $K = 0.6, P = 2500$. Top graphs show intensity profiles calculated at $B = 0.5$ points marked by red circles on the bottom map. Profile colors correspond to map regions colors. Dashed line represents $\sigma = \sqrt[3]{B}$ curve. After Ref. [205].

Comparison of supermode states for different values of K is shown in Figure (6.7.a). A decrease of K decreases the nonlinearity-to-diffraction ratio for the focusing beam, reducing the steepness and number of peaks. Below a certain value of K focusing beam doesn't form shapes with three or more peaks, transforming from two-peak structures straight to triangular shapes. Vector supermode soliton map for $K = 0.6$ is shown in Figure (6.8). The dependence of defocusing beam shape on B and σ remains qualitatively the same as for the scalar case.

6.3.3 Dynamics of nonlocally coupled solitons

Soliton stability was checked by simulating the propagation of vector supermode with 0.1% random amplitude noise in both channels. Typical propagation results are shown in Figure (6.9). The most noticeable property of vector solitons is their curved trajectory. All solitons observed for $A > 0$ develop trajectory bending during propagation, even in the $N = K = 1$ case. Trajectory bending is random and noise-dependent, but it does not show chaotic dynamics properties. This behavior will be discussed thoroughly in the next subsection.

In addition to trajectory bending, vector solitons found for $K > 1$ develop instability of the structure, visible in Figure (6.9.a). The focusing component develops oscillations in peaks steepness, leading to soliton destruction (not shown). Propagation distance before soliton collapse rises asymptotically to infinity as K approaches unity. This instability can be explained through the increase of the nonlinearity-to-diffraction ratio for the focusing beam. This hypothesis is confirmed by the fact that vector solitons remain stable for $K > 1$ as long as $N = \frac{1}{K^2}$.

Supermode solitons observed for $K \leq 1$ are often destroyed by intense perturbations, caused by trajectory bending. An example of such behavior is shown in Figure (6.9.b). Once again, solitons become less susceptible to collapse as K approaches unity. Vector solitons observed in pseudo-scalar case $N = K = 1$, while showing trajectory bending, remain stable.

Defocusing nonlinearity is often connected with energy losses, as was explained in the previous section. Absorption can be included by adding linear losses terms to the equations.

$$\begin{cases} i\partial_Z \psi_1 = \frac{1}{NK}\partial_{XX}\psi_1 + KF\left(\psi_1, \psi_2\right)\psi_1 \\ i\partial_Z \psi_2 = \partial_{XX}\psi_2 + F\left(\psi_1, \psi_2\right)\psi_2 - i\alpha_0\psi_2 \end{cases} \tag{6.25}$$

where α_0 is the absorption coefficient. Typical results of vector soliton propagation in the dissipative system are presented in Figure (6.9.c). Trajectory bending still appears during early propagation. Additionally, vector soliton slowly evolves into

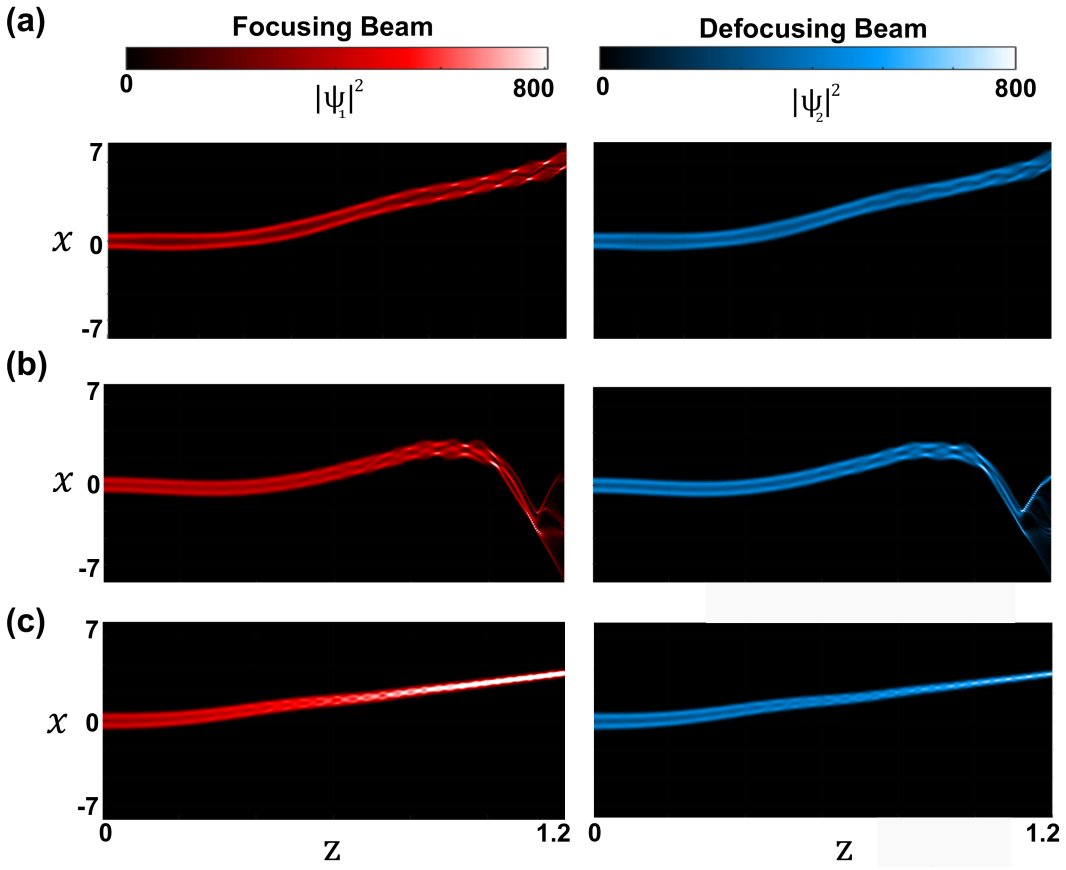

FIGURE 6.9: Examples of two-hump vector soliton propagation for $B = 0.5, \sigma = 0.65, P = 2500$. (a) – Meta-stable propagation for $K = 1.2$. (b) – Soliton collapse for $K = 0.9$. (c) – Soliton evolution for $K = 0.9$ with absorption coefficient $\alpha_0 = 0.25$. After Ref. [205].

a one-peak shape as defocusing component gets attenuated. Trajectory bending disappears as a one-hump structure becomes established. Eventually, defocusing term completely decays.

6.3.4 Trajectory bending in vector supermode solitons

Trajectory bending, found in all cases of vector soliton propagation, demands further investigation as an example of both momentum conservation breaking and spontaneous symmetry breaking in optical beams[235]. Walk-off is often observed in nematic LC due to optical axis misalignment [236], but it does not lead to complex behavior observed for vector nematicons.

Trajectory bending appears due to the lack of action-reaction symmetry in the system [237, 238]. If the defocusing beam has no attractive term ($A = 1$), the defocusing beam has a purely repulsive effect on the focusing beam. In effect, defocusing beam pushes the focusing beam away, while simultaneously focusing beam pulls defocusing beam in. Action-reaction symmetry breaking is additionally reinforced by the differences between nonlinear response functions $R_f \neq R_d$. This fact explains why trajectory bending appears for every value of $0 < A \leq 1$, even when $A - 1 > B$

guarantees attractive term domination in the defocusing beam. In the case of $A = 0$ focusing beam does not influence the nonlinear processes and trajectory bending does not occur.

Analytical considerations

To explore trajectory bending analytically, we derived mutual forces that beams exert on each other through nonlinear interactions. Beam interaction forces are derived by utilizing the Ehrenfest theorem [239]. We apply a generalized form of two-component equations to calculate the evolution of vector state (ψ_1, ψ_2).

$$\begin{cases} i\partial_Z\psi_1 = D_1\partial_{XX}\psi_1 + M_{11}P_1(\psi_1)\psi_1 + M_{21}P_2(\psi_2)\psi_1 \\ i\partial_Z\psi_2 = D_2\partial_{XX}\psi_2 + M_{12}P_1(\psi_1)\psi_2 + M_{22}P_2(\psi_2)\psi_2 \end{cases} \tag{6.26}$$

where $P(\psi_1, \psi_2) = P_1(\psi_1) + P_2(\psi_2)$ is a nonlinear potential, which at this stage we do not specify. We assume that initial condition for this evolution will be a stationary solution found by any relaxation method. We will derive equations of motion for the average position $\langle X\rangle_m$, where $\langle f(\psi)\rangle_m = \dfrac{\int \psi_m^* f(\psi_m)\,dx}{\int |\psi_m|^2 dx}$ is expected value of distribution f for ψ_m state component. Simple analysis leads to the set of coupled equations for first derivative

$$\begin{aligned} \partial_Z\langle X\rangle_j = \langle\partial_Z\phi_j|X|\phi_j\rangle + \langle\phi_j|X|\partial_Z\phi_j\rangle = i\left(\langle\phi_j|D_j\partial_{XX}|X\phi_j\rangle + \langle\phi_j|M_jPX|\phi_j\rangle - \right. \\ \left. -\langle\phi_j|XM_jP|\phi_j\rangle - \langle\phi_j|D_jX\partial_{XX}|\phi_j\rangle\right) = 2iD_j\langle\phi_j|\partial_X|\phi_j\rangle = 2iD_j\langle\partial_X\rangle_j \end{aligned} \tag{6.27}$$

and the second derivative

$$\begin{aligned} \partial_{ZZ}\langle X\rangle_j = 2iD_j\left(\langle\partial_Z\phi_j|\partial_X|\phi_j\rangle + \langle\phi_j|\partial_X|\partial_Z\phi_j\rangle\right) = 2D_j\left(\langle\phi_j|\partial_XD_j\partial_{XX}|\phi_j\rangle + \right. \\ \left. +\langle\phi_j|\partial_XM_j|P\phi_j\rangle - \langle\phi_j|D_j\partial_{XX}\partial_X|\phi_j\rangle - \langle\phi_j|M_jP\partial_X|\phi_j\rangle\right) = 2D_jM_j\langle\partial_XP\rangle_j \end{aligned} \tag{6.28}$$

For our specific case, we can substitute coefficients from equations (6.25) and obtain the following form

$$\begin{cases} \partial_{ZZ}\langle X\rangle_1 = a_{11}(Z) + a_{12}(Z) \\ \partial_{ZZ}\langle X\rangle_2 = a_{21}(Z) + a_{22}(Z) \end{cases} \tag{6.29}$$

where "acceleration" terms are defined explicitly by

$$\begin{cases} a_{11} = \dfrac{2}{N}\dfrac{\int |\psi_1|^2 \partial_X \left[R_f * |\psi_1|^2\right] dx}{\int |\psi_1|^2 dx} \\ a_{12} = \dfrac{-2B}{N}\dfrac{\int |\psi_1|^2 \partial_X \left[R_d * |\psi_2|^2\right] dx}{\int |\psi_1|^2 dx} \\ a_{21} = 2\dfrac{\int |\psi_2|^2 \partial_X \left[R_f * |\psi_1|^2\right] dx}{\int |\psi_2|^2 dx} \\ a_{22} = -2B\dfrac{\int |\psi_2|^2 \partial_X \left[R_d * |\psi_2|^2\right] dx}{\int |\psi_2|^2 dx}. \end{cases} \tag{6.30}$$

At the initial stage of the propagation we can assume that solutions are stationary and their width is much smaller than nonlocality range of the nonlinear potential. In this case we have $\int |\psi_m|^2 \partial_X P_k dx \approx [\partial_X P_k]_{X=\langle X\rangle_m}$ and equations (6.30) can be related to the examples known in the literature, for instance [238].

Previously we have observed trajectory bending behavior in states perturbed by random noise. Our goal is to explore and quantify this type of behavior. Instead of random noise, we introduce three possible types of state perturbation. First approach to perturbation is the shift perturbation – shifting initial beam position without changing its shape: $\psi_{m,pert}(X) = \psi_m(X - \delta_{ms})$. Second is asymmetry perturbation – it corresponds to perturbing beam shape by breaking state symmetry: $\psi_{m,pert} = \psi_m * (1 + \delta_{ma} * X)$. Third way is adding phase perturbation, corresponding to additional transverse momentum $\psi_{m,pert} = \psi_m * e^{i\delta_{mp}X}$.

To estimate perturbation influence analytically, we assume a one-peak Gaussian shape of the initial beams, similar to Eqs. 6.22, with additional perturbation terms

$$\begin{cases} \psi_1 = A_1 e^{-X^2/w_1^2} e^{i\delta_{1p}X} \left[1 + \delta_{1a} X\right] \\ \psi_2 = A_2 e^{-(X-\delta_s)^2/w_2^2} e^{i\delta_{2p}X} \left[1 + \delta_{2a}(X - \delta_s)\right] \end{cases} \tag{6.31}$$

Substitution of Eqs. 6.31 into Eqs. 6.30 leads to disappearance of self-interaction terms $a_{11} = a_{22} = 0$. Phase perturbations δ_{mp} don't affect acceleration coefficients. General formula for interaction terms is too unwieldy for practical use. We focus on two particular cases:

1. The only perturbation is asymmetry in one of the channels: $\delta_s = \delta_{2a} = 0$.

$$\begin{cases} \partial_{ZZ}\langle X\rangle_1 = \delta_{1a}\dfrac{16A_2^2 w_1^2 w_2 B}{N\left(\delta_{1a}^2 w_1^2 + 4\right)\left(2\sigma^2 + w_1^2 + w_2^2\right)^{3/2}} \\ \partial_{ZZ}\langle X\rangle_2 = \delta_{1a}\dfrac{4A_1^2 w_1^3}{\left(2 + w_1^2 + w_2^2\right)^{3/2}} \end{cases} \tag{6.32}$$

Both terms have the same sign, thus we expect self-acceleration to the right.

2. The only perturbation is shift between channels: $\delta_{1a} = \delta_{2a} = 0$.

$$\begin{cases} \partial_{ZZ}\langle X\rangle_1 = -\delta_s \dfrac{8A_2^2 w_2 e^{-\frac{2\delta_s^2}{2\sigma^2+w_1^2+w_2^2}} B}{N\left(2\sigma^2+w_1^2+w_2^2\right)^{3/2}} \\ \partial_{ZZ}\langle X\rangle_2 = -\delta_s \dfrac{8A_1^2 w_1 e^{-\frac{2\delta_s^2}{2+w_1^2+w_2^2}}}{\left(2+w_1^2+w_2^2\right)^{3/2}} \end{cases} \tag{6.33}$$

Both terms have the same sign, thus we expect self-acceleration to the left.

We can use these results to estimate acceleration ratio between two channels $a_r = \dfrac{\partial_{ZZ}\langle X\rangle_1}{\partial_{ZZ}\langle X\rangle_2}$ analytically. We expect two distinct propagation regimes for different ratios. If $0 < a_r < 1$, defocusing beam has higher acceleration, thus decreasing beam misalignment and stabilizing propagation. However, if $a_r > 1$, the focusing beam will separate from defocusing beam due to higher acceleration, thus destabilizing the soliton and leading to trajectory bending.

We can calculate the acceleration ratio for both cases in small perturbation limit $\delta \to 0$.

$$a_r = \frac{A_2^2 w_2 B}{A_1^2 w_1 N}\left(\frac{w_1^2+w_2^2+2}{w_1^2+w_2^2+2\sigma^2}\right)^{3/2} \tag{6.34}$$

Our previous simulations allow us to assume $A_1 \simeq A_2$ and $w_1 \simeq w_2$ even for supermode solitons with different wavelength ratios. This allows us to simplify a_r further.

$$a_r \simeq \frac{B}{N}\left(\frac{w^2+1}{w^2+\sigma^2}\right)^{3/2} \tag{6.35}$$

In order to achieve stable supermode solitons we require $0 < B < 1$ and $0 < \sigma < 1$. In this case maximal value a_r is achieved for $w \to 0$. This leads us to the following condition for self-accelerating trajectory bending

$$\sigma < \left(\frac{B}{N}\right)^{1/3} \tag{6.36}$$

This is the generalized form of the Eq. 6.24 – condition for the existence of the supermode solitons. We can conclude that self-accelerating trajectory bending can be observed only in supermode solitons. These results are supported by numerical calculations.

Numerical investigation

Propagation results for quasi-scalar ($K = 1$) and vector nematicons are presented in Figure (6.10). Vector solitons don't exhibit trajectory bending in absence of perturbation. Initial trajectory bending direction is in agreement with theoretical predictions. Initial trajectory bending is linearly proportional to perturbation value, also in agreement with theoretical considerations. Asymmetric perturbation leads to periodically modulated trajectory. Shift perturbation has a much stronger effect than asymmetry perturbation – even small shift drives vector soliton onto parabolic trajectory, with following soliton destruction in case of $K < 1$. Soliton destruction appears as focusing and defocusing components slowly become spatially separated. Similar behavior is observed in the case of phase perturbation.

Based on the first numerical results we propose a hypothesis – misalignment of solitons' centers is the main contributor to the trajectory bending. Several indirect observations favor this conjecture. First, if the same asymmetric or phase perturbation is introduced in both channels for $K = 1$, trajectory bending does not occur. Second, vector soliton is much more sensitive to the shift perturbation than to asymmetry perturbation, as asymmetry perturbation has minimal influence on the center position. Third, phase perturbation leads to trajectory bending contrary to the theoretical prediction. Phase perturbation can be understood as initial transverse beam velocity, creating components misalignment and leading to the same dynamics as observed for the shift perturbation.

To show that the relative shift of soliton centers and the interaction strength are correlated we present an example of beam acceleration dynamics in Figure (6.11). Acceleration coefficients based on Eqs. 6.30 are in agreement with numerical results. Self-interaction terms a_{11}, a_{22} remain negligible in all simulations. We observed a high correlation between beam acceleration and center misalignment between two components. Temporal deviations from these correlations correspond to particularly asymmetric wavefunction shapes.

Our next step was to analyze the influence of other parameters, such as B and σ on trajectory bending. Smaller σ leads to states with a larger number of peaks. Supermode solutions for smaller σ are less stable – they have a stronger response to perturbations and a bigger risk of collapse. Perturbation of one-peak solutions doesn't lead to growing trajectory bending, in agreement with theoretical predictions. Results are shown in Figure (6.12). Qualitatively, the same behaviors are observed for every type of perturbation independent from B and σ, as long as supermode states have the same structure.

To investigate the influence of wavelength ratio further, we explored its influence on diffractive and nonlinear terms separately. In the general model, such an effect can be achieved by changing the linear refractive index ratio. Results are presented in Figure (6.13). The strongest influence on trajectory bending behavior appears due

to the diffractive term – the difference in diffraction between components drastically destabilizes soliton propagation. Alignment of refractive index ratio to compensate propagation constant change can drastically increase vector supermode stability.

Conclusion

In conclusion, we investigated vector supermode solitons numerically and analytically. Coupling between two components immensely influences soliton propagation dynamics, even in the case of pseudo-scalar propagation. Action-reaction symmetry breaking leads to instability type unique for vector solitons – trajectory bending. Trajectory instability is mainly controlled by soliton center mismatch and can be regulated by adjusting material dispersion.

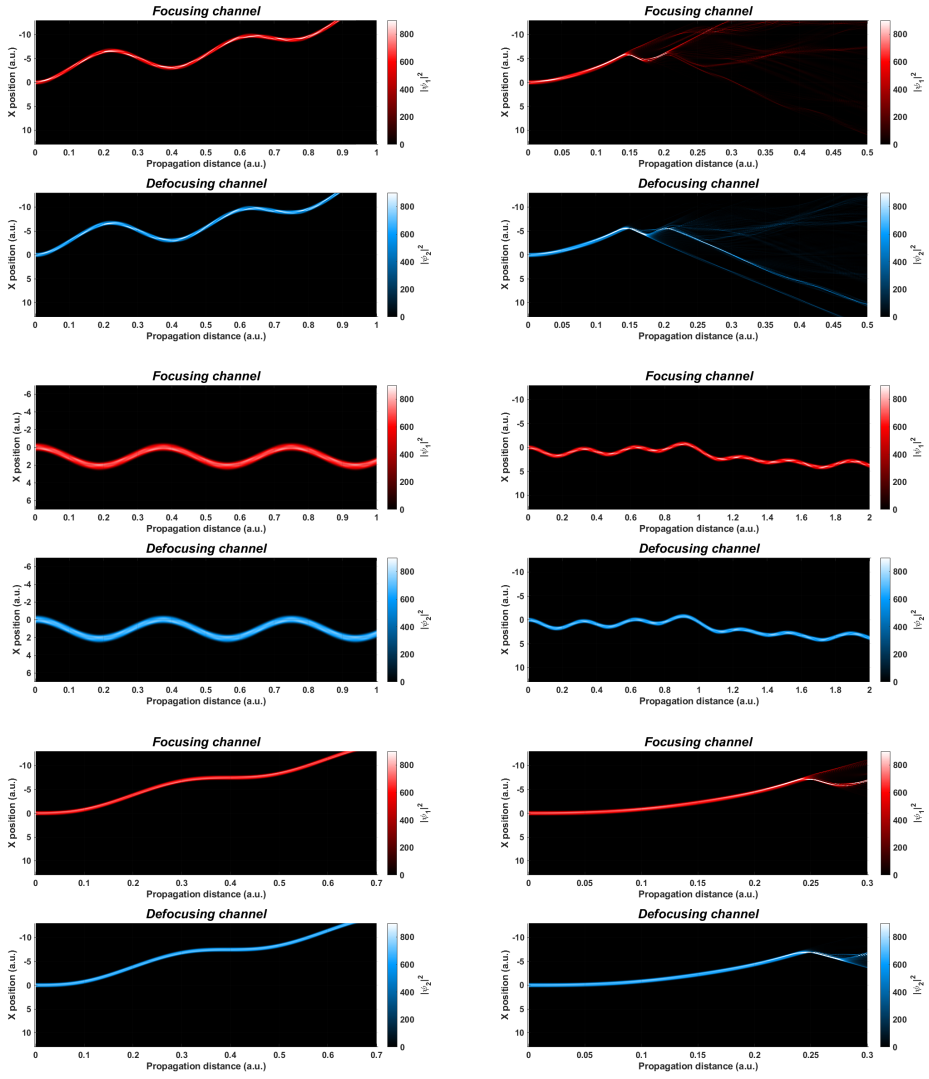

FIGURE 6.10: Trajectory bending with controlled perturbation for $K = 1$ (left) and $K = 0.9$ (right). Top row – propagation with shift perturbation $\delta_{2s} = 0.003$. Middle row – propagation with asymmetry perturbation $\delta_{1a} = 0.1$. Bottom row – propagation with phase perturbation $\delta_{1p} = 0.1$. All simulations performed with initial parameters $B = 0.5, \sigma = 0.75$.

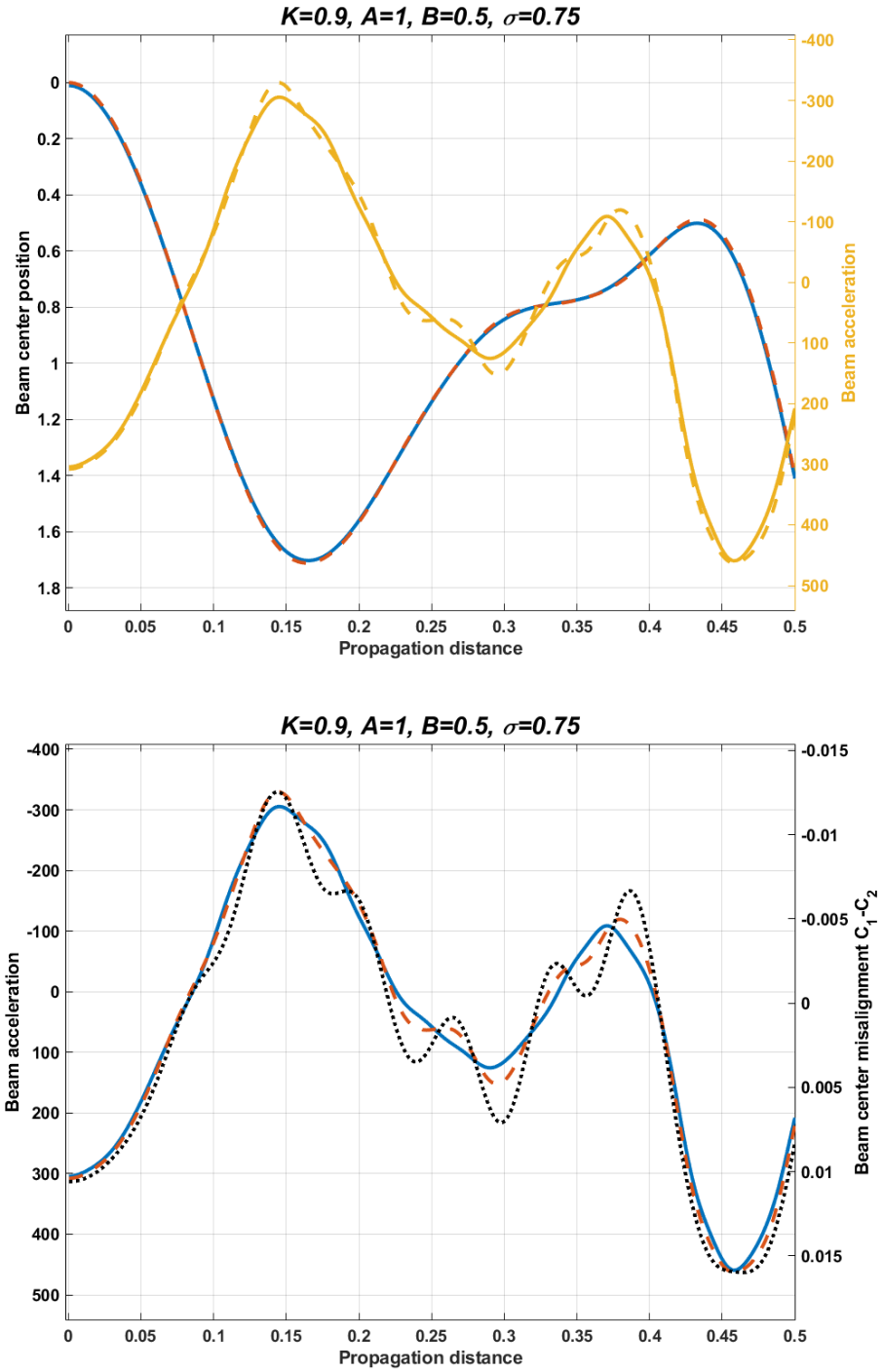

FIGURE 6.11: Top – soliton center position and acceleration (yellow) for focusing (solid) and defocusing (dashed) component. Bottom – soliton acceleration and beam center misalignment $\langle X\rangle_1 - \langle X\rangle_2$ (black dotted curve). Initial parameters: $K = 0.9, B = 0.5, \sigma = 0.75, \delta_{1a} = 0.2$.

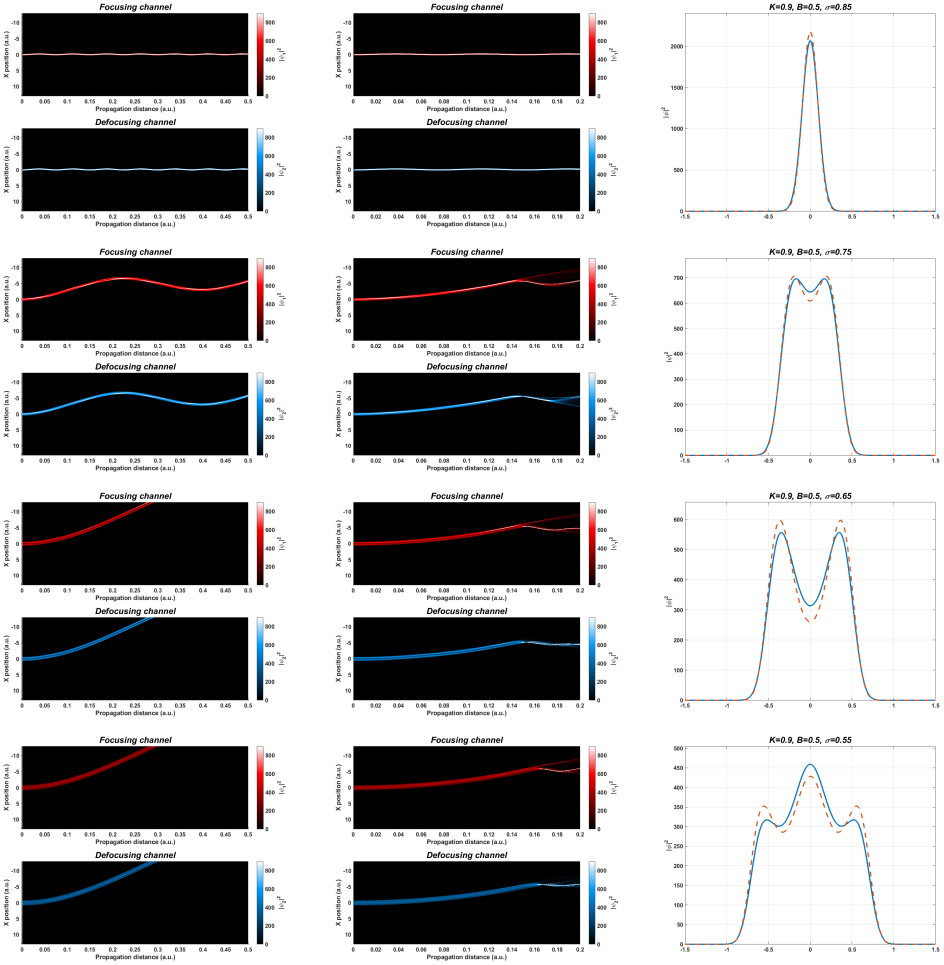

FIGURE 6.12: Trajectory bending of different initial supermode states for $K = 1$ (left column) and $K = 0.9$ (middle column). Right column presents initial state distribution for $K = 0.9$. All calculations were performed for $B = 0.5$ using shift perturbation $\Delta_{2,shift} = 0.003$. Each row corresponds to different value of nonlocality ratio. Top to bottom – $\sigma = 0.85; \sigma = 0.75; \sigma = 0.65; \sigma = 0.55$.

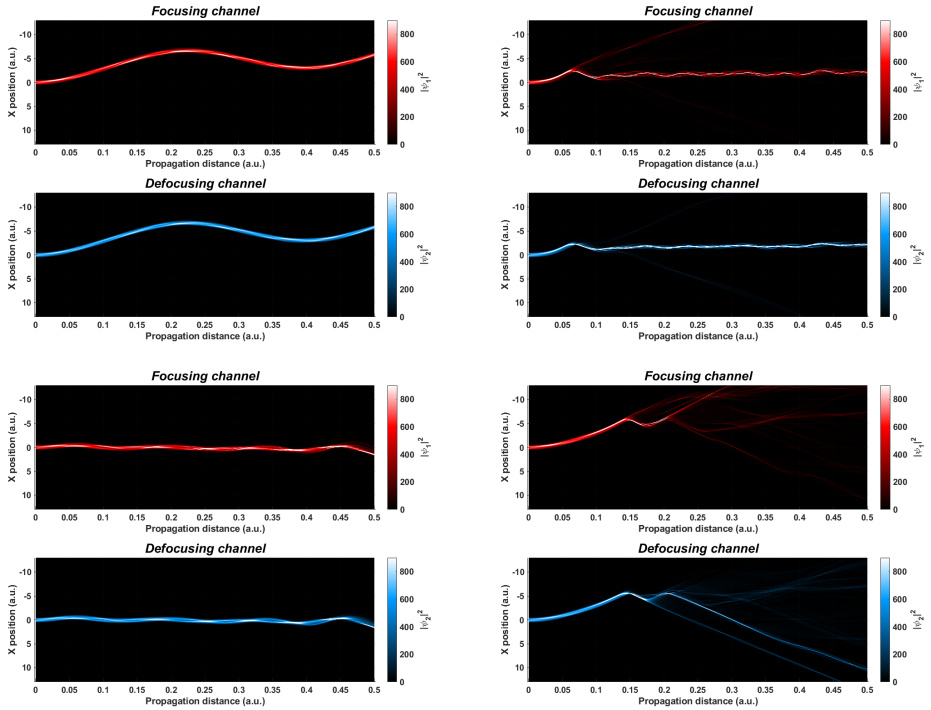

FIGURE 6.13: Perturbed soliton propagation for $B = 0.5, \sigma = 0.75, \Delta_{2,shift} = 0.003$ including different terms of coupled structure influence. Top left – pseudo-scalar case ($N = 1, K = 1$). Top right – two components with different diffractive terms and equal nonlinear terms ($N = 0.9, K = 1$). Bottom left – two components with equal diffractive terms and different nonlinear terms ($N = 1.11, K = 0.9$). Bottom right – two components with different diffractive and nonlinear terms ($N = 1, K = 0.9$).

Chapter 7

Conclusions

During the creation of this thesis, my goal was to provide a brief introduction to state-of-the-art research of coupled nonlinear systems. Interaction of multiple nonlinear components leads to interesting state dynamics even in the case of simple models. The introduction of interaction with propagation medium, both through nonlocal interactions and external energy flow, creates vector states that are highly sensitive to the surrounding conditions.

Our exploration of the coupled nonlinear rings with saturable gain shows a rich family of possible propagation states. Precise coupling control creates inhomogeneous, oscillating, or chaotic states, or even control system topological charge through precise vortex creation.

Our research on nonlocal coupled models with competing nonlinearities leads us to the whole family of vector supermode solitons. The introduction of the interacting components leads to trajectory bending instability. This process, possible only in coupled nonlinear systems, is strongly correlated with soliton components' spatial mismatch and can be corrected through specific material dispersion matching.

Appendix A

Derivation of conservation laws in coupled NLSE

The initial system of two coupled NLSE ($m = 1, 2$) takes the following form.

$$i\partial_t \psi_m = d_m \partial_{xx} \psi_m + \gamma_m \psi_m + \Gamma_m |\psi_m|^2 \psi_m + \\ + \kappa_m \psi_{3-m} + C_m |\psi_{3-m}|^2 \psi_m + K_m \psi_{3-m}^2 \psi_m^* \quad \text{(A.1)}$$

Generally, $d, \gamma, \Gamma, \kappa, K, C$ are complex, time-independent functions of x. For simplicity of derivation, we shall assume that d is constant. This assumption is true if $d\partial_{xx}\psi$ term represents diffraction. In optical pulse framework, d corresponds to material dispersion and is not constant. Conservation laws derived below still apply, even though they require more tedious calculations. In this case dispersion term is expanded through Taylor series in Fourier space [47]: $d(x)\partial_{xx}\psi = d_0\partial_{xx}\psi + d_1\partial_{xxx}\psi + d_2\partial_{xxxx}\psi + ...$

In order to derive conservation of total norm $N = \int_{-\infty}^{\infty} |\psi_1|^2 + |\psi_2|^2 dx$, we calculate $[Eq.A.1]_m \psi_m^* - [Eq.A.1]_m^* \psi_m$

$$i\left(\psi_m^* \partial_t \psi_m + \psi_m \partial_t \psi_m^*\right) = d_m \psi_m^* \partial_{xx} \psi_m - d_m^* \psi_m \partial_{xx} \psi_m^* + \left(\gamma_m - \gamma_m^*\right) |\psi_m|^2 + \\ + \left(\Gamma_m - \Gamma_m^*\right) |\psi_m|^4 + \left(\kappa_m \psi_m^* \psi_{3-m} - \kappa_m^* \psi_m \psi_{3-m}^*\right) + \\ + \left(C_m - C_m^*\right) |\psi_{3-m}|^2 |\psi_m|^2 + \left(K_m \left[\psi_m^* \psi_{3-m}\right]^2 - K_m^* \left[\psi_m \psi_{3-m}^*\right]^2\right) \quad \text{(A.2)}$$

Conservation of norm demands $d_m = d_m^*, \gamma_m = \gamma_m^*, \Gamma_m = \Gamma_m^*, \kappa_m = \kappa_m^*, C_m = C_m^*, K_m = K_m^*$. Essentially this conditions are the same as the assumption of hermitian evolution. After simplification and integration over space, we get following relation

$$i\partial_t \int_{-\infty}^{\infty} |\psi_m|^2 dx = -d_m \left[\psi_m^* \partial_x \psi_m - \psi_m \partial_x \psi_m^*\right]_{-\infty}^{\infty} + \\ + \int_{-\infty}^{\infty} \kappa_m \left(\psi_m^* \psi_{3-m} - \psi_m \psi_{3-m}^*\right) + K_m \left(\left[\psi_m^* \psi_{3-m}\right]^2 - \left[\psi_m \psi_{3-m}^*\right]^2\right) dx \quad \text{(A.3)}$$

Norm can be defined only in case of localized states, thus $\psi_m|_{-\infty} = \psi_m|_{\infty} = 0$. In this case, change of the single channel norm depends on total current between channels

$$\partial_t \int_{-\infty}^{\infty} |\psi_1|^2 dx = J_\perp = -i \int_{-\infty}^{\infty} \kappa_1 \left(\psi_1^* \psi_2 - \psi_2^* \psi_1\right) + K_1 \left(\left[\psi_1^* \psi_2\right]^2 - \left[\psi_2^* \psi_1\right]^2\right) dx \quad \text{(A.4)}$$

The last assumption for norm conservation is equivalence of action and reaction between two channels: $\kappa_1 = \kappa_2, K_1 = K_2$. In this case $\partial_t \int_{-\infty}^{\infty} |\psi_2|^2 dx = -J_\perp$, thus total norm is conserved. Action-reaction equivalence also assumes $C_1 = C_2$. This assumption does not influence norm, however it will become important for momentum and energy conservation.

Definition of energy depends on particular physical system. We find it by calculating $\sum_m [Eq.A.1]\partial_t \psi_m^* + [Eq.A.1]_m^* \partial_t \psi_m$

$$i(\partial_t \psi_m^*)(\partial_t \psi_m) - i(\partial_t \psi_m)(\partial_t \psi_m^*) = d_m^*(\partial_t \psi_m)(\partial_{xx} \psi_m^*) + d_m(\partial_t \psi_m^*)(\partial_{xx} \psi_m) + \\ + \gamma_m \psi_m \partial_t \psi_m^* + \gamma_m^* \psi_m^* \partial_t \psi_m + |\psi_m|^2 \left(\Gamma_m \psi_m \partial_t \psi_m^* + \Gamma_m^* \psi_m^* \partial_t \psi_m\right) + \\ + \kappa_m \psi_{3-m} \partial_t \psi_m^* + \kappa_m^* \psi_{3-m}^* \partial_t \psi_m + \left(C_m \psi_m \partial_t \psi_m^* + C_m^* \psi_m^* \partial_t \psi_m\right) + \\ + \left(K_m \psi_{3-m}^2 \psi_m^* \partial_t \psi_m^* + K_m^* [\psi_{3-m}^*]^2 \psi_m \partial_t \psi_m\right) \quad \text{(A.5)}$$

We can simplify this formula by using previous assumptions: hermiticity, action-reaction equivalence, and localized solutions.

$$0 = d_m \partial_x \left((\partial_t \psi_m^*)(\partial_x \psi_m) + (\partial_x \psi_m^*)(\partial_t \psi_m)\right) - d_m \partial_t |\partial_x \psi_m|^2 + \gamma_m \partial_t |\psi_m|^2 + \\ + \frac{\Gamma_m}{2} \partial_t |\psi_m|^4 + \kappa_m \left(\psi_{3-m} \partial_t \psi_m^* + \psi_{3-m}^* \partial_t \psi_m\right) + \\ + C_m |\psi_{3-m}|^2 \partial_t |\psi_m|^2 + \frac{K_m}{2} \left(\psi_{3-m}^2 \partial_t [\psi_m^*]^2 + [\psi_{3-m}^*]^2 \partial_t \psi_m^2\right) \quad \text{(A.6)}$$

Integration over space coordinate gives us the final definition of energy.

$$E = \int_{-\infty}^{\infty} \Big[-d_1|\partial_x\psi_1|^2 - d_2|\partial_x\psi_2|^2 + \gamma_1|\psi_1|^2 + \gamma_2|\psi_2|^2 + \\ + \frac{\Gamma_1}{2}|\psi_1|^4 + \frac{\Gamma_2}{2}|\psi_2|^4 + \kappa\left(\psi_1\psi_2^* + \psi_1^*\psi_2\right) + \\ + C|\psi_1|^2|\psi_2|^2 + \frac{K}{2}\left([\psi_1\psi_2^*]^2 + [\psi_1^*\psi_2]^2\right)\Big] dx = \text{const} \quad \text{(A.7)}$$

Momentum is defined as a total current inside a single channel:

$$M_m = \int_{-\infty}^{\infty} j_m = \int_{-\infty}^{\infty} \frac{\psi_m^*\partial_x\psi_m - \psi_m\partial_x\psi_m^*}{i} dx \quad \text{(A.8)}$$

To show conservation of momentum, we need to simplify $\sum_m [Eq.A.1]_m \partial_x\psi_m^* + [Eq.A.1]_m^* \partial_x\psi_m - \psi_m^*\partial_x[Eq.A.1]_m - \psi_m\partial_x[Eq.A.1]_m^*$. As previously, we assume hermiticity of all components, action-reaction symmetry and localized solutions.

$$\partial_t M_m = \Big[-d_m\left(\psi_m\partial_{xx}\psi_m^* + \psi_m^*\partial_{xx}\psi_m - 2|\partial_x\psi_m|^2\right) - \\ - \Gamma_m|\psi_m|^4 - K_m\left([\psi_1^*\psi_2]^2 + [\psi_1\psi_2^*]^2\right)\Big]_{-\infty}^{\infty} - \\ - 2|\psi_m|^2\partial_x\gamma_m - |\psi_m|^4\partial_x\Gamma_m + 2\kappa_m\left(\psi_{3-m}\partial_x\psi_m^* + \psi_{3-m}^*\partial_x\psi_m\right) - \\ - 2C_m|\psi_m|^2\partial_x|\psi_{3-m}|^2 - \left([\psi_1^*\psi_2]^2 + [\psi_1\psi_2^*]^2\right)\partial_x K_m \quad \text{(A.9)}$$

We can combine both terms to calculate the total momentum.

$$\partial_t M = -2\left(|\psi_1|^2\partial_x\gamma_1 + |\psi_2|^2\partial_x\gamma_2\right) - \left(|\psi_1|^4\partial_x\Gamma_1 + |\psi_2|^4\partial_x\Gamma_2\right) - \\ - 2\left(\psi_1^*\psi_2 + \psi_2^*\psi_1\right)\partial_x\kappa - 2|\psi_1|^2|\psi_2|^2\partial_x C - 2\left([\psi_1^*\psi_2]^2 + [\psi_1\psi_2^*]^2\right)\partial_x K \quad \text{(A.10)}$$

As we can see, conservation of total momentum additionally demands that all coupling and potential terms do not depend on x.

Appendix B

Newton Conjugate Gradient method in coupled NLSE

Previously, we formulated this form of coupled NLSE

$$\begin{cases} i\partial_t\psi_1 = d_1\partial_{xx}\psi_1 + \gamma_1\psi_1 + \Gamma_1|\psi_1|^2\psi_1 + \kappa_1\psi_2 + C_1|\psi_2|^2\psi_1 + K_1\psi_2^2\psi_1^* \\ i\partial_t\psi_2 = d_2\partial_{xx}\psi_2 + \gamma_2\psi_2 + \Gamma_2|\psi_2|^2\psi_2 + \kappa_2\psi_1 + C_2|\psi_1|^2\psi_2 + K_2\psi_1^2\psi_2^* \end{cases} \tag{B.1}$$

We assume existence of states with constant phase velocity: $\psi_m(x,t) = \psi_m(x)e^{i\mu_m t}$. First, we substitute phase velocity and separate real and imaginary values: $\psi_m(x) = R_m + iG_m$.

$$\begin{cases} -\mu_1 R_1 = d_1\partial_{xx}R_1 + \gamma_1 R_1 + \Gamma_1\left(R_1^2+G_1^2\right)R_1 + \kappa_1 R_2 + \\ \quad + C_1\left(R_2^2+G_2^2\right)R_1 + K_1\left(R_1R_2^2 + 2R_2G_1G_2 - R_1G_2^2\right) \\ -\mu_1 G_1 = d_1\partial_{xx}G_1 + \gamma_1 G_1 + \Gamma_1\left(R_1^2+G_1^2\right)G_1 + \kappa_1 G_2 + \\ \quad + C_1\left(R_2^2+G_2^2\right)G_1 + K_1\left(G_1G_2^2 + 2G_2R_1R_2 - G_1R_2^2\right) \\ -\mu_2 R_2 = d_2\partial_{xx}R_2 + \gamma_2 R_2 + \Gamma_1\left(R_2^2+G_2^2\right)R_2 + \kappa_2 R_1 + \\ \quad + C_2\left(R_1^2+G_1^2\right)R_2 + K_2\left(R_2R_1^2 + 2R_1G_1G_2 - R_2G_1^2\right) \\ -\mu_2 G_2 = d_2\partial_{xx}G_2 + \gamma_2 G_2 + \Gamma_1\left(R_2^2+G_2^2\right)G_2 + \kappa_2 G_1 + \\ \quad + C_2\left(R_1^2+G_1^2\right)G_2 + K_2\left(G_2G_1^2 + 2G_1R_1R_2 - G_2R_1^2\right) \end{cases} \tag{B.2}$$

In the next step we express each term as sum of initial guess and error correction: $R_m = R_{m,n} + r_{m,n}, G_m = G_{m,n} + g_{m,n}$, where $r, j \ll 1$. Tedious, but straightforward simplification leads us to the following equations.

$$
\begin{cases}
\left(\mu_1+\gamma_1+d_1\partial_{xx}\right)\left(R_{1,n}+r_{1,n}\right)+\Gamma_1\left[\left(R_{1,n}^2+G_{1,n}^2\right)R_{1,n}+\left(3R_{1,n}^2+G_{1,n}^2\right)r_{1,n}+\right.\\
\quad\left.+2R_{1,n}G_{1,n}g_{1,n}\right]+\kappa_1\left(R_{2,n}+r_{2,n}\right)+C_1\left[\left(R_{2,n}^2+G_{2,n}^2\right)R_{1,n}+\right.\\
\quad\left.+\left(R_{2,n}^2+G_{2,n}^2\right)r_{1,n}+2R_{1,n}\left(R_{2,n}r_{2,n}+G_{2,n}g_{2,n}\right)\right]+\\
\quad+C_1\left[R_{2,n}^2\left(R_{1,n}+r_{1,n}\right)+2r_{2,n}R_{1,n}R_{2,n}+2G_{1,n}G_{2,n}\left(R_{1,n}+r_{1,n}\right)+\right.\\
\quad\left.+2R_{2,n}\left(g_{1,n}G_{2,n}+G_{1,n}g_{2,n}\right)-R_{2,n}^2\left(R_{1,n}+r_{1,n}\right)-2g_{2,n}R_{1,n}G_{2,n}\right]=\mathcal{O}(a^2)\\
\left(\mu_1+\gamma_1+d_1\partial_{xx}\right)\left(G_{1n}+g_{1,n}\right)+\Gamma_1\left[\left(R_{1,n}^2+G_{1,n}^2\right)G_{1,n}+\left(R_{1,n}^2+3G_{1,n}^2\right)g_{1,n}+\right.\\
\quad\left.+2R_{1,n}G_{1,n}r_{1,n}\right]+\kappa_1\left(G_{2,n}+g_{2,n}\right)+C_1\left[\left(R_{2,n}^2+G_{2,n}^2\right)G_{1,n}+\right.\\
\quad\left.+\left(R_{2,n}^2+G_{2,n}^2\right)g_{1,n}+2G_{1,n}\left(R_{2,n}r_{2,n}+G_{2,n}g_{2,n}\right)\right]+\\
\quad+C_1\left[G_{2,n}^2\left(G_{1,n}+g_{1,n}\right)+2g_{2,n}G_{1,n}G_{2,n}+2R_{1,n}R_{2,n}\left(G_{1,n}+g_{1,n}\right)+\right.\\
\quad\left.+2G_{2,n}\left(r_{1,n}R_{2,n}+R_{1,n}r_{2,n}\right)-G_{2,n}^2\left(G_{1,n}+g_{1,n}\right)-2r_{2,n}G_{1,n}R_{2,n}\right]=\mathcal{O}(a^2)\\
\left(\mu_2+\gamma_2+d_2\partial_{xx}\right)\left(R_{2,n}+r_{2,n}\right)+\Gamma_2\left[\left(R_{2,n}^2+G_{2,n}^2\right)R_{2,n}+\left(3R_{2,n}^2+G_{2,n}^2\right)r_{2,n}+\right.\\
\quad\left.+2R_{2,n}G_{2,n}g_{2,n}\right]+\kappa_2\left(R_{1,n}+r_{1,n}\right)+C_2\left[\left(R_{1,n}^2+G_{1,n}^2\right)R_{2,n}+\right.\\
\quad\left.+\left(R_{1,n}^2+G_{1,n}^2\right)r_{2,n}+2R_{2,n}\left(R_{1,n}r_{1,n}+G_{1,n}g_{1,n}\right)\right]+\\
\quad+C_2\left[R_{1,n}^2\left(R_{2,n}+r_{2,n}\right)+2r_{1,n}R_{1,n}R_{2,n}+2G_{1,n}G_{2,n}\left(R_{2,n}+r_{2,n}\right)+\right.\\
\quad\left.+2R_{1,n}\left(g_{1,n}G_{2,n}+G_{1,n}g_{2,n}\right)-R_{1,n}^2\left(R_{2,n}+r_{2,n}\right)-2g_{1,n}R_{2,n}G_{1,n}\right]=\mathcal{O}(a^2)\\
\left(\mu_2+\gamma_2+d_2\partial_{xx}\right)\left(G_{2,n}+g_{2,n}\right)+\Gamma_2\left[\left(R_{2,n}^2+G_{2,n}^2\right)G_{2,n}+\left(R_{2,n}^2+3G_{2,n}^2\right)g_{2,n}+\right.\\
\quad\left.+2R_{2,n}G_{2,n}r_{2,n}\right]+\kappa_2\left(G_{1,n}+g_{1,n}\right)+C_2\left[\left(R_{1,n}^2+G_{1,n}^2\right)G_{2,n}+\right.\\
\quad\left.+\left(R_{1,n}^2+G_{1,n}^2\right)g_{2,n}+2G_{2,n}\left(R_{1,n}r_{1,n}+G_{1,n}g_{1,n}\right)\right]+\\
\quad+C_2\left[G_{1,n}^2\left(G_{2,n}+g_{2,n}\right)+2g_{1,n}G_{1,n}G_{2,n}+2R_{1,n}R_{2,n}\left(G_{2,n}+g_{2,n}\right)+\right.\\
\quad\left.+2G_{1,n}\left(r_{1,n}R_{2,n}+R_{1,n}r_{2,n}\right)-G_{1,n}^2\left(G_{2,n}+g_{2,n}\right)-2r_{1,n}G_{2,n}R_{1,n}\right]=\mathcal{O}(a^2)
\end{cases}
\tag{B.3}
$$

We generate a matrix equation for Newton iteration by neglecting higher orders of error.

$$
L_1u=L_0U \tag{B.4}
$$

where $u=\begin{bmatrix} r_{1,n}\\ g_{1,n}\\ r_{2,n}\\ g_{2,n}\end{bmatrix}$ is correction vector, added in each iteration step: $\psi_{(k,n+1)}=\psi_{(k,n)}+r_{(k,n)}+i*g_{(k,n)}$;

$$
L_1 u = \begin{bmatrix}
\left[\mu_1+\gamma_1+d_1\partial_{xx}+\left(3R_{1,n}^2+G_{1,n}^2\right)\Gamma_1+\left(R_{2,n}^2+G_{2,n}^2\right)C_1+\right. \\
\left.+\left(R_{2,n}^2-G_{2,n}^2\right)K_1\right]r_{1,n}+2\left(\Gamma_1 R_{1,n}G_{1,n}+K_1R_{2,n}G_{2,n}\right)g_{1,n}+ \\
+\left(\kappa_1+2\left(C_1+K_1\right)R_{1,n}R_{2,n}+2K_1G_{1,n}G_{2,n}\right)r_{2,n}+ \\
+2\left[\left(C_1-K_1\right)R_{1,n}G_{2,n}+K_1R_{2,n}G_{1,n}\right]g_{2,n} \\
\\
\left[\mu_1+\gamma_1+d_1\partial_{xx}+\left(R_{1,n}^2+3G_{1,n}^2\right)\Gamma_1+\left(R_{2,n}^2+G_{2,n}^2\right)C_1+\right. \\
\left.+\left(G_{2,n}^2-R_{2,n}^2\right)K_1\right]g_{1,n}+2\left(\Gamma_1 R_{1,n}G_{1,n}+K_1R_{2,n}G_{2,n}\right)r_{1,n}+ \\
+\left(\kappa_1+2\left(C_1+K_1\right)G_{1,n}G_{2,n}+2K_1R_{1,n}R_{2,n}\right)g_{2,n}+ \\
+2\left[\left(C_1-K_1\right)G_{1,n}R_{2,n}+K_1G_{2,n}R_{1,n}\right]r_{2,n} \\
\\
\left[\mu_2+\gamma_2+d_2\partial_{xx}+\left(3R_{2,n}^2+G_{2,n}^2\right)\Gamma_2+\left(R_{1,n}^2+G_{1,n}^2\right)C_2+\right. \\
\left.+\left(R_{1,n}^2-G_{1,n}^2\right)K_2\right]r_{2,n}+2\left(\Gamma_2 R_{2,n}G_{2,n}+K_2R_{1,n}G_{1,n}\right)g_{2,n}+ \\
+\left(\kappa_2+2\left(C_2+K_2\right)R_{1,n}R_{2,n}+2K_2G_{1,n}G_{2,n}\right)r_{1,n}+ \\
+2\left[\left(C_2-K_2\right)R_{2,n}G_{1,n}+K_2R_{1,n}G_{2,n}\right]g_{1,n} \\
\\
\left[\mu_2+\gamma_2+d_2\partial_{xx}+\left(R_{2,n}^2+3G_{2,n}^2\right)\Gamma_2+\left(R_{1,n}^2+G_{1,n}^2\right)C_2+\right. \\
\left.+\left(G_{1,n}^2-R_{1,n}^2\right)K_2\right]g_{2,n}+2\left(\Gamma_2 R_{2,n}G_{2,n}+K_2R_{1,n}G_{1,n}\right)r_{2,n}+ \\
+\left(\kappa_2+2\left(C_2+K_2\right)G_{1,n}G_{2,n}+2K_2R_{1,n}R_{2,n}\right)g_{1,n}+ \\
+2\left[\left(C_2-K_2\right)G_{2,n}R_{1,n}+K_2G_{1,n}R_{2,n}\right]r_{1,n}
\end{bmatrix} \tag{B.5}
$$

and

$$
L_0 U = -\begin{bmatrix}
\left(\mu_1+\gamma_1+d_1\partial_{xx}+\left(R_{1,n}^2+G_{1,n}^2\right)\Gamma_1+\left(R_{2,n}^2+G_{2,n}^2\right)C_1\right)R_{1,n}+ \\
+\kappa_1 R_{2,n}+C_1\left(R_{1,n}R_{2,n}^2+2R_{2,n}G_{1,n}G_{2,n}-R_{1,n}G_{2,n}^2\right) \\
\\
\left(\mu_1+\gamma_1+d_1\partial_{xx}+\left(R_{1,n}^2+G_{1,n}^2\right)\Gamma_1+\left(R_{2,n}^2+G_{2,n}^2\right)C_1\right)G_{1,n}+ \\
+\kappa_1 G_{2,n}+C_1\left(G_{1,n}G_{2,n}^2+2G_{2,n}R_{1,n}R_{2,n}-G_{1,n}R_{2,n}^2\right) \\
\\
\left(\mu_2+\gamma_2+d_2\partial_{xx}+\left(R_{2,n}^2+G_{2,n}^2\right)\Gamma_2+\left(R_{1,n}^2+G_{1,n}^2\right)C_2\right)R_{2,n}+ \\
+\kappa_2 R_{1,n}+C_2\left(R_{2,n}R_{1,n}^2+2R_{1,n}G_{1,n}G_{2,n}-R_{2,n}G_{1,n}^2\right) \\
\\
\left(\mu_2+\gamma_2+d_2\partial_{xx}+\left(R_{2,n}^2+G_{2,n}^2\right)\Gamma_2+\left(R_{1,n}^2+G_{1,n}^2\right)C_2\right)G_{2,n}+ \\
+\kappa_2 G_{1,n}+C_2\left(G_{2,n}G_{1,n}^2+2G_{1,n}R_{1,n}R_{2,n}-G_{2,n}R_{1,n}^2\right)
\end{bmatrix} \tag{B.6}
$$

Error terms are found using conjugate gradient method:

$$u_0 = 0 \tag{B.7}$$
$$Z_0 = L_0 U \tag{B.8}$$
$$D_0 = M^{-1} Z_0 \tag{B.9}$$
$$\alpha_i = \frac{\langle Z_i | M^{-1} Z_i \rangle}{\langle D_i | L_1 D_i \rangle} \tag{B.10}$$
$$u_{i+1} = u_i + \alpha_i D_i \tag{B.11}$$
$$Z_{i+1} = Z_i - \alpha_i L_1 D_i \tag{B.12}$$
$$\beta_{i+1} = \frac{\langle Z_{i+1} | M^{-1} Z_{i+1} \rangle}{\langle Z_i | M^{-1} Z_i \rangle} \tag{B.13}$$
$$D_{i+1} = M^{-1} Z_{i+1} + \beta_{i+1} D_i \tag{B.14}$$

where $M = \begin{bmatrix} \mu_1 - d_1 \partial_{xx} & & & \\ & \mu_1 - d_1 \partial_{xx} & & \\ & & \mu_2 - d_2 \partial_{xx} & \\ & & & \mu_2 - d_2 \partial_{xx} \end{bmatrix}$ is preconditioning operator. Stopping criterion is determined by residue norm.

$$\frac{\langle Z_i | M^{-1} Z_i \rangle}{\langle Z_0 | M^{-1} Z_0 \rangle} < \epsilon \tag{B.15}$$

Note that L_1 operator must be hermitian and symmetrical ($\kappa_1 = \kappa_2, K_1 = K_2, C_1 = C_2$). These conditions are identical with conditions for energy conservation. If initial operator L_1 is symmetrical but not hermitian, equation can be adjointed through constructing hermitian operator $L_1^\dagger L_1$ [143]. Newton iteration formula for non-hermitian symmetric systems takes following form.

$$L_1^\dagger L_1 u = L_1^\dagger L_0 U \tag{B.16}$$

Bibliography

[1] Richard H Enns. *It's a nonlinear world*. Springer Science and Business Media, 2010.

[2] John Scott Russell. *Report on Waves: Made to the Meetings of the British Association in 1842-43*. 1845.

[3] Carlo Cercignani. "The boltzmann equation". In: *The Boltzmann equation and its applications*. Springer, 1988, pp. 40–103.

[4] Henri Poincaré. "Sur le problème des trois corps et les équations de la dynamique". In: *Acta mathematica* 13.1 (1890), A3–A270.

[5] Diederik Johannes Korteweg and Gustav De Vries. "XLI. On the change of form of long waves advancing in a rectangular canal, and on a new type of long stationary waves". In: *The London, Edinburgh, and Dublin Philosophical Magazine and Journal of Science* 39.240 (1895), pp. 422–443.

[6] Max Born and Leopold Infeld. "Foundations of the new field theory". In: *Proceedings of the Royal Society of London. Series A, Containing Papers of a Mathematical and Physical Character* 144.852 (1934), pp. 425–451.

[7] Balth Van der Pol. "LXXXVIII. On "relaxation-oscillations"". In: *The London, Edinburgh, and Dublin Philosophical Magazine and Journal of Science* 2.11 (1926), pp. 978–992.

[8] Albert Einstein. "Die grundlage der allgemeinen relativitätstheorie". In: *Das Relativitätsprinzip*. Springer, 1923, pp. 81–124.

[9] Lui Lam. *Introduction to nonlinear physics*. Springer Science and Business Media, 2003.

[10] Robert C Hilborn et al. *Chaos and nonlinear dynamics: an introduction for scientists and engineers*. Oxford University Press on Demand, 2000.

[11] Sarbarish Chakravarty and Yuji Kodama. "Construction of KP solitons from wave patterns". In: *Journal of Physics A: Mathematical and Theoretical* 47.2 (2013), p. 025201.

[12] Peter L Christiansen, Mads Peter Sorensen, and AC Scott. *Nonlinear Science at the Dawn of the 21st Century*. Vol. 542. Springer Science and Business Media, 2000.

[13] Douglas L Mills. *Nonlinear optics: basic concepts*. Springer Science and Business Media, 2012.

[14] Maria Göppert-Mayer. "Über elementarakte mit zwei quantensprüngen". In: *Annalen der Physik* 401.3 (1931), pp. 273–294.

[15] Fritz Sauter. "Über das Verhalten eines Elektrons im homogenen elektrischen Feld nach der relativistischen Theorie Diracs". In: *Zeitschrift für Physik* 69.11 (1931), pp. 742–764.

[16] Gilbert N Lewis, David Lipkin, and Theodore T Magel. "Reversible photochemical processes in rigid media. A study of the phosphorescent state". In: *Journal of the American Chemical Society* 63.11 (1941), pp. 3005–3018.

[17] Theodore H Maiman et al. "Stimulated optical radiation in ruby". In: (1960).

[18] PA Franken et al. "Generation of optical harmonics". In: *Physical Review Letters* 7.4 (1961), p. 118.

[19] B Ershov et al. "Two-photon absorption in CaF 2: H 0 3+". In: *IEEE Journal of Quantum Electronics* 2.4 (1966), pp. 108–108.

[20] Nicolaas Bloembergen. *Encounters In Nonlinear Optics: Selected Papers of Nicolaas Bloembergen (With Commentary)*. World Scientific, 1996.

[21] Akira Hasegawa. "Soliton-based optical communications: An overview". In: *IEEE Journal of Selected Topics in Quantum Electronics* 6.6 (2000), pp. 1161–1172.

[22] Robert W Boyd. *Nonlinear optics*. Academic press, 2019.

[23] G Lenz, Pierre Meystre, and Ewan M Wright. "Nonlinear atom optics". In: *Physical review letters* 71.20 (1993), p. 3271.

[24] Louis De Broglie. "Waves and quanta". In: *Nature* 112.2815 (1923), pp. 540–540.

[25] Otto Stern. "Beugung von Molekularstrahlen am Gitter einer Krystallspaltfläche". In: *Naturwissenschaften* 17.21 (1929), pp. 391–391.

[26] Lu Deng et al. "Four-wave mixing with matter waves". In: *Nature* 398.6724 (1999), pp. 218–220.

[27] Yuen-Ron Shen. *The principles of nonlinear optics*. 1984.

[28] Ljudvig D Faddeev and Vladimir E Korepin. "Quantum theory of solitons". In: *Physics Reports* 42.1 (1978), pp. 1–87.

[29] Iwo Bialynicki-Birula and Jerzy Mycielski. "Nonlinear wave mechanics". In: *Annals of Physics* 100.1-2 (1976), pp. 62–93.

[30] Andrei D Polyanin and Valentin F Zaitsev. *Handbook of Nonlinear Partial Differential Equations: Exact Solutions, Methods, and Problems*. Chapman and Hall/CRC, 2003.

[31] Thomas Brabec and Ferenc Krausz. "Intense few-cycle laser fields: Frontiers of nonlinear optics". In: *Reviews of Modern Physics* 72.2 (2000), p. 545.

[32] Anton Desyatnikov, Andrey Maimistov, and Boris Malomed. "Three-dimensional spinning solitons in dispersive media with the cubic-quintic nonlinearity". In: *Physical Review E* 61.3 (2000), p. 3107.

[33] Nguyen Viet Hung et al. "Spatial control of the competition between self-focusing and self-defocusing nonlinearities in one-and two-dimensional systems". In: *Physical review A* 90.2 (2014), p. 023841.

[34] RW Hellwarth. "Third-order optical susceptibilities of liquids and solids". In: *Progress in Quantum Electronics* 5 (1977), pp. 1–68.

[35] Radha Balakrishnan. "Soliton propagation in nonuniform media". In: *Physical Review A* 32.2 (1985), p. 1144.

[36] Nail Akhmediev, Wiesław Królikowski, and AW Snyder. "Partially coherent solitons of variable shape". In: *Physical review letters* 81.21 (1998), p. 4632.

[37] Leonard Mandel and Emil Wolf. *Optical coherence and quantum optics*. Cambridge university press, 1995.

[38] Konstantinos G Makris et al. "Nonlocal incoherent spatial solitons in liquid crystals". In: *JOSA B* 22.7 (2005), pp. 1371–1377.

[39] S. Coen et al. "Supercontinuum generation by stimulated Raman scattering and parametric four-wave mixing in photonic crystal fibers". In: *Journal of the Optical Society of America B-Optical Physics* 19.4 (2002), pp. 753–764.

[40] NM Kroll and PL Kelley. "Temporal and spatial gain in stimulated light scattering". In: *Physical Review A* 4.2 (1971), p. 763.

[41] O. Bang et al. "Collapse arrest and soliton stabilization in nonlocal nonlinear media". In: *Physical Review E* 66.4 (2002).

[42] B Malomed. "Nonlinear schrödinger equations". In: (2005).

[43] Alwyn Scott. *Encyclopedia of nonlinear science*. Routledge, 2006.

[44] Allan Griffin, David W Snoke, and Sandro Stringari. *Bose-einstein condensation*. Cambridge University Press, 1996.

[45] David JE Callaway. "On the remarkable structure of the superconducting intermediate state". In: *Nuclear Physics B* 344.3 (1990), pp. 627–645.

[46] A Gurevich. *Nonlinear phenomena in the ionosphere*. Vol. 10. Springer Science and Business Media, 2012.

[47] Govind P Agrawal. *Nonlinear Fiber Optics: Formerly Quantum Electronics*. Academic press, 2013.

[48] Vladimir E Zakharov. "Stability of periodic waves of finite amplitude on the surface of a deep fluid". In: *Journal of Applied Mechanics and Technical Physics* 9.2 (1968), pp. 190–194.

[49] Charles Kittel. *Introduction to solid state physics*. 1976.

[50] Mike H Anderson et al. "Observation of Bose-Einstein condensation in a dilute atomic vapor". In: *science* 269.5221 (1995), pp. 198–201.

[51] Xuejun Zhu et al. "Exciton condensate in semiconductor quantum well structures". In: *Physical review letters* 74.9 (1995), p. 1633.

[52] Tim Byrnes, Na Young Kim, and Yoshihisa Yamamoto. "Exciton–polariton condensates". In: *Nature Physics* 10.11 (2014), pp. 803–813.

[53] VE Demidov et al. "Observation of spontaneous coherence in Bose-Einstein condensate of magnons". In: *Physical review letters* 100.4 (2008), p. 047205.

[54] Christopher J Pethick and Henrik Smith. *Bose–Einstein condensation in dilute gases*. Cambridge university press, 2008.

[55] Ming-feng Shih et al. "Two-dimensional steady-state photorefractive screening solitons". In: *Optics letters* 21.5 (1996), pp. 324–326.

[56] Yuri S Kivshar and Govind P Agrawal. *Optical solitons: from fibers to photonic crystals*. Academic press, 2003.

[57] J Stenger et al. "Spin domains in ground-state Bose–Einstein condensates". In: *Nature* 396.6709 (1998), pp. 345–348.

[58] C Menyuk. "Nonlinear pulse propagation in birefringent optical fibers". In: *IEEE Journal of Quantum electronics* 23.2 (1987), pp. 174–176.

[59] U. A. Laudyn et al. "Three-color vector nematicon". In: *Photonics Letters of Poland* 9.2 (2017), pp. 36–38.

[60] Chao Yu, Shicheng Jiang, and Ruifeng Lu. "High order harmonic generation in solids: a review on recent numerical methods". In: *Advances in Physics: X* 4.1 (2019), p. 1562982.

[61] PB Corkum, Claude Rolland, and T Srinivasan-Rao. "Supercontinuum generation in gases". In: *Physical review letters* 57.18 (1986), p. 2268.

[62] AM Kamchatnov, SA Darmanyan, and F Lederer. "Formation of solitons on the sharp front of the pulse in an optical fiber". In: *Physics Letters A* 245.3-4 (1998), pp. 259–264.

[63] R Stolen and J Bjorkholm. "Parametric amplification and frequency conversion in optical fibers". In: *IEEE Journal of Quantum Electronics* 18.7 (1982), pp. 1062–1072.

[64] Robert R Alfano et al. *The supercontinuum laser source*. Springer, 1989.

[65] F Maucher et al. "Self-organization of light in optical media with competing nonlinearities". In: *Physical review letters* 116.16 (2016), p. 163902.

[66] Ole Bang et al. "Engineering competing nonlinearities". In: *Optics letters* 24.20 (1999), pp. 1413–1415.

[67] A. Sigler and B. A. Malomed. "Solitary pulses in linearly coupled cubic-quintic Ginzburg-Landau equations". In: *Physica D-Nonlinear Phenomena* 212.3-4 (2005), pp. 305–316.

[68] Dumitru Mihalache et al. "Stable vortex tori in the three-dimensional cubic-quintic Ginzburg-Landau equation". In: *Physical review letters* 97.7 (2006), p. 073904.

[69] Qi Guo et al. "Large phase shift of nonlocal optical spatial solitons". In: *Physical Review E* 69.1 (2004), p. 016602.

[70] Nail Akhmediev and Adrian Ankiewicz. *Dissipative solitons: from optics to biology and medicine*. Vol. 751. Springer Science & Business Media, 2008.

[71] TK Gustafson et al. "SELF-TRAPPING IN MEDIA WITH SATURATION OF THE NONLINEAR INDEX". In: *Applied Physics Letters* 12.5 (1968), pp. 165–168.

[72] Stefano Trillo and William Torruellas. *Spatial solitons*. Vol. 82. Springer, 2013.

[73] David J Acheson. *Elementary fluid dynamics*. 1991.

[74] D. S. Ricketts et al. "On the self-generation of electrical soliton pulses". In: *Ieee Journal of Solid-State Circuits* 42.8 (2007), pp. 1657–1668.

[75] A. Hasegawa and F. Tappert. "Transmission of Stationary Nonlinear Optical Pulses in Dispersive Dielectric Fibers .1. Anomalous Dispersion". In: *Applied Physics Letters* 23.3 (1973), pp. 142–144.

[76] A. Hasegawa and F. Tappert. "Transmission of Stationary Nonlinear Optical Pulses in Dispersive Dielectric Fibers .2. Normal Dispersion". In: *Applied Physics Letters* 23.4 (1973), pp. 171–172.

[77] Michael C Birse. "Soliton models for nuclear physics". In: *Progress in particle and nuclear physics* 25 (1990), pp. 1–80.

[78] Alan J Heeger et al. "Solitons in conducting polymers". In: *Reviews of Modern Physics* 60.3 (1988), p. 781.

[79] Aleksandr Sergeevich Davydov et al. *Solitons in molecular systems*. Springer, 1985.

[80] Søren SL Andersen, Andrew D Jackson, and Thomas Heimburg. "Towards a thermodynamic theory of nerve pulse propagation". In: *Progress in neurobiology* 88.2 (2009), pp. 104–113.

[81] David W Aossey et al. "Properties of soliton-soliton collisions". In: *Physical Review A* 45.4 (1992), p. 2606.

[82] Yoshitaka Sakai, Raymond J Hawkins, and Stephen R Friberg. "Soliton-collision interferometer for the quantum nondemolition measurement of photon number: numerical results". In: *Optics letters* 15.4 (1990), pp. 239–241.

[83] NF Pilipetskii and AR Rustamov. "Observation of self-focusing of light in liquids". In: *JETP Lett* 2.2 (1965), pp. 55–57.

[84] Kristian Dysthe, Harald E Krogstad, and Peter Müller. "Oceanic rogue waves". In: *Annu. Rev. Fluid Mech.* 40 (2008), pp. 287–310.

[85] John M Dudley and James Roy Taylor. *Supercontinuum generation in optical fibers*. Cambridge University Press, 2010.

[86] Paul Blanchard, RL Devaney, and GR Hall. *Differential Equations*. 1998.

[87] Akira Onuki. *Phase transition dynamics*. Cambridge University Press, 2002.

[88] TS Monteiro and DS Saraga. "Quantum wells in tilted fields: Semiclassical amplitudes and phase coherence times". In: *Foundations of Physics* 31.2 (2001), pp. 355–370.

[89] Neil Boechler, Georgios Theocharis, and C Daraio. "Bifurcation-based acoustic switching and rectification". In: *Nature materials* 10.9 (2011), pp. 665–668.

[90] Sebastian Wieczorek et al. "The dynamical complexity of optically injected semiconductor lasers". In: *Physics Reports* 416.1-2 (2005), pp. 1–128.

[91] Timothy A Denton et al. "Fascinating rhythm: a primer on chaos theory and its application to cardiology". In: *American heart journal* 120.6 (1990), pp. 1419–1440.

[92] Jeffrey P Thomas, Earl H Dowell, and Kenneth C Hall. "Nonlinear inviscid aerodynamic effects on transonic divergence, flutter, and limit-cycle oscillations". In: *AIAA journal* 40.4 (2002), pp. 638–646.

[93] Jean-Marc Ginoux and Christophe Letellier. "Van der Pol and the history of relaxation oscillations: Toward the emergence of a concept". In: *Chaos: An Interdisciplinary Journal of Nonlinear Science* 22.2 (2012), p. 023120.

[94] Aniket Patra, Boris L Altshuler, and Emil A Yuzbashyan. "Chaotic synchronization between atomic clocks". In: *Physical Review A* 100.2 (2019), p. 023418.

[95] Richard J Field and FW Schneider. "Oscillating chemical reactions and nonlinear dynamics". In: *Journal of Chemical Education* 66.3 (1989), p. 195.

[96] Michael C Mackey and Leon Glass. "Oscillation and chaos in physiological control systems". In: *Science* 197.4300 (1977), pp. 287–289.

[97] Alan L Hodgkin and Andrew F Huxley. "A quantitative description of membrane current and its application to conduction and excitation in nerve". In: *The Journal of physiology* 117.4 (1952), pp. 500–544.

[98] EE Sel'Kov. "Self-Oscillations in Glycolysis 1. A Simple Kinetic Model". In: *European Journal of Biochemistry* 4.1 (1968), pp. 79–86.

[99] Edward N Lorenz. "Deterministic nonperiodic flow". In: *Journal of atmospheric sciences* 20.2 (1963), pp. 130–141.

[100] Kathleen T Alligood, Tim D Sauer, and James A Yorke. *Chaos.* Springer, 1996.

[101] AA Tsonis and JB Elsner. "Chaos, strange attractors, and weather". In: *Bulletin of the American Meteorological Society* 70.1 (1989), pp. 14–23.

[102] MA Hernández-Acosta et al. "Chaotic signatures of photoconductive Cu2ZnSnS4 nanostructures explored by Lorenz attractors". In: *New Journal of Physics* 20.2 (2018), p. 023048.

[103] George Contopoulos. *Order and chaos in dynamical astronomy.* Springer Science and Business Media, 2004.

[104] Leonid A Safonov et al. "Multifractal chaotic attractors in a system of delay-differential equations modeling road traffic". In: *Chaos: An Interdisciplinary Journal of Nonlinear Science* 12.4 (2002), pp. 1006–1014.

[105] O. Postavaru, S. R. Anton, and A. Toma. "COVID-19 pandemic and chaos theory". In: *Mathematics and Computers in Simulation* 181 (2021), pp. 138–149.

[106] Erjada Progonati. "Brexit in the Light of Chaos Theory and Some Assumptions About the Future of the European Union". In: *International Symposium on Chaos, Complexity and Leadership.* Springer. 2018, pp. 87–96.

[107] Stephen R Friberg and Kenneth W DeLong. "Breakup of bound higher-order solitons". In: *Optics letters* 17.14 (1992), pp. 979–981.

[108] Hitoshi Kawaguchi et al. "Bistable output characteristics in semiconductor laser injection locking". In: *IEEE Journal of Quantum Electronics* 21.9 (1985), pp. 1314–1317.

[109] A Kaplan. "Multistable self-trapping of light and multistable soliton pulse propagation". In: *IEEE journal of quantum electronics* 21.9 (1985), pp. 1538–1543.

[110] Hermann A Haus. *Waves and fields in optoelectronics*. Prentice-Hall, 1984. ISBN: 0139460535.

[111] DN Christodoulides and RI Joseph. "Slow Bragg solitons in nonlinear periodic structures". In: *Physical review letters* 62.15 (1989), p. 1746.

[112] D Majus et al. "Nature of spatiotemporal light bullets in bulk Kerr media". In: *Physical review letters* 112.19 (2014), p. 193901.

[113] AW Snyder, L Poladian, and DJ Mitchell. "Stable black self-guided beams of circular symmetry in a bulk Kerr medium". In: *Optics Letters* 17.11 (1992), pp. 789–791.

[114] Anton S Desyatnikov, Lluis Torner, and Yuri S Kivshar. "Optical vortices and vortex solitons". In: *arXiv preprint nlin/0501026* (2005).

[115] Aleksandr Ramaniuk et al. "Absorption-mediated stabilization of nonlinear propagation of vortex beams in nematic liquid crystals". In: *Optics Communications* 451 (2019), pp. 338–344.

[116] Halina Rubinsztein-Dunlop et al. "Roadmap on structured light". In: *Journal of Optics* 19.1 (2016), p. 013001.

[117] Andrew Forbes, Michael de Oliveira, and Mark R Dennis. "Structured light". In: *Nature Photonics* 15.4 (2021), pp. 253–262.

[118] Alexander V Buryak, Yuri S Kivshar, and Stefano Trillo. "Stability of three-wave parametric solitons in diffractive quadratic media". In: *Physical review letters* 77.26 (1996), p. 5210.

[119] Falk Lederer et al. "Discrete solitons in optics". In: *Physics Reports* 463.1-3 (2008), pp. 1–126.

[120] Philippe Grelu and Nail Akhmediev. "Dissipative solitons for mode-locked lasers". In: *Nature photonics* 6.2 (2012), pp. 84–92.

[121] Manabu Kagami, Tatsuya Yamashita, and Hiroshi Ito. "Light-induced self-written three-dimensional optical waveguide". In: *Applied Physics Letters* 79.8 (2001), pp. 1079–1081.

[122] Claudio Conti, Marco Peccianti, and Gaetano Assanto. "Route to nonlocality and observation of accessible solitons". In: *Physical review letters* 91.7 (2003), p. 073901.

[123] Andrea Fratalocchi et al. "Nonlinearly controlled angular momentum of soliton clusters". In: *Optics letters* 32.11 (2007), pp. 1447–1449.

[124] Hermann A Haus and William S Wong. "Solitons in optical communications". In: *Reviews of modern physics* 68.2 (1996), p. 423.

[125] Ramgopal Gangwar, Sunil Singh, and Nar Singh. "Soliton based optical communication". In: *Progress In Electromagnetics Research* 74 (2007), pp. 157–166.

[126] E. W. Lentz. "Breaking the warp barrier: hyper-fast solitons in Einstein-Maxwell-plasma theory". In: *Classical and Quantum Gravity* 38.7 (2021).

[127] Mordechai Segev et al. "Vector photorefractive spatial solitons". In: *Optics letters* 20.17 (1995), pp. 1764–1766.

[128] Yuri S Kivshar and Barry Luther-Davies. "Dark optical solitons: physics and applications". In: *Physics reports* 298.2-3 (1998), pp. 81–197.

[129] DY Tang et al. "Observation of high-order polarization-locked vector solitons in a fiber laser". In: *Physical review letters* 101.15 (2008), p. 153904.

[130] S De Nicola. "Conservation laws for the non-linear Schrödinger equation". In: *Pure and Applied Optics: Journal of the European Optical Society Part A* 2.1 (1993), p. 5.

[131] Aleksei Shabat and Vladimir Zakharov. "Exact theory of two-dimensional self-focusing and one-dimensional self-modulation of waves in nonlinear media". In: *Soviet physics JETP* 34.1 (1972), p. 62.

[132] Akira Hasegawa and Yuji Kodama. *Solitons in optical communications*. 7. Oxford University Press on Demand, 1995.

[133] Dmitry E Pelinovsky and Yuri S Kivshar. "Stability criterion for multicomponent solitary waves". In: *Physical Review E* 62.6 (2000), p. 8668.

[134] Nazib G Vakhitov and Aleksandr A Kolokolov. "Stationary solutions of the wave equation in the medium with nonlinearity saturation". In: *Radiophysics and Quantum Electronics* 16.7 (1973), pp. 783–789.

[135] Jalal Shatah and Walter Strauss. "Instability of nonlinear bound states". In: *Communications in Mathematical Physics* 100.2 (1985), pp. 173–190.

[136] Marc Haelterman, AP Sheppard, and AW Snyder. "Bound-vector solitary waves in isotropic nonlinear dispersive media". In: *Optics letters* 18.17 (1993), pp. 1406–1408.

[137] HT Tran and RA Sammut. "Instability of two-frequency dark waves in self-defocusing media". In: *Optics communications* 119.5-6 (1995), pp. 583–586.

[138] VV Afanasyev et al. "Dynamics of coupled dark and bright optical solitons". In: *Optics letters* 14.15 (1989), pp. 805–807.

[139] Elena A Ostrovskaya et al. "Stability of multihump optical solitons". In: *Physical review letters* 83.2 (1999), p. 296.

[140] Raul de La Fuente and Alain C Barthelemy. "Spatial soliton-induced guiding by cross-phase modulation". In: *IEEE journal of quantum electronics* 28.2 (1992), pp. 547–554.

[141] Adrian P Sheppard and Yuri S Kivshar. "Polarized dark solitons in isotropic Kerr media". In: *Physical Review E* 55.4 (1997), p. 4773.

[142] Elena A Ostrovskaya et al. "Multichannel soliton transmission and pulse shepherding in bit-parallel-wavelength optical fiber links". In: *IEEE Journal of selected topics in quantum electronics* 8.3 (2002), pp. 591–596.

[143] Jianke Yang. *Nonlinear Waves in Integrable and Non-integrable Systems*. Society for Industrial and Applied Mathematics, 2010.

[144] William H Press et al. *Numerical recipes 3rd edition: The art of scientific computing*. Cambridge university press, 2007.

[145] Hans Petter Langtangen and Svein Linge. *Finite difference computing with PDEs: a modern software approach*. Springer Nature, 2017.

[146] Jiaqun Wang, Youhe Zhou, and Xiaojing Liu. "A Space-Time Fully Decoupled Wavelet Galerkin Method for Solving Multidimensional Nonlinear Schrödinger Equations with Damping". In: *Mathematical Problems in Engineering* 2017 (2017).

[147] William E Schiesser and Graham W Griffiths. *A compendium of partial differential equation models: method of lines analysis with Matlab*. Cambridge University Press, 2009.

[148] Sahil Garg and Mohit Pant. "Meshfree methods: A comprehensive review of applications". In: *International Journal of Computational Methods* 15.04 (2018), p. 1830001.

[149] Y. Y. Choy et al. "Crank-Nicolson Implicit Method For The Nonlinear Schrodinger Equation With Variable Coefficient". In: *Proceedings of the 21st National Symposium on Mathematical Sciences (Sksm21): Germination of Mathematical Sciences Education and Research Towards Global Sustainability* 1605 (2014), pp. 76–82.

[150] A Hadjidimos. "Successive overrelaxation (SOR) and related methods". In: *Journal of Computational and Applied Mathematics* 123.1-2 (2000), pp. 177–199.

[151] Endre Süli and David F Mayers. *An introduction to numerical analysis*. Cambridge university press, 2003.

[152] TE Simos. "Modified Runge-Kutta-Fehlberg methods for periodic initial-value problems". In: *Japan journal of industrial and applied mathematics* 12.1 (1995), pp. 109–122.

[153] Charles Eric Leiserson et al. *Introduction to algorithms*. Vol. 3. MIT press, 1994.

[154] P. S. Jung, K. Rutkowska, and M. A. Karpierz. "Evanescent field boundary conditions for modelling of light propagation". In: *Journal of Computational Science* 25 (2018), pp. 115–121.

[155] Brian Hall. *Lie groups, Lie algebras, and representations: an elementary introduction*. Vol. 222. Springer, 2015.

[156] Thiab R Taha and Mark I Ablowitz. "Analytical and numerical aspects of certain nonlinear evolution equations. II. Numerical, nonlinear Schrödinger equation". In: *Journal of Computational Physics* 55.2 (1984), pp. 203–230.

[157] Stéphane Balac and Arnaud Fernandez. "Mathematical analysis of adaptive step-size techniques when solving the nonlinear Schrödinger equation for simulating light-wave propagation in optical fibers". In: *Optics Communications* 329 (2014), pp. 1–9.

[158] Junuthula Narasimha Reddy. *Introduction to the finite element method*. McGraw-Hill Education, 2019.

[159] Vladimir I Petviashvili. "Equation of an extraordinary soliton". In: *Fizika plazmy* 2 (1976), pp. 469–472.

[160] J. K. Yang and T. I. Lakoba. "Universally-convergent squared-operator iteration methods for solitary waves in general nonlinear wave equations". In: *Studies in Applied Mathematics* 118.2 (2007), pp. 153–197.

[161] J. K. Yang and T. I. Lakoba. "Accelerated imaginary-time evolution methods for the computation of solitary waves". In: *Studies in Applied Mathematics* 120.3 (2008), pp. 265–292.

[162] J. Yang. "Newton-conjugate-gradient methods for solitary wave computations". In: *Journal of Computational Physics* 228.18 (2009), pp. 7007–7024.

[163] Jonathan Richard Shewchuk. *An introduction to the conjugate gradient method without the agonizing pain*. Generic. 1994.

[164] Yousef Saad. *Iterative methods for sparse linear systems*. SIAM, 2003.

[165] K. B. Zegadlo et al. "Symmetry Breakings in Dual-Core Systems with Double-Spot Localization of Nonlinearity". In: *Symmetry-Basel* 10.5 (2018).

[166] Henryk Arodz, Jacek Dziarmaga, and Wojciech Hubert Zurek. *Patterns of symmetry breaking*. Vol. 127. Springer Science & Business Media, 2003.

[167] Steven H Strogatz. *Nonlinear dynamics and chaos with student solutions manual: With applications to physics, biology, chemistry, and engineering*. CRC press, 2018.

[168] Grégory Barbillon, Andrey Ivanov, and Andrey K Sarychev. "Applications of Symmetry Breaking in Plasmonics". In: *Symmetry* 12.6 (2020), p. 896.

[169] Jeff Hecht. *City of light: the story of fiber optics*. Oxford University Press on Demand, 2004.

[170] C Pollock and Michal Lipson. *Integrated photonics*. Vol. 20. Springer, 2003. ISBN: 1441953981.

[171] Tomohiro Amemiya et al. "Metamaterial waveguide devices for integrated optics". In: *Materials* 10.9 (2017), p. 1037.

[172] Katsunari Okamoto. *Fundamentals of optical waveguides*. Academic press, 2006. ISBN: 0125250967.

[173] J Hukriede, D Runde, and D Kip. "Fabrication and application of holographic Bragg gratings in lithium niobate channel waveguides". In: *Journal of Physics D: Applied Physics* 36.3 (2003), R1.

[174] Marcello Ferrera et al. "Low-power continuous-wave nonlinear optics in doped silica glass integrated waveguide structures". In: *Nature photonics* 2.12 (2008), pp. 737–740.

[175] Wei-Ping Huang. "Coupled-mode theory for optical waveguides: an overview". In: *JOSA A* 11.3 (1994), pp. 963–983.

[176] Thawatchai Mayteevarunyoo, Boris A Malomed, and Guangjiong Dong. "Spontaneous symmetry breaking in a nonlinear double-well structure". In: *Physical Review A* 78.5 (2008), p. 053601.

[177] GJ Milburn et al. "Quantum dynamics of an atomic Bose-Einstein condensate in a double-well potential". In: *Physical Review A* 55.6 (1997), p. 4318.

[178] Ying Xue et al. "Plasmonic lattice solitons beyond the coupled-mode theory". In: *Laser & Photonics Reviews* 8.4 (2014), pp. L52–L57.

[179] Augusto Smerzi et al. "Quantum coherent atomic tunneling between two trapped Bose-Einstein condensates". In: *Physical Review Letters* 79.25 (1997), p. 4950.

[180] M Böhm and F Mitschke. "Solitons in lossy fibers". In: *Physical Review A* 76.6 (2007), p. 063822.

[181] Or Peleg et al. "Self-trapped leaky waves and their interactions". In: *Physical Review A* 80.4 (2009), p. 041801.

[182] H-G Purwins, HU Bödeker, and Sh Amiranashvili. "Dissipative solitons". In: *Advances in Physics* 59.5 (2010), pp. 485–701.

[183] Elena A Ostrovskaya et al. "Dissipative solitons and vortices in polariton Bose-Einstein condensates". In: *Physical Review A* 86.1 (2012), p. 013636.

[184] Orazio Svelto and David C Hanna. *Principles of lasers*. Vol. 4. Springer, 1998.

[185] MA Kaliteevski et al. "Whispering gallery polaritons in cylindrical cavities". In: *Physical Review B* 75.23 (2007), p. 233309.

[186] Hyun Gyu Song et al. "Tailoring the potential landscape of room-temperature single-mode whispering gallery polariton condensate". In: *Optica* 6.10 (2019), pp. 1313–1320.

[187] D. A. Zezyulin and V. V. Konotop. "Nonlinear currents in a ring-shaped waveguide with balanced gain and dissipation". In: *Physical Review A* 94.4 (2016).

[188] Alexander Dreismann et al. "Coupled counterrotating polariton condensates in optically defined annular potentials". In: *Proceedings of the National Academy of Sciences* 111.24 (2014), pp. 8770–8775.

[189] C Sturm et al. "Nonequilibrium polariton condensate in a magnetic field". In: *Physical Review B* 91.15 (2015), p. 155130.

[190] Naotomo Takemura et al. "Polaritonic feshbach resonance". In: *Nature Physics* 10.7 (2014), pp. 500–504.

[191] N Takemura et al. "Spin anisotropic interactions of lower polaritons in the vicinity of polaritonic Feshbach resonance". In: *Physical Review B* 95.20 (2017), p. 205303.

[192] M. C. Gwinner et al. "Periodic Large-Area Metallic Split-Ring Resonator Metamaterial Fabrication Based on Shadow Nanosphere Lithography". In: *Small* 5.3 (2009), pp. 400–406.

[193] Jonathan Grandidier et al. "Gain-assisted propagation in a plasmonic waveguide at telecom wavelength". In: *Nano letters* 9.8 (2009), pp. 2935–2939.

[194] Govind P Agrawal. "Induced focusing of optical beams in self-defocusing nonlinear media". In: *Physical review letters* 64.21 (1990), p. 2487.

[195] A. Ramaniuk et al. “Vortex Creation without Stirring in Coupled Ring Resonators with Gain and Loss”. In: *Symmetry-Basel* 10.6 (2018).

[196] N. V. Hung et al. “Modulational instability of coupled ring waveguides with linear gain and nonlinear loss”. In: *Scientific Reports* 7 (2017).

[197] Krzysztof Zegadlo et al. “Route to chaos in a coupled microresonator system with gain and loss”. In: *Nonlinear Dynamics* 97.1 (2019), pp. 559–569.

[198] A. S. Desyatnikov, Y. S. Kivshar, and L. Torner. “Optical vortices and vortex solitons”. In: *Progress in Optics, Vol 47* 47 (2005), pp. 291–391.

[199] R Driben et al. “Dynamics of dipoles and vortices in nonlinearly coupled three-dimensional field oscillators”. In: *Physical Review E* 94.1 (2016), p. 012207.

[200] Floris Takens. “Detecting strange attractors in turbulence”. In: *Dynamical systems and turbulence, Warwick 1980*. Springer, 1981, pp. 366–381.

[201] Ricardo Mañé. “On the dimension of the compact invariant sets of certain nonlinear maps”. In: *Dynamical Systems and Turbulence, Warwick 1980*. Springer, 1981, pp. 230–242.

[202] JU Kang et al. “Observation of Manakov spatial solitons in AlGaAs planar waveguides”. In: *Physical review letters* 76.20 (1996), p. 3699.

[203] S Gatz and Joachim Herrmann. “Soliton propagation in materials with saturable nonlinearity”. In: *JOSA B* 8.11 (1991), pp. 2296–2302.

[204] Pawel S Jung et al. “Semi-analytical approach to supermode spatial solitons formation in nematic liquid crystals”. In: *Optics express* 25.20 (2017), pp. 23893–23898.

[205] A. Ramaniuk et al. “Scalar and vector supermode solitons owing to competing nonlocal nonlinearities”. In: *Optics Express* 29.6 (2021), pp. 8015–8023.

[206] Iam-Choon Khoo. *Liquid crystals*. Vol. 64. John Wiley & Sons, 2007.

[207] Pierre-Gilles De Gennes and Jacques Prost. *The physics of liquid crystals*. 83. Oxford university press, 1993.

[208] Danish Iqbal and Muhammad Haris Samiullah. “Photo-responsive shape-memory and shape-changing liquid-crystal polymer networks”. In: *Materials* 6.1 (2013), pp. 116–142.

[209] Kunihiro Ichimura. “Photoalignment of liquid-crystal systems”. In: *Chemical reviews* 100.5 (2000), pp. 1847–1874.

[210] O Buchnev et al. “Nematicon waveguides: self-confined beams and their electric control”. In: *Applied Physics B* 108.1 (2012), pp. 177–182.

[211] J Stöhr and MG Samant. “Liquid crystal alignment by rubbed polymer surfaces: a microscopic bond orientation model”. In: *Journal of electron spectroscopy and related phenomena* 98 (1999), pp. 189–207.

[212] Iga Ostromęcka et al. “Measurements of the quality of nematic liquid crystal alignment”. In: *Photonics Letters of Poland* 8.1 (2016), pp. 14–16.

[213] Pawel S Jung et al. “Formation and stability of vortex solitons in nematic liquid crystals”. In: *Optics Letters* 46.1 (2021), pp. 62–65.

[214] M Peccianti et al. "Electrically assisted self-confinement and waveguiding in planar nematic liquid crystal cells". In: *Applied Physics Letters* 77.1 (2000), pp. 7–9.

[215] Gaetano Assanto, Marco Peccianti, and Claudio Conti. "Nematicons: optical spatial solitons in nematic liquid crystals". In: *Optics and photonics news* 14.2 (2003), pp. 44–48.

[216] Marco Peccianti and Gaetano Assanto. "Nematicons". In: *Physics Reports* 516.4-5 (2012), pp. 147–208.

[217] Gaetano Assanto. "Nematicons: reorientational solitons from optics to photonics". In: *Liquid Crystals Reviews* 6.2 (2018), pp. 170–194.

[218] Yana V Izdebskaya et al. "Stable vortex soliton in nonlocal media with orientational nonlinearity". In: *Optics letters* 43.1 (2018), pp. 66–69.

[219] Alessandro Alberucci et al. "Two-color vector solitons in nonlocal media". In: *Physical review letters* 97.15 (2006), p. 153903.

[220] Theodoros P Horikis and Dimitrios J Frantzeskakis. "Vector nematicons: Coupled spatial solitons in nematic liquid crystals". In: *Physical Review A* 94.5 (2016), p. 053805.

[221] Urszula Anna Laudyn et al. "Three-color vector nematicon". In: *Photonics Letters of Poland* 9.2 (2017), pp. 36–38.

[222] István Jánossy. "Molecular interpretation of the absorption-induced optical reorientation of nematic liquid crystals". In: *Physical Review E* 49.4 (1994), p. 2957.

[223] Gaetano Assanto et al. "Temperature control of nematicon trajectories". In: *Physical Review E* 100.6 (2019), p. 062702.

[224] JA Fleck and MD Feit. "Beam propagation in uniaxial anisotropic media". In: *JOSA* 73.7 (1983), pp. 920–926.

[225] A Alberucci et al. "Propagation of spatial optical solitons in a dielectric with adjustable nonlinearity". In: *Physical Review A* 82.2 (2010), p. 023806.

[226] Paweł Jung. "Modelowanie propagacji fali elektromagnetycznej w strukturach ciekłokrystalicznych i subfalowych". PhD thesis. Optics and Photonics Division, 2016.

[227] Yozo Utsumi et al. "Measurement methods of nematic liquid crystal response time". In: *Molecular crystals and liquid crystals* 434.1 (2005), pp. 9–337.

[228] Pawel S Jung et al. "Supermode spatial optical solitons in liquid crystals with competing nonlinearities". In: *Physical Review A* 95.2 (2017), p. 023820.

[229] Frederick C Frank. "I. Liquid crystals. On the theory of liquid crystals". In: *Discussions of the Faraday Society* 25 (1958), pp. 19–28.

[230] Filip A Sala and Miroslaw A Karpierz. "Modeling of molecular reorientation and beam propagation in chiral and non-chiral nematic liquid crystals". In: *Optics express* 20.13 (2012), pp. 13923–13938.

[231] Filip A Sala and Mirosław A Karpierz. "Chiral and nonchiral nematic liquid-crystal reorientation induced by inhomogeneous electric fields". In: *JOSA B* 29.6 (2012), pp. 1465–1472.

[232] Shaozhi Pu et al. "Solitons in liquid crystals with competing nonlinearities". In: *Optics Communications* 450 (2019), pp. 78–86.

[233] Qing Wang, Jingzhen Li, and Weixin Xie. "Elliptic optical soliton in anisotropic nonlocal competing cubic–quintic nonlinear media". In: *IEEE Photonics Journal* 10.2 (2018), pp. 1–11.

[234] Pawel Stanislaw Jung et al. "Supermode spatial solitons via competing nonlocal nonlinearities". In: *Photonics Letters of Poland* 10.2 (2018), pp. 33–35.

[235] Alessandro Alberucci et al. "Soliton enhancement of spontaneous symmetry breaking". In: *Optica* 2.9 (2015), pp. 783–789.

[236] Armando Piccardi, Alessandro Alberucci, and Gaetano Assanto. "Power-dependent nematicon steering via walk-off". In: *JOSA B* 27.11 (2010), pp. 2398–2404.

[237] Martin Wimmer et al. "Optical diametric drive acceleration through action–reaction symmetry breaking". In: *Nature Physics* 9.12 (2013), pp. 780–784.

[238] Alessandro Alberucci et al. "Effective breaking of the action-reaction principle using spatial solitons". In: *Physical Review A* 100.1 (2019), p. 011802.

[239] Brian C Hall. *Quantum theory for mathematicians*. Vol. 267. Springer, 2013.